CHEMICAL REVIEWS

Review

pubs.acs.org/CR

Scanning probe microscopy and spectroscopy of colloidal semiconductor nanocrystals and assembled structures

Ingmar Swart,[†] Peter Liljeroth,[‡] and Daniel Vanmaekelbergh*[,†]

[†]Debye Institute for Nanomaterials Science, Chemistry Department, University of Utrecht, Princetonplein 5, 3584 CC Utrecht, The Netherlands

[‡]Department of Applied Physics, Aalto University School of Science, PO Box 15100, 00076 Aalto, Finland

ABSTRACT: Colloidal semiconductor nanocrystals become increasingly important in materials science and technology, due to their optoelectronic properties that are tunable by size. The measurement and understanding of their energy levels is key to scientific and technological progress. Here we review how the confined electronic orbitals and related energy levels of individual semiconductor quantum dots have been measured by means of scanning tunneling microscopy and spectroscopy. These techniques were originally developed for flat conducting surfaces, but they have been adapted to investigate the atomic and electronic structure of semiconductor quantum dots. We compare the results obtained on colloidal quantum dots with those on comparable solid-state ones. We also compare the results obtained with scanning tunneling spectroscopy with those of optical spectroscopy. The first three sections provide an introduction to colloidal quantum dots, and a theoretical basis to be able to understand tunneling spectroscopy on dots attached to a conducting surface. In sections 4 and 5, we review the work performed on lead-chalcogenide nanocrystals and on colloidal quantum dots and rods of II−VI compounds, respectively. In section 6, we deal with colloidal III−V nanocrystals and compare the results with their self-assembled counter parts. In section 7, we review the work on other types of semiconductor quantum dots, especially on Si and Ge nanocrystals.

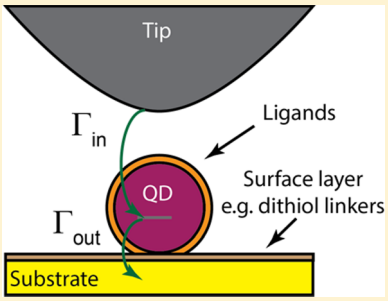

CONTENTS

Special Issue: Nanoparticle Chemistry

Received: November 17, 2015
Published: February 22, 2016

DOI: 10.1021/acs.chemrev.5b00678
Chem. Rev. 2016, 116, 11181−11219

1. INTRODUCTION

Scanning tunneling microscopy was invented in the beginning of the 1980s by a research group at IBM, Zurich. Briefly, the instrument was able to position an ultraclean metallic tip on sub-nanometer distance from a clean and nearly flat surface of a semiconductor or metal. Upon application of a bias between the tip and the substrate, a current flows due to electron tunneling. By scanning the tip over the surface, and monitoring the tunneling current at a given tip height and bias, an "atomic" image of the surface is obtained. This method is called scanning tunneling microscopy (STM). If the position of the tip is kept constant, and the tunneling current is measured as a function of the bias, the local density of electronic states of the conductor can be measured as a function of the energy, at the specific position of the tip. As information is obtained on energy levels, the technique was coined scanning tunneling spectroscopy (STS). Besides the surface of the conductor, it became clear that also small molecules or nanocrystals attached to the atomically flat substrate could be imaged and that their energy levels could be measured also.

It is thus not a surprise that STM/STS became a valuable method to investigate semiconductor nanocrystals (quantum dots) obtained by gas-phase deposition or by wet colloidal chemistry. Initiated in the 1980s, the field of colloidal nanocrystalline quantum dots became one of the fastest developing fields in nanoscience and materials science, and it still is today. Around 2000, it became clear that scanning tunnelling microscopy and spectroscopy (STM and STS) performed on individual nanocrystals allowed one to explore their single-particle energy-level structure, as well as electron−electron and electron−phonon interactions. For a number of reasons outlined below, STM/STS on colloidal quantum dots provides information that is partly complementary to that of optical spectroscopy, which has been used on a much broader scale. In this Review, we present and discuss the STM/STS research on (colloidal) quantum dots, and where it is possible and appropriate, we compare the results with those obtained by optical spectroscopy.

2. COLLOIDAL NANOCRYSTALS OF SEMICONDUCTOR COMPOUNDS: SCIENTIFIC INTEREST AND COMPARISON WITH SOLID-STATE QUANTUM DOTS

At the end of the foregoing century, colloidal nanocrystals formed one of the fastest developing fields in nanoscience, and

DOI: 10.1021/acs.chemrev.5b00678
Chem. Rev. 2016, 116, 11181−11219

this is still the case in 2016. The success of this field is due to a combination of factors: (i) versatile synthesis of colloidal semiconductor nanocrystals and heteronanocrystals of various compounds with optoelectronic quality that approaches that of the precious solid-state quantum dots formed by gas-phase deposition, (ii) the strong effect of quantum confinement that enables one to tailor the optical transitions of a given system of nanocrystals over a very broad energy range, and (iii) the enormous progress in optical and electrical spectroscopic techniques that enables one to fully uncover the exciting physics of these systems. Around 2000, it became clear that scanning tunnelling microscopy and spectroscopy (STM and STS) performed on individual nanocrystals allowed one to explore their single-particle energy-level structure as well as electron−electron and electron−phonon interactions.[1−8] Here, we provide a review of the progress made in this exciting field in the last two decades. This Review focuses on colloidal quantum dots, but we will compare the results with those obtained on their solid-state counterparts where it is appropriate.

2.1. Colloidal nanocrystals that display confined eigenstates

2.1.1. Brief historical perspective. In 1993, a paper was published on the synthesis of Cd-chalcogenides (CdX, X = S, Se, Te) quantum dots that redirected the field of colloidal nanoscience.[9] The work demonstrated the synthesis of suspensions of CdSe (CdS, CdTe) nanocrystals that were stabilized by an organic capping and dispersed in a nonpolar organic solvent, such as hexane and toluene. The distribution of nanocrystal size in a given suspension was relatively small compared to previous synthesis methods (<10%). Upon optical excitation, these suspensions showed (nearly) monochromatic emission reflecting the radiative recombination of the lowest-energy exciton.[10] The photoluminescence quantum yield was ∼10%, a high value at that time. The emission color could be tuned by the size of the nanocrystals, ranging between blue (nanocrystal diameter of ∼2 nm) to the near-IR (nanocrystal size of ∼7 nm) as a result of the electron− and hole−particle confinement in the nanocrystal. Hence, a novel class of semiconductor nanocrystals emerged in which the optical transitions were directly related to the quantum-confined eigenstates.[11−20]

2.1.2. Hot injection method. The synthesis method was based on the injection of Cd and Se precursors in a hot solvent that consisted merely of the capping ligands, resulting in (nearly) instant crystal nucleation, and further growth of the critical nuclei. Nucleation and growth were performed at relatively high temperatures; the slow growth at elevated temperature and the presence of an excess of capping ligands in the reaction medium favored the formation of defect-free semiconductor nanocrystals that were also reasonably passivated by the capping ligands. This resulted in nanocrystal suspensions that showed (nearly) monochromatic emission from the lowest exciton state with a photoluminescence quantum yield of 10%. An astonishing amount of work has been performed on understanding the mechanisms of the nucleation and growth, up to this date.[21−33] Reviews of the synthesis of colloidal nanocrystals can be found in the literature and in this special issue. It soon became apparent that the synthesis method based on organo-metallic precursors injected in an organic medium at elevated temperatures was broadly applicable; it is now used to prepare nanocrystal suspensions of many semiconductor, metallic, and magnetic compounds.[34−36] It also served as a basis to develop the growth of anisotropic systems such as 1-D semiconductor nanowires and 2-D nanoplatelets.[37−56]

2.1.3. Characterization of the atomic structure of nanocrystals. The atomic structure of the prepared nanocrystals with their crystallographic facets has been studied with X-ray diffraction (XRD), transmission electron microscopy (TEM), and high-angle annular dark-field microscopy (HAADF-STEM).[49,57−69] As an example, Figure 1 displays

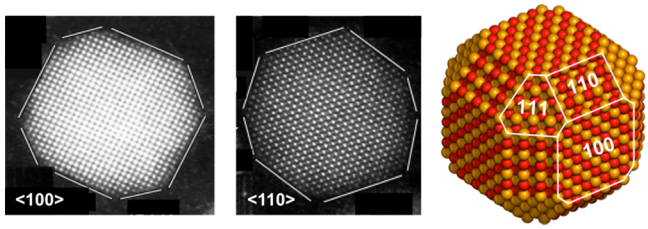

Figure 1. Atomic structure of colloidal PbSe nanocrystals of ∼5 nm in size derived from scanning transmission electron microscopy (STEM). (Left and center) HAADF-STEM images of two PbSe nanocrystals; in the left image the nanocrystal is oriented such that the electron beam is directed perfectly along the <100> direction, and atomic columns are seen, each consisting of equal numbers of Pb and Se. In the image in the center, the beam is directed in the <110> direction; atomic columns of pure Pb (bright) and pure Se (dark gray) are seen. In the right image is a model for a rock salt PbSe nanocrystal derived on the basis of the STEM data. The model is based on a cubic shape, from which edges and corners are truncated. Reprinted with permission from ref 58. Copyright 2013 American Chemical Society.

HAADF-STEM images of PbSe nanocrystals in two viewing directions. It is found that the nanocrystals have the same rock salt crystal structure as bulk PbSe, and even the distance between the atomic planes is identical to those in the bulk phase. From such data, a model for the atomic structure of PbSe nanocrystals and the facets can be constructed. While the inorganic core structure of the nanocrystals has been thoroughly studied, the attachment of the capping molecules to the facets is only now being unraveled by advanced NMR techniques and IR spectroscopy.[70−78]

2.2. Core/shell nanocrystals and heterostructures

2.2.1. Colloidal semiconductor nanocrystals with increased photoluminescence quantum yield. The first colloidal CdSe semiconductor nanocrystals capped with 1−2 monolayers of ZnS were reported in 1996.[79] The work was rapidly followed up.[80−85] Such core−shell systems show analogy with their solid-state semiconductor counterparts, in which each quantum dot (QD) is embedded in a second semiconductor with higher band gap. The shell grows epitaxially on the different facets of the nanocrystal. This can result in the passivation of the core interfacial states in a more robust way than simply by organic ligands. As a result, the photoluminescence (PL) quantum yield of these so-called core−shell nanocrystals is large, currently up to a level of 50−90%; also the photochemical stability under ambient conditions is improved.

2.2.2. Core−shell systems in a broader perspective. The importance of core−shell systems for the field of colloidal nanoscience cannot be overestimated: the shell enables colloidal nanocrystals that are photochemically sufficiently robust for advanced spectroscopy and applications. Second, core−shell systems heralded the start of the development of colloidal nanocrystal heterostructures in which the electronic

DOI: 10.1021/acs.chemrev.5b00678
Chem. Rev. 2016, 116, 11181−11219

and optical properties can be engineered not only by means of quantum confinement but also by the presence of two semiconductor crystalline phases connected epitaxially in one colloidal nanoparticle. The most important developments were heteronanocrystals with separated electron and hole wave functions (type-II) systems, architectures with soft potential wells that reduce nonradiative Auger recombination, and systems in which a metal or magnetic phase is in quantum contact with a semiconductor compound in each colloidal nanoparticle (refs 40, 54, 57, and 86−130).

2.3. Nanocrystal superlattices and 1-D and 2-D systems assembled from nanocrystals

2.3.1. Colloid crystallization on adding a nonsolvent or by solvent evaporation. Suspensions of semiconductor nanocrystals capped with organic molecules in an organic solvent are stable against coagulation by the fact that the interactions between the ligands of two nanocrystals are very similar in nature and strength to those between the ligands and the solvent molecules. Hence, the solvent screens the van der Waals attraction between the capping of adjacent nanocrystals, and only the core−core attraction (on a distance determined by the capping mantle) is left as attractive pair potential. To induce colloidal crystallization, the suspension has to be destabilized, either by adding a nonsolvent to increase the attraction between the particles or by solvent evaporation to increase the particle volume fraction.[131−136] Colloidal crystallization by solvent evaporation has been studied extensively. Using suspensions with two types of nanocrystals, it has been shown that the hard-sphere model forms a good basis to understand colloidal crystallization of semiconductor nanocrystals: i.e., crystallization is not driven by a decrease in the enthalpy of the system but by an increase in the entropy.[137−139] This seemingly counterintuitive model has been previously verified for larger charged colloids in polar solvents.[140−142] When the nanocrystals have a metallic core, the core−core attractions are stronger and can no longer be neglected as a contribution to the overall driving force in crystallization.[137]

2.3.2. Nanocrystal assembly and epitaxial attachment. With nanocrystals of the Pb-chalcogenide compounds, it was observed that the organic capping on certain facets is not present or only weakly attached. Under certain conditions, such nanocrystals undergo oriented attachment, i.e., larger crystals are formed by epitaxial attachment of individual nanocrystals via certain facets.[62,143,144] For PbS and PbSe compounds, single-crystalline 1-D rods and 2-D quantum wells have been obtained.[145−147] Recently, also 2-D systems with a superimposed square and honeycomb nanogeometry have been reported.[148−150] The nanocrystals assemble at the suspension−air interface in a crystallographically oriented way and eventually form single crystals by facet-to-facet necking.

2.3.3. Nanocrystal superlattices as an emerging class of new materials. One of the driving forces in the study of the formation of nanocrystal crystallization is the possibility of nanocrystal superlattices, i.e., arrays in which one or more types of nanocrystals are ordered in a geometrical fashion and are in close contact. Thus, novel properties may emerge by electronic coupling and/or far-field "dipole" interactions between the nanocrystals in the ground or photoexcited state. In recent years, the electronic transport properties of nanocrystal superlattices have been studied extensively.[36,151−159] It has been demonstrated that the carrier mobility in superlattices of nanocrystals in which the organic capping is retained is very low. However, by in situ exchange of the organic capping molecules for shorter organic or inorganic moieties, the carrier mobility can be improved by many orders of magnitude. Recently mobilities up to 200 $cm^2/(V\,s)$ have been reported for CdSe nanocrystal systems.[156,160,161]

2.3.4. Properties of single-crystalline 1-D and 2-D semiconductors. It should be clear that, in 1-D and 2-D atomically coherent systems formed by oriented attachment, there is no material tunneling barrier between two attached nanocrystals. Still, if the crystalline necks are thinner than the nanocrystals themselves, effective tunneling barriers exist due to quantum confinement. Considerable quantum mechanical coupling is expected in these systems. This is corroborated by the large mobilities reported for PbSe rods and for atomically coherent 2-D systems of PbSe with a square geometry. Atomically coherent systems with a honeycomb nanogeometry obtain a special band structure due to the honeycomb geometry. Effective mass, k.p, and atomistic calculations show that honeycomb semiconductors combine the band gap of a 2-D quantum well with genuine Dirac valence and conduction bands,[162−165] i.e., a linear (instead of a quadratic) relationship between the kinetic electron energy and the momentum around the K-points in the Brillouin zone. In heavy-element honeycomb semiconductors, it is predicted that the Dirac bands should show a nontrivial opening at the K-points, giving rise to the quantum spin Hall effect.[164,166−168]

2.4. Optical spectroscopy on colloidal and solid-state quantum dots

Since the 1980s, solid-state semiconductor quantum dots have been prepared by gas-phase deposition techniques, i.e., chemical vapor deposition (CVD) and molecular beam epitaxy (MBE), in analogy with the fabrication of quantum well layers. Most of the work on these so-called self-assembled quantum dots was devoted to group III−V, II−VI, and IV−VI compounds.[169−194] The nanocrystals are epitaxially grown on a crystalline substrate and, in a second step, overgrown. The substrate and the shell layers consist of a semiconductor compound with larger band gap. The inorganic shells result in the electronic passivation of surface states and often to interfacial alloying. InAs QDs in a GaAs matrix or GaAs quantum dots in a (Ga,Al)As matrix are well-studied examples. The inorganic shells can also influence the QD shape (usually a strongly flattened pyramid), the atomic strain, and the alloyed composition of the quantum dot. Self-assembled quantum dots have been studied extensively with advanced optical spectroscopy on the ensemble and single-dot level. Because of the way in which the QDs are incorporated in a solid matrix, quantum coupling between adjacent dots can often not be neglected. The current research is focused, on one hand, on fundamental topics, e.g., in advanced quantum optics. On the other hand, self-assembled solid-state quantum dots are applied in solid-state (IR) laser systems, light-emitting diodes (LEDs), photon detectors, and solar cells.

Modern colloidal nanocrystal synthesis has focused (besides on several families of oxide compounds) on the Cd-, Pb-, and Hg-chalcogenide compounds and InP and InAs nanocrystals,[195] emitting in the near-IR. Recently, the synthetic efforts have been extended to nanocrystals of the CuIn(S,Se) family,[196−203] new III−V compounds such as InSb,[204] and perovskites,[205,206] e.g., $CsPbX_3$ (X = Cl, Br, I). As a consequence of the wet-chemical synthesis, the colloidal quantum dots are naturally present in suspension; this means that individual QDs are on

DOI: 10.1021/acs.chemrev.5b00678
Chem. Rev. 2016, 116, 11181−11219

average well-separated and there is no quantum mechanical interaction between them. Hence, optical absorption and emission spectroscopy performed on suspensions can be used to study the optoelectronic properties of *noninteracting* colloidal nanocrystals. In this way, the quantum properties of individual quantum dots should be fully displayed. There is only one drawback in these ensemble measurements, namely, inhomogeneous spectral line-broadening due to the fact that the nanocrystals all contain a slightly different number of atoms and thus show a slightly varying degree of electron and hole confinement. By dilute deposition of the nanocrystals on a glass or quartz substrate, the optical properties of individual nanocrystals can be studied by spectroscopy on the single-particle level.[182,184,207−221] Single-photon emission by an individual colloidal QD is demonstrated by "anti-bunching" in time-correlated photon detection. The examination of individual colloidal quantum dots has led to outstanding work on the intermittency in the nanocrystal emission (blinking), single and two-photon emission from exciton and biexciton states, the competition between the nonradiative Auger recombination and the exciton luminescence, and the cooling of hot excitons.[82,125,222−235] All these issues are directly connected to the atomic structure of the nanocrystals, e.g., the capping ligands, core−shell structure, and interfacial alloying. The atomic structure can be better controlled by the enormous progress that has recently been made in colloid synthesis (see refs in section 2.2). It turns out that the core−shell engineering of colloidal nanocrystals allows one to perform advanced optical spectroscopy akin to that performed on self-assembled solid-state QDs. Colloidal QDs have the advantage that they can be dispersed as individual quantum objects with minor interaction with the substrate. Moreover, they can be processed to occupy specific positions on a substrate or brought into contact with another nanoscale device structure. Colloidal QDs generally have a smaller volume and thus stronger quantum confinement than their solid-state counterparts, resulting in a larger separation of the exciton states, and a more pronounced fine structure due to exchange interactions, nanocrystal shape, and crystal-field splitting.

2.5. Scanning tunneling microscopy and spectroscopy on self-assembled and colloidal QDs

2.5.1. Self-assembled QDs offering stable and clean tunneling junctions (refs 169, 181, 185, 187, 190−192, and 236−261). Self-assembled quantum dots are grown epitaxially on a (highly doped) macroscopic semiconductor substrate; this provides robust samples for scanning tunneling microscopy and spectroscopy (STM and STS). When a STM tip is positioned above a self-assembled quantum dot, a mechanically stable tip/QD/substrate junction is formed, which allows one to perform atomically resolved microscopy. In such a way, the overall shape of the quantum dot, the atomic structure of the wetting layers and dot, and the presence and effect of doping atoms can be studied. The solid that contains the self-assembled quantum dots can be cleaved under ultrahigh-vacuum conditions, enabling cross-sectional microscopy and energy-level spectroscopy (refs 185, 187, 192, 193, 238−240, 242−244, 247−254, 257, and 262−276). Recently, cross-sectional microscopy has been combined with atom probe tomography,[192] which allows one to make detailed cross sections of the atomic structure of the quantum dot combined with tunneling spectroscopy. By measuring the spatially resolved tunneling current at a tip−substrate bias at which the tip Fermi level is resonant with a QD energy level, the squared amplitude of the wave function could be mapped; the presence of nodal planes then enables assignment of quantum numbers to the wave function and the corresponding energy level.[241,260,261,264]

2.5.2. Preparation of a suitable substrate/colloidal QD sample, which is the key to reliable spectroscopy on colloidal QDs. As prepared, colloidal nanocrystalline QDs are in a suspension. To make scanning tunneling microspectroscopy possible, a clean and stable metallic substrate/QD system is required. This has been achieved in two ways: (1) by connecting individual quantum dots to a substrate[277,278] (often an atomically flat (111) Au film) via bifunctional organic linkers such as dithiols or diamines or (2) by the assembly of monolayer arrays of quantum dots on a flat metallic substrate. Examples of the latter are monolayer arrays of CdSe QDs,[7] PbSe QDs dispersed in a CdSe array,[279] and pure PbSe[280] and InAs QD arrays[281] (see below). It should be realized that the formation of reliable QD samples for low-temperature scanning tunneling microscopy and spectroscopy is far from trivial: the system has to be ultraclean, i.e., it must be devoid of loosely bound solvent and capping molecules, as these molecules can jump to the tip, inducing a change of the vacuum tunneling barrier and noise in the imaging and spectroscopy. On the other hand, the substrate/QD/tip junction has to be mechanically stable, a requirement much harder to achieve than with self-assembled solid-state quantum dots. For this reason, gentle annealing is used to evaporate loosely bound molecules and to stabilize the substrate/QD junction, once the sample is brought in the ultrahigh vacuum (UHV) of the microscope (Figure 2). Although colloidal quantum dots as monolithic objects have been imaged reliably with tunneling microscopy providing their overall shape and dimensions, atomically resolved images have not (yet) been obtained. The

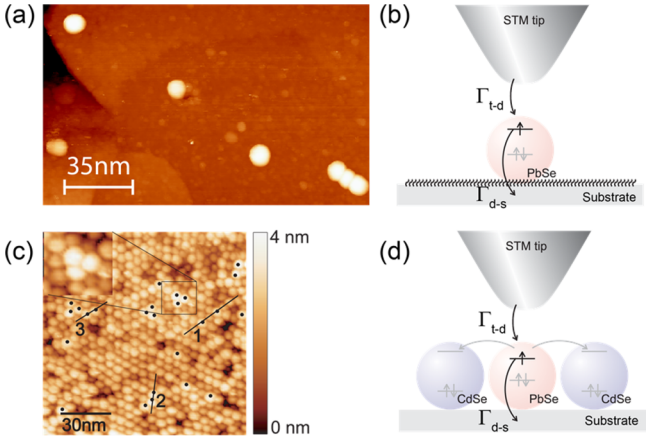

Figure 2. Preparation of colloidal QD/substrate samples for scanning tunnelling microscopy and spectroscopy. (a) STM image of individual PbSe nanocrystals (5 nm core diameter) attached to a Au(111) surface by dithiols. Reprinted with permission from ref 277. Copyright 2005 American Physical Society. (b) Tip/dot/substrate double-barrier tunnel junction when STM experiments are performed on systems such as shown in (a). (c) Monolayer of nanocrystals deposited on an ultraflat graphite substrate. In this monolayer, 7 nm PbSe nanocrystals are dispersed as monomers, dimers, etc. between 6.1 nm CdSe nanocrystals. (d) Schematic of the corresponding tip−dot−substrate junction. Reprinted with permission from ref 279. Copyright 2008 American Chemical Society.

DOI: 10.1021/acs.chemrev.5b00678
Chem. Rev. 2016, 116, 11181−11219

study of the electronic structure of colloidal quantum dots by resonant tunneling spectroscopy is the main issue of the present Review.

3. INTRODUCTION TO SCANNING TUNNELING MICROSCOPY ON SEMICONDUCTOR NANOCRYSTALS (REFS 3−7, 39, 118, 139, AND 277−317)

3.1. Scanning tunneling microscopy

Since its conception, scanning tunneling microscopy (STM) has been one of the main experimental techniques to obtain atomic-scale structural and spectroscopic information on surfaces.[318−322] STM is based on measuring a current due to the quantum mechanical tunneling effect between a sharp probe ("tip") and a conductive substrate. Because of the extreme distance dependence of the tunneling probability, essentially all of the electrons tunnel between the last atom of the tip and the substrate. This results in a current probe that has a diameter of roughly one atomic diameter and is the reason behind the atomic resolution imaging capabilities of the STM. A general introduction to scanning tunneling microscopy and spectroscopy can be found in several books, for instance, "Introduction to scanning tunneling microscopy" by C. Julian Chen (Oxford University Press, ISBN 978-0-19-921150-0) and "Scanning Probe Microscopy and Spectroscopy" by Roland Wiesendanger (Cambridge University Press, ISBN 0521-41810-0).

STM is typically carried out in two different modes: the constant-height and constant-current modes. In the constant-height mode, the STM tip is raster scanned above the surface while keeping the tip z-position constant and recording the changes in the tunneling current. While this mode is useful on atomically flat samples, it rarely can be used on nanocrystal samples because of their roughness (compared to the atomic diameter). In the constant-current mode, a feedback loop is used to adjust the z-position of the tip in order to maintain a constant tunneling current. Recording the z-signal yields a topography image of the sample surface. While the z-signal is related to the actual topography of the sample, it is important to keep in mind that the tunneling current is also influenced by electronic effects.

In addition to the tip−sample distance, the tunneling current depends on the local density of electronic states (LDOS) close to the Fermi level of the sample ρ_s. At a low temperature, the tunneling current can be expressed as

$$I(V, x, y, z) \propto \int_0^{eV_b} \rho_t(E - eV)\rho_s(E, x, y)T(E, V, z)\, dE \quad (1)$$

where ρ_t is the tip density of states, T is the transmission probability, and V_b is the applied bias voltage between the sample and the tip. By differentiating the tunneling current and assuming an energy-independent transmission function and the tip DOS, one obtains

$$\frac{dI}{dV} \propto \rho_s(eV, x, y) \quad (2)$$

That is, the dI/dV signal is directly proportional to the LDOS at the position of the STM tip. This very important result forms the basis for all scanning tunneling spectroscopy (STS) experiments, where the dI/dV signal is used to obtain the energy and the spatially resolved LDOS.

3.2. Scanning tunneling microscopy on semiconductor nanocrystal QDs[3,291]

Here, we discuss the intricacies associated with performing STM and STS measurements on nanocrystals and their self-assemblies. The first step in successful scanning probe microscopy experiments on nanocrystals is the preparation of the sample. This is most often done by either drop-casting or spin-coating the nanocrystal suspension onto a conductive substrate, e.g., highly ordered pyrolytic graphite (HOPG) or a noble metal single crystal. This typically results in self-assembled layers. These layers are mechanically sufficiently stable for scanning tunneling microscopy and spectroscopy. In the case that individual nanoparticles are to be studied, substrate surfaces with chemical anchoring groups such as dithiol-covered Au(111) can be used. Subsequently, the sample is inserted into the UHV chamber that also houses the microscope. Because of the way the sample is prepared, it is inherently contaminated with solvent molecules and free or loosely bound ligand molecules. These moieties on the sample surface can attach to the STM tip, leading to instabilities in the tunnel junction. Hence, after insertion of the sample in UHV, it must be further cleaned. This is most often done by annealing at temperatures <150 °C for several hours, aiming at the evaporation of the loosely chemisorbed contaminations. This annealing procedure does not remove the ligands strongly bound to the nanocrystals. Because these molecules are typically several nanometers in length and have a significant HOMO−LUMO gap, they act as a barrier for electron tunneling. Hence, upon inserting a nanocrystal sample into the microscope and successful cleaning, the situation should be as indicated in Figure 3a.

The tip−nanocrystal−substrate junction is a so-called double-barrier tunnel junction (DBTJ). The barrier between tip and quantum dot consists of a vacuum gap and a shell of ligands, whereas the barrier between the particle and the substrate is mainly due to the ligands. The applied bias V is distributed over these two barriers. In addition, one should consider the rates of electron tunnelling across both barriers: the rate of tunneling from the tip into the quantum dot across the tip/dot barrier (Γ_{in}) and the rate of tunneling from the QD to the substrate out of the QD (Γ_{out}). The ratio of these rates determines the electron occupation in the QD, i.e., the average number of added electrons, a key element in the interpretation of scanning tunneling spectroscopy data, as will be discussed below. First, we need to discuss the energetics of charge carrier addition and the potential distribution in the DBTJ.

3.3. Wave functions and energy levels in semiconductor nanocrystal QDs (refs 11, 18, 19, 53, and 323−343)

Self-assembled and colloidal semiconductor quantum dots are in the first place crystalline compounds, although with limited spatial dimensions, roughly between 2 and 20 nm, i.e., containing ~10^3−10^6 atoms. The energy levels derive from the bonding between the atoms in the crystal structure. Semiconductor nanocrystals differ from molecules in that the atoms are periodically arranged. In contrast to macroscopic crystals, however, they show noticeable confinement of the electron and hole wave functions. The energy levels are computed with methods typically used for larger (macroscopic) crystals, such as multiband effective mass approximations (refs 18 and 333) and atomistic (refs 18, 19, 324, 325, 329, 336, and 344−346) calculations. The (time-independent) wave functions consist of an "atomic" and an "envelope" part, the

DOI: 10.1021/acs.chemrev.5b00678
Chem. Rev. 2016, 116, 11181−11219

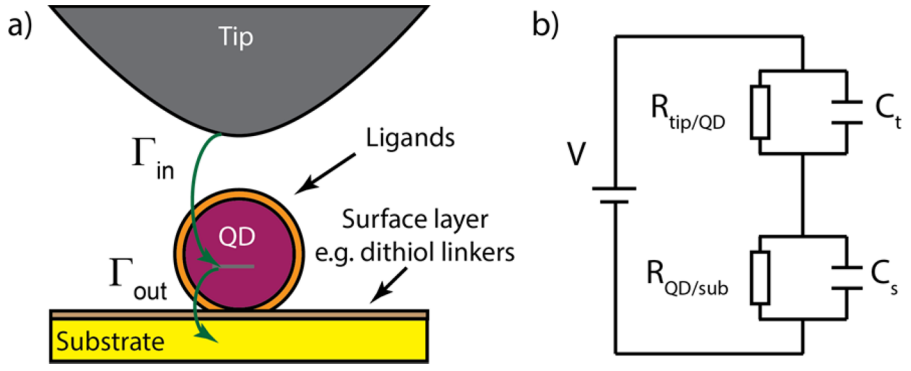

Figure 3. Double-barrier tunnel junction. (a) The tip−QD−substrate system contains two tunnel barriers. There is a barrier between the tip and the QD, which consists of the vacuum gap and the ligand shell around the QD. The second barrier is between the QD and the substrate. The largest contributions to this barrier are the ligands surrounding the QD. In addition, an insulating layer on the surface, e.g., a layer of alkanedithiols to anchor individual QDs, will also contribute to this barrier. (b) The equivalent electric circuit of the double-barrier tunnel junction, V ($=V_{substrate} - V_{tip}$) stands for the applied bias between the substrate and the tip.

latter being a standing wave reflecting the electron (hole) particle confinement, very similar to the particle-in-a-box wave functions:

$$\psi(i, j, k, n) = \varphi_{at}\varphi_{n,l}(i, j, k) \tag{3}$$

Here, i,j,k are the indices of the atomic position in the crystal. The atomic part, φ_{at}, is formed from combinations of atomic orbitals. Typically, the highest filled valence energy levels and lowest empty conduction energy levels are primarily composed of different atomic orbitals. For instance, for the highest valence levels of CdSe, φ_{at} are predominantly composed of the 4p-type orbitals of Se, while the lowest conduction levels are composed of 5s orbitals of the Cd atoms. The envelope wave function $\varphi_{n,l}(i,j,k)$ can be considered as the weight that is given to each atomic wave function depending on the position in the nanocrystal. The envelope wave functions correspond to the standing wave functions in a box with finite energy walls, thus (slightly) extending over the edge facets of the semiconductor nanocrystal. Colloidal nanocrystals show strong electron and hole confinement, with kinetic confinement energy exceeding the thermal energy at room temperature. For colloidal semiconductor nanocrystals, the confinement energies can be in the 100 meV range. Hence, the optical gap between the valence and conduction bands exceeds the bulk value by hundreds of meV and increases with decreasing nanocrystal size. In addition, the energy levels of these systems at the top of the valence band (bottom of the conduction band) are well-separated and can be denoted by the quantum numbers n, l, and m_l that play a similar role as for atoms. For instance, for CdSe nanocrystals, the lowest single-electron conduction level, $n = 1$, $l = 0$, corresponds to a 2-fold spin degenerate S-orbital (envelope function), while the second level, $n = 1$, $l = 1$, $m_l = -1, 0, 1$, consists of six P-orbitals (taking the electron spin into account). This second level is the counterpart of the atomic P-level, $n = 2$, $l = 1$, $m_l = -1, 0, 1$.

3.4. Energetics of electron or hole addition (refs 3, 327, 328, 335, 336, and 347)

In a scanning tunneling microscopy and spectroscopy experiment, charge carriers, i.e., electrons or holes, are temporarily added to the nanocrystal; see section 3.2. To be able to interpret tunneling spectra in a quantitative way, the energetics of addition of electron(s) and/or holes to a quantum dot have to be considered in detail. The model presented below is based on the seminal work of the groups of Zunger and Delerue.

We will discuss tunnelling spectroscopy on a QD with a specific set of degenerate single-particle energy levels. As an example, we consider nanocrystalline QDs with a (nearly) spherical shape and wurtzite or zinc blende crystal structure, such as CdSe QDs. In addition, we only consider the two lowest energy envelope functions $\varphi_{n,l}(i,j,k)$ of the conduction band and the highest state in the valence band. The conduction electron states are the 2- and 6-fold degenerate S-type ($l = 0$) and P-type ($l = 1$) states with energy ε^e_S and ε^e_P respectively. The highest valence state has an S-type envelope function, and energy denoted as $\varepsilon^h_{VB,1}$. The electrochemical potential required to add the first electron to the S-type energy level is given by

$$\mu_{1/0} = E(1) - E(0) = \varepsilon^e_S + \varepsilon_{pol} \tag{4}$$

E(1) and E(0) denote the total energy of the quantum dot with an additional electron in the first electron energy level and in the ground state, respectively. ε_{pol} represents the additional energy that is needed to (temporarily) add an additional charge to the QD. This term can also be understood in the framework of the dielectric mismatch between the QD and its surroundings: this mismatch leads to an electrostatic polarization charge density on the quantum dot surface interacting with the charge of the electron. Under most conditions the dielectric constant inside the quantum dot is larger than that outside the quantum dot, and the polarization energy is positive.[348] The energy to add the second electron to the S-type energy level is given by

$$\mu_{2/1} = E(2) - E(1) = \varepsilon^e_S + \varepsilon_{pol} + \varepsilon_{ee} \tag{5}$$

ε_{ee} accounts for the electron−electron Coulomb repulsion energy between the two electrons with opposite spin in the S-type orbital; it has a contribution that results from the dielectric mismatch, and a direct part as in the bulk. The third electron is added to a p-type orbital, at an electrochemical potential:

$$\mu_{3/2} = E(3) - E(2) = \varepsilon^e_P + \varepsilon_{pol} + 2\varepsilon_{ee} \tag{6}$$

Also the fourth, fifth, and sixth electrons are added to a P-type orbital. Each of these additions add a factor of ε_{ee} with respect to eq 6. Similar arguments hold for the addition of holes to the QD.

DOI: 10.1021/acs.chemrev.5b00678
Chem. Rev. 2016, 116, 11181−11219

The electrochemical potential at which the first hole is injected is given by

$$\mu_{-1/0} = E(-1) - E(0) = \varepsilon^{h}_{\mathrm{VB},1} - \varepsilon_{\mathrm{pol}} \tag{7}$$

The polarization energy is positive in eq 7. No current flows in potential region between the first electron resonance at positive bias and the first hole resonance at negative bias, and also the tunneling conductance is zero. The width of this so-called zero-conductivity gap is given by

$$\mu_{1/0} - \mu_{-1/0} = (\varepsilon^{e}_{\mathrm{S}} - \varepsilon^{h}_{\mathrm{VB},1}) + 2\varepsilon_{\mathrm{pol}} \tag{8}$$

Below, we will compare this "electrical band gap value" with the optical gap of the quantum dot.

3.5. Voltage distribution in the double-barrier tunnel junction[3,291]

From an electrical point of view, the tip/QD/substrate DBTJ can be modeled as two capacitors in series (Figure 3). Here, C_t and C_s are the capacitances of the tip−QD and QD−substrate junctions, respectively. Such a circuit is a capacitive voltage divider network, i.e., the voltage V is distributed over the capacitors. The fraction falling over the tip−QD junction is

$$V_t = V\frac{C_t}{C_t + C_s} \tag{9}$$

and that over the QD−substrate junction is

$$V_s = V\frac{C_s}{C_t + C_s} \tag{10}$$

To first order, both junctions can be modeled as parallel-plate capacitors. Then, the capacitances of the junctions are given by $C_t = \frac{\varepsilon A}{d_t}$ and $C_s = \frac{\varepsilon A}{d_s}$ where ε is the dielectric constant, A is the area of the capacitor, and d_t and d_s are the tip−QD and QD−substrate distances, respectively. Typically, the QD−substrate barrier is smaller than the tip−QD junction, i.e., $d_s \ll d_t$. Hence, $C_t \gg C_s$. Therefore, the largest fraction of the applied bias voltage drops over the tip−QD junction. This fraction, $\eta = V_t/V$, is known as the lever arm; a typical value is 0.8 (see below).

If the lever arm is <1, the quantum-confined levels of the QD shift with the applied bias V with respect to their zero-bias position. Effectively, a larger potential has to be applied to provide the tunneling charge carrier with enough energy to tunnel into the QD. For example, for the CdSe QD discussed in the previous section, the first conduction electron level is observed at $\mu_{1/0} = \eta eV = \varepsilon^{e}_{\mathrm{S}} + \varepsilon_{\mathrm{pol}}$. If the potential distribution in the junction is more symmetric, i.e., the lever arm is close to 1/2, more complicated charge carrier tunneling processes can occur (vide infra). The most common is ambipolar charge transport, i.e., simultaneous tunneling of electrons and holes. This occurs, for example, when the valence hole level shifts above the Fermi level of the substrate in response to the applied bias while simultaneously the Fermi level of the tip is resonant with a conduction electron level. In this regime, electrons and holes can recombine in the quantum dot radiatively and non-radiatively.

From the above it should be clear that, when quantitative information is to be extracted from experimental data, the potential distribution in the junction should be characterized. This can be done by solving the Poisson equation for a realistic tip−QD−substrate junction:

$$\nabla^2 V(x, y, z) = -\frac{\rho(x, y, z)}{\varepsilon} \tag{11}$$

Here $V(x, y, z)$ is the potential distribution in the junction, ε is the dielectric constant, and $\rho(x, y, z)$ is the charge distribution in the junction. In principle, the dielectric constant can also depend on the position in the junction. When the QD is neutral, this equation simplifies to the Laplace equation. When the QD is charged, the charge distribution can be determined by solving the Schrödinger equation for a particle-in-a-box, where the box shape is given by the shape of the QD. In the simulations the bias of the tip and substrate are fixed at ground and V, respectively. The QD is modeled as a dielectric sphere, surrounded by a shell of dielectric material with a different dielectric constant, representing the ligands. Figure 4 shows the potential distribution as calculated for the case where an STM tip is positioned above a single neutral PbSe QD (ε = 227) with a diameter of 4 nm, surrounded by a ligand shell of 0.5 nm (ε = 3). The tip−QD distance and QD−substrate distances are set to 1.0 and 0.5 nm, respectively. In this case, the lever arm $\eta \approx 0.75$. Hence, ~75% of the voltage drops over the tip−QD junction. Note that the potential over the PbSe QD is virtually constant because of the large dielectric constant of PbSe.

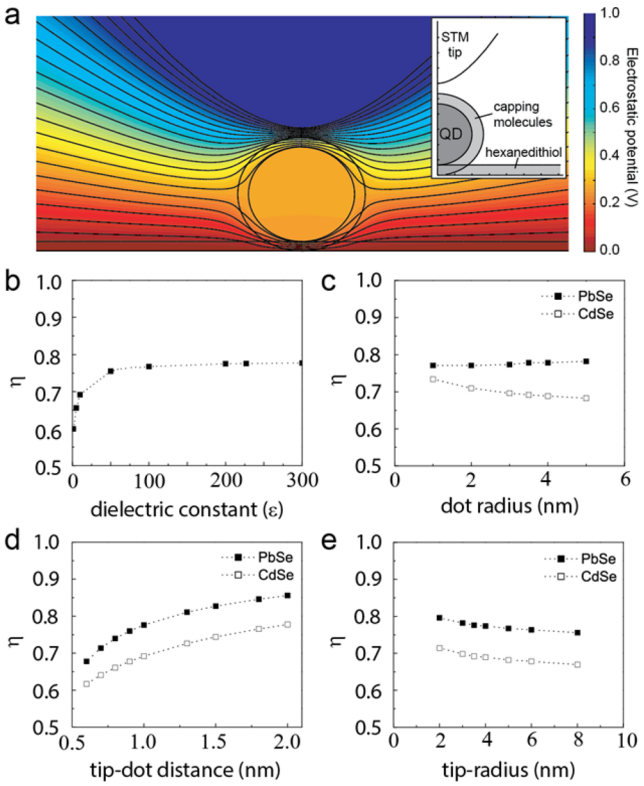

Figure 4. Potential distribution in scanning tunneling microscopy/spectroscopy experiments on QDs. (a) Potential distribution in the tip−QD−substrate junction calculated by solving the Laplace equation for a PbSe QD with a diameter of 4 nm (ε = 227). (b−e) Influence of the dielectric constant (b), QD diameter (c), tip−QD distance (d), and tip radius (e). Unless varied, the following parameters were used: QD radius, 7 nm; tip−QD distance, 1.0 nm. Figures taken from the Ph.D. thesis of Karin Overgaag, Utrecht University, 2008.

DOI: 10.1021/acs.chemrev.5b00678
Chem. Rev. 2016, 116, 11181−11219

Parts b−e of Figure 4 show how the lever arm depends on the dielectric constant, QD radius, tip−radius, and tip−dot distance for CdSe and PbSe QDs, respectively. For dielectric constants below 50, the lever arm depends markedly on the value of the dielectric constant (calculated using a dot radius of 3 nm and a tip−QD distance of 0.5 nm). For PbSe (ε = 227), $\eta \approx 0.75$, and for CdSe (ε = 10), $\eta \approx 0.7$. For CdSe, the lever arm depends appreciably on the size of the QD, whereas the trend for PbSe QDs is much less pronounced. This difference can be traced back to the different values of the dielectric constant of PbSe and CdSe. It is important to note that the lever arm also depends on the radius of the STM tip. For a sharp tip a larger fraction of the bias drops over the tip−QD junction. The relation between the lever arm and the tip radius is almost linear over a range of realistic values (2−8 nm). The sharpness of the tip can be deduced experimentally from topography images. Most interestingly, the lever arm also depends appreciably on the tip−QD distance. This parameter can easily be changed experimentally by adjusting the tunneling current set point. By measuring the energetic position of the tunneling resonances as a function of set-point current, the lever arm can be determined. An accurate method to obtain the lever arm is measuring the voltage separation between the LO-phonon vibronics of a given energy-level resonance. The lever arm is then given by the LO-phonon energy for the semiconductor under study (an intrinsic quantity known in the literature) divided by the experimental voltage difference between two vibronics. This procedure is accurate provided that the phonon energy is not influenced by the limited dimensions of the crystal.[349] Electron−phonon coupling will be discussed in more detail below.

3.6. Energy level spectroscopy under shell-tunneling conditions, $\Gamma_{in} \ll \Gamma_{out}$ (refs 3, 5, 278, 283, and 284)

If the rate of electron tunneling out of the QD is much larger than the rate of electrons tunneling into the nanoparticle, $\Gamma_{in} \ll \Gamma_{out}$, the time-averaged occupation of the QD is zero, i.e., a single electron arrives on the QD and leaves before another one arrives. This regime, in which electron−electron interactions are absent, is known as the *shell-tunneling* regime. At zero bias, the Fermi levels of the tip and sample are aligned. Typically, the Fermi level is located between the first valence hole level and the lowest conduction electron level of the QD (see Figure 5a). By applying a positive voltage to the tip, its Fermi level is raised. In principle, electrons can now tunnel from occupied states in the tip directly to unoccupied states in the substrate. However, because the tip−sample distance is relatively large (5−10 nm), the direct tunneling current is close to zero. Once the Fermi level of the tip becomes resonant with an energy level in the QD, charge carriers can tunnel from the tip to the energy level and then from this energy level to the substrate. As discussed in the previous section, this occurs at an electrochemical potential of $\mu_{1/0} = \varepsilon^e_S + \varepsilon_{pol}$. This additional transport channel results in a step in the measured current at the particular bias voltage that opens this pathway. Steps in the current−voltage ($I(V_b)$) curves correspond to peaks in the differential conductance, dI/dV (V). The latter can be determined numerically from the $I(V)$ curves but can also be measured directly using lock-in techniques. Because electron−electron Coulomb repulsion in the S-level is absent, the degeneracy of the S-level is maintained, i.e., the S-level is measured as one tunneling peak. Upon increasing the bias voltage further, there are no appreciable changes until another resonant tunneling channel becomes

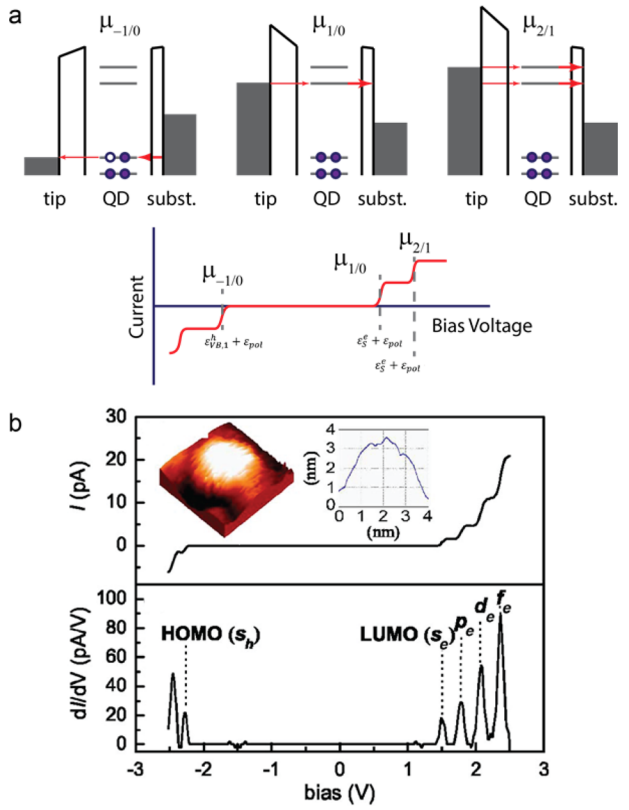

Figure 5. Scanning tunnelling spectroscopy under shell-tunnelling conditions. (a) Scheme of a tip/quantum dot/substrate double-barrier tunnel junction under conditions of shell tunnelling, and cartoon of the expected current I vs bias V curve. Under shell-tunnelling conditions, the tunnelling of electrons at the resonance bias (V1 and V2) into the quantum dot is much slower than tunnelling out of the quantum dot to the substrate (indicated by the thickness of the red arrows). The same holds for the tunnelling of valence holes from the tip into the quantum dot at the opposite bias polarity. The occupation of the conduction energy levels with electrons (valence levels with holes) is close to zero, and Coulomb repulsions are absent. The resonances reflect the single-electron and single-hole energy levels (see text). The zero-conductance gap is given by the band gap of the quantum dot plus two times the polarization energy (see text). (b) Energy level spectroscopy of a CdSe quantum dot chemically bound to a flat gold substrate under shell-tunnelling conditions. The diameter of the dot can be estimated from the height of the microscopic image and is here 3.2 nm (see insets). The top picture shows the tunnelling current I vs the applied bias V, measured at 4.5 K; the steps indicate the resonances reflecting the single-particle energy levels of the quantum dot (see text and panel a). The bottom shows the differential conductance spectrum, i.e., dI/dV vs V; the peaks show the single-particle energy levels. Reprinted with permission from ref 4. Copyright 2006 American Physical Society.

available. In the case of the CdSe quantum dots, the second resonance is due to the degenerate P-levels at an electrochemical potential of $\mu_{2/1} = \varepsilon^e_P + \varepsilon_{pol}$. Similar arguments hold if a negative bias is applied. Now, an electron from the highest occupied valence level can tunnel to the tip electrode, i.e., a hole is injected. The electrochemical potential to add the first hole is given by $\mu_{-1/0} = \varepsilon^h_{VB,1} + \varepsilon_{pol}$. The range in the electrochemical potential in which no current flows, i.e., between the lowest conduction band state and highest valence band state, is called the zero-conductivity gap and is given by eq 8: $\mu_{1/0} - \mu_{-0/1} = (\varepsilon^e_S - \varepsilon^h_{VB,1}) + 2\varepsilon_{pol}$. Hence, the zero-conductivity gap is enlarged by the charging energy of the

DOI: 10.1021/acs.chemrev.5b00678
Chem. Rev. 2016, 116, 11181−11219

electron and the hole, denoted here as $2\varepsilon_{pol}$. Because the charging energy ε_{pol} is similar for all the energy levels, the differential conductance spectrum directly reflects the single-particle density of states, shifted by the polarization term.

3.7. Energy-level spectroscopy under shell-filling conditions, $\Gamma_{in} > \Gamma_{out}$

If the rate of electron tunneling into the QD is larger than the rate of electrons tunneling out of the QD, the time-averaged occupation of the QD is nonzero, i.e., charge accumulates in the QD. In this regime, the energetics of charge carrier addition under shell-filling conditions hold, as discussed in section 3.4. Consider a CdSe quantum dot with doubly and 6-fold degenerate S- and P-type levels, respectively. The conductance spectrum consists of a doublet of S-type resonances and a sextuplet of P-type resonances. The energy difference between the first and second peaks is simply given by the electron−electron repulsion energy ε_{ee}. The energy difference between the first doublet and the second sextuplet is given by $(\varepsilon^e_P - \varepsilon^e_S) + \varepsilon_{ee}$. This is shown schematically in Figure 6a. Energy level spectroscopy under shell-filling conditions has been achieved with colloidal InAs quantum dots.[278,285,286] An example of such a tunneling spectrum is presented in Figure 6b.

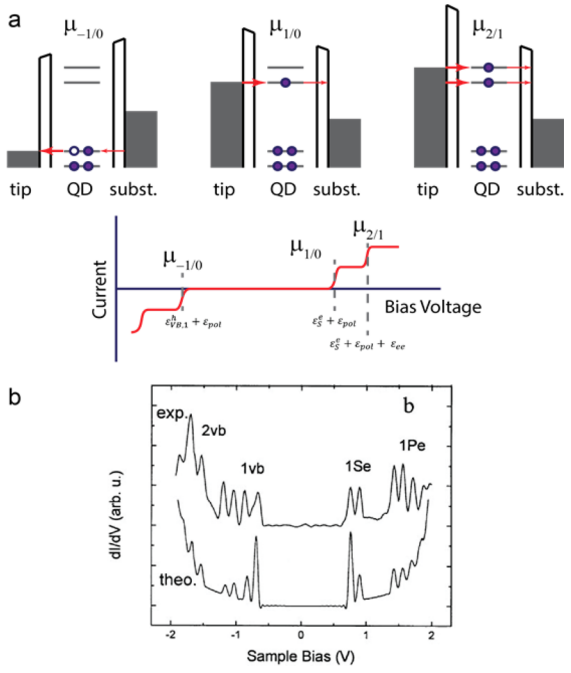

Figure 6. Scanning tunnelling spectroscopy under shell-filling conditions. (a) Scheme of a tip/quantum dot/substrate double-barrier tunnel junction under conditions of shell filling: tunnelling of electrons into the quantum dot is faster than tunnelling out of the quantum dot to the substrate (note the thickness of the red arrows that indicate the tunnelling process). The occupation of the energy levels involved in the tunnelling is thus close to unity (indicated by the filled and open dots for the conduction and valence states, respectively) and determined by the Fermi level of the tip. Coulomb repulsions break the degeneracy of the energy levels. The steps in the current at $\mu_{1/0}$ and $\mu_{2/1}$ reflect the occupation of the conduction S envelope function with a first and second electron, followed by occupation of the P-type envelope functions (not shown). (b) Energy level spectroscopy of an InAs quantum dot (radius, 2.4 nm) chemically bound to a flat Au substrate via dithiol linkers under shell-filling conditions. The experimental dI/dV vs V spectrum (top) shows peaks reflecting the sequential filling of the S and P conduction orbitals at positive potentials and the valence orbitals at negative potentials, in agreement with simulations (bottom). T = 4.2 K. Reprinted with permission from ref 286. Copyright 2000 Elsevier.

The experimental signature for shell filling is the appearance of additional peaks in the differential conductance spectrum with increasing set-point current.[5,6] Under complete shell-filling conditions, the current is determined by Γ_{out}. Hence, the current through the nanocrystal cannot be increased anymore by bringing the tip closer to the QD. In practice, the shell-filling regime is difficult to reach and spectra can be obscured by instabilities of the tunnel junction and strong charge screening by the tip. In addition, if the tip−QD distance is decreased, the tunnel barrier becomes more symmetric. As a consequence, the levels of the QD shift considerably with respect to their position at zero bias. This can lead to ambipolar charge transport, i.e., simultaneous tunneling of electrons and holes.

3.8. Comparison of electron tunneling spectroscopy and optical spectroscopy

Optical spectroscopy is more generally used as a tool to investigate the optoelectronic properties of nanocrystalline QDs. Scanning tunneling spectroscopy and optical spectroscopy are based on different physical phenomena. It is, therefore, instructive to compare the basic physics of both methods.

3.8.1. Spectroscopic transitions. Spectroscopy is based on the fact that an energy quantum induces a transition between two (eigen) states of a quantum system. In *optical* spectroscopy the carrier of the energy quantum is the photon; the absorption of a photon by a QD corresponds to the promotion of an electron from a lower to a higher energy level, and the emission of a photon corresponds to the downward transition of an electron. If we consider more specifically semiconductor quantum dots, an interband optical transition results in the generation of an empty state in a valence energy level (i.e., a hole, h) and an electron (e) occupying a conduction energy level. Upon electron−hole recombination, a photon is emitted:

$$\mathrm{QD} + h\nu \rightarrow \mathrm{QD}(e, h) \rightarrow \mathrm{QD} + h\nu \tag{13}$$

In absorption spectroscopy, the fraction of photons absorbed when the light beam (of given wavelength) passes through the sample is measured (first arrow in the scheme above). In photoluminescence spectroscopy, the number of photons emitted by an excited sample is measured in a spectrally (and time) resolved way (second arrow). We note that the energy of the emitted photon energy can be slightly different from the absorbed photon energy, due to relaxation processes of the excited state QD(e,h).

In scanning *tunneling* spectroscopy, the carrier of energy is the electron. Schematically,

$$\mathrm{QD} + e(\mathrm{tip}) \overset{\Gamma_{in}}{\rightarrow} \mathrm{QD}(e) \overset{\Gamma_{out}}{\longrightarrow} \mathrm{QD} + e(\mathrm{substrate}) \tag{14}$$

Electron transport is driven by the bias V applied between the substrate and the tip. The energy dispersed as heat (or light) per electron cycle is thus given by eV. As outlined above, the zero-conductance gap in scanning tunneling microscopy is given by $\mu_{0/1} - \mu_{-1/0} = (\varepsilon^e_S - \varepsilon^h_{VB,1}) + 2\varepsilon_{pol}$. This gap is to be compared with the (photon) energy of the first allowed interband transition creating an electron in ε^e_S and a hole in $\varepsilon^h_{VB,1}$ (process 13):

$$h\nu = (\varepsilon^e_S - \varepsilon^h_{VB,1}) + 2\varepsilon_{pol} - \varepsilon_{e,h} \tag{15}$$

DOI: 10.1021/acs.chemrev.5b00678
Chem. Rev. 2016, 116, 11181−11219

The electron−hole attraction energy $\varepsilon_{e,h}$ consists of two polarization contributions and a direct attraction energy. This means that the sum $2\varepsilon_{pol} - \varepsilon_{e,h}$ is close to the direct electron−hole attraction energy, which is small (about a few to a few tens of meV). Hence, the optical transition energy is close to the single-particle band gap $h\nu \approx (\varepsilon^{e}_{S} - \varepsilon^{h}_{VB,1})$ while the zero-conductivity gap is enlarged by the charging energy of the electron and the hole, denoted here as $2\varepsilon_{pol}$.[3,350] We should remark here that the *measured* zero-conductivity gap is further enlarged by the bias voltage distribution (lever arm <1) over the double-barrier tunnel junction (see section 3.5).

3.8.2. Selection rules. In optical spectroscopy of semiconductor quantum dots, transitions between filled levels from the (top of) the valence band and the (bottom of) the conduction band are studied. Conservation of angular momentum implies in practice that the angular momentum of the photon is compensated by a change in the angular momentum of the atomic wave function φ_{at}, while the envelope wave function $\varphi_{n,l}(i,j,k)$ remains constant. For instance, in the case of (nearly spherical) CdSe quantum dots, the absorption spectrum shows allowed optical transitions involving the 4P levels of Se and the 5S levels of Cd, while the angular quantum number of the envelope part of the wave function remains unchanged: $l = 0$, $(S_h \rightarrow S_e)$ transition; $l = 1$, $(P_h \rightarrow P_e)$ transition.[342] The absorption spectrum shows these transitions in a more complex form, however, due to the fact that there are three closely spaced valence bands.[9,10,332,351−354] Intraband optical transitions[100,342,345,355−362] between energy levels in the conduction band (valence band) are also allowed; the angular momentum of the photon is then compensated by a change of the angular momentum of the envelope wave function $\varphi_{n,l}(i,j,k)$, for instance, $S_e \rightarrow P_e$, while the atomic wave function remains constant. In electron tunneling spectroscopy, the electron in the tip carries a small linear momentum. However, in the semiconductor nanocrystal that receives the electron, the linear momentum is not a well-defined property. Hence, there are no strict selection rules in scanning tunneling spectroscopy of nanocrystals,[5] and therefore all the energy levels of the quantum dot can be addressed.

3.8.3. Spectroscopic transitions involving defect states. The question arises whether localized defect states in the forbidden gap of the quantum dot can be measured with either optical or electron tunneling spectroscopy. Direct optical transitions that involve defect states have low oscillator strength and can hardly or not be observed in the absorption spectrum. Regarding the emission of photons, the electron (or hole) of the exciton may decay to a localized state, after which electron−hole recombination may occur with the emission of a sub-band-gap photon. Often this transition is weak, and there is a strong competition with nonradiative recombination. In tunneling spectroscopy, the overlap between the localized wave function of a defect level with the wave function of the tip (substrate) is weak, and tunneling processes via localized surface states lead to an overall tunneling current that is much smaller than the tunneling current via eigenstates. However, in the band gap where eigenstates are absent, the current due to tunneling via localized states can be observed. Reports on the detection of midgap states with scanning tunnelling spectroscopy will be discussed below.

In summary, it should be clear that, in optical absorption spectroscopy, mainly allowed transitions with high oscillator strength are detected. In scanning tunneling spectroscopy, a more straightforward measurement of all energy levels of the semiconductor quantum dot is achieved; both the single-particle eigenstates and the degeneracy of these eigenstates broken by Coulomb interactions can in principle be measured. The disadvantage of scanning tunneling spectroscopy is that the spacing between the observed peaks does not directly correspond to the spacing between energy levels (voltage distribution in the junction, charging energy).

3.9. Spatial detection of standing waves related to eigenstates (refs 241, 264, 288, 291, 363, and 364)

The time-independent part of each wave function corresponding to a discrete (valence or conduction) energy level in a semiconductor QD forms a standing wave (see eq 1). If tunneling between the tip and a resonant energy level is the rate-limiting step in current transport, the energy-resolved conductance $\frac{dI(x,y,z,V)}{dV}$ will be decided by the orbital overlap between the tip orbital and the resonant wave function in the quantum dot. Hence, the conductance will be proportional to the amplitude of the wave function $|\varphi_{at}\varphi_{n,l}(i,j,k)|^2$. This corresponds to the broadly used Tersoff-Hamann picture of tunnelling spectroscopy where the dI/dV signal is identified with the local density of states at the position of the STM tip.[365]

It also means that, by measuring the spatially dependent conductance at given bias, the wave functions can be "imaged" or "mapped", showing the nodal planes and the overall symmetry. Measurement of the spatially dependent conductance map can be performed in constant-height or constant-current mode.

Measuring maps of wave functions above atomically flat quantum systems is reasonably straightforward. Energy-resolved wave functions have been measured above graphene nanostructures[366] and graphene ribbons[367] on atomically flat metal substrates, as well as on relatively large flat or stable molecules.[368−372] Also standing wave patterns related to impurity atoms in atomically flat systems can be measured without much difficulty.[373,374] It should be clear that mapping wave functions in a quantum system with a three-dimensional atomic configuration is not straightforward. Self-assembled solid-state quantum dots are mechanically stable, and flat surfaces can be obtained by cleaving. This allows one to perform "cross-sectional" energy-level spectroscopy and wave function imaging.[241,261,375,376] The symmetries observed in the conductance maps have enabled the assignment of quantum numbers to the wave functions and thus helped to identify the QD eigenstates.

Mapping of the wave functions in colloidal nanocrystals is extremely challenging. Nevertheless, results were reported for colloidal quantum dots and for 1-D CdSe rods and heterostructures.[5,288,377] For semiconductor/semiconductor and semiconductor/metal heterostructures, mapping of wave functions has a special scientific interest, as this may reveal the penetration of the eigenstates of crystal A into the space of crystal B, and thus show how wave functions and charge densities spread across an atomically sharp interface.

4. STUDY OF THE ENERGY LEVELS OF QUANTUM DOTS AND QUANTUM DOT ARRAYS OF LEAD-CHALCOGENIDE COMPOUNDS

4.1. Brief history of colloidal nanocrystals of lead-chalcogenide compounds

Since the beginning of the twentieth century, there has been a strong interest in thin films of lead-chalcogenide PbX

DOI: 10.1021/acs.chemrev.5b00678
Chem. Rev. 2016, 116, 11181−11219

(X = S, Se, Te) compounds. With the developments in solid-state physics and chemistry in the second half of the twentieth century, PbX thin films and later on also quantum wells were developed and extensively investigated.[190,303,346,378−407] Because of their small band gap (in the few 100 meV range), these systems have importance for optoelectronic applications in the near-IR as photon detectors.

The lead-chalcogenide compounds have a rock salt crystal structure with considerable ionic character in the Pb−X bonds. The first colloidal suspensions of PbS and PbSe nanocrystals were prepared by combining ionic-type precursors in polar solvents.[63,408,409] In a very similar way to the developments for the CdX compounds, the modern colloid synthesis is using organic solvents; they use a Se precursor and an organo-Pb compound such as Pb-oleate.[25,93,340,361,410−415] The first results emerged around 2000.[340] The as-synthesized nanocrystals can be very monodisperse in size and shape.[414,416,417] The regular shape of the nanocrystals is that of a truncated cube, displaying the most stable [100] facets and, due to the truncation, also smaller [110] and [111] facets.[58,150] Absorption spectroscopy showed discrete interband transitions broadened by the nonuniform size of the nanocrystals and peculiar effects in the electronic structure (see below).[331,411,418−420] The photoluminescence spectrum shows light emission from the lowest energetic exciton(s) with a high quantum yield.[116,121,411,418] This is in line with electronic structure calculations: the rock salt PbX structure and the use of mostly p-type orbitals in the bonding does not lead to dangling bonds at the surface.[337,421] For pure PbSe crystals, surface recombination should not be a dominant process. However, in PbSe nanocrystals solids used in solar cells, electron−hole recombination via midgap states is strong and responsible for the relatively low efficiency; the midgap states are possibly related to the dithiol linker molecules.[422,423]

Nanocrystals of PbX compounds are chemically unstable under ambient conditions. This can be monitored, e.g., by a gradual decrease in the intensity and blue-shift of the light absorption at the energy of the first exciton. The reaction of the surface atoms with molecular oxygen leads to Pb- and Se-oxide moieties and a gradual decrease of the core size. The surface chemistry of PbX compounds has been investigated extensively.[73,424] Nowadays, treatments with NH_4Cl and $PbCl_2$ compounds result in suspensions that are photochemically stable under ambient conditions.[425,426]

4.2. Peculiar electronic structure of lead-chalcogenide nanocrystals

The effects of quantum confinement were, in the first instance, estimated with the k.p 4-band method.[340] This was followed by more advanced atomistic tight-binding[346] and pseudopotential[337,421] calculations. The latter provide a sound picture for the energy levels of PbSe nanocrystals. The band structure of bulk PbSe and a sketch of the quantum-confined energy levels are provided in Figure 7. The other lead-chalcogenide compounds show similar features. The fundamental gap of 0.176 eV (at 0 K) is positioned at the L-points of the Brillouin zone. There are four L-points, which means that the degeneracy of the electronic levels is four times that of the zinc blende and wurtzite structures. Hence, in PbSe quantum dots, the highest valence levels (envelope function S_h) and the lowest conduction levels (envelope function S_e) are 8-fold degenerate. We will use a "group" of levels to indicate the levels with the same envelope function. For instance, in the conduction band,

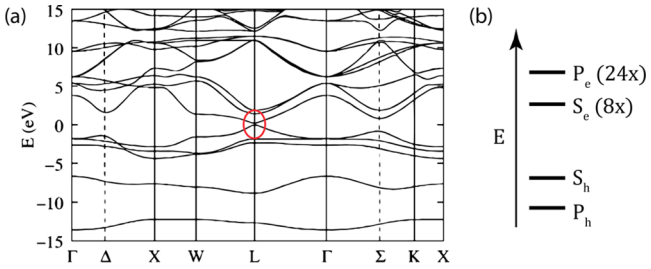

Figure 7. Electronic structure of PbSe. (a) Band structure of bulk PbSe. The Fermi level is located at $E = 0$ eV. The bulk band gap is 280 meV at 300 K. Reprinted with permission from ref 346. Copyright 2004 American Physical Society. (b) Quantum confinement result is a splitting between the electron and hole levels (indicated by subscripts e and h, respectively). The degeneracy of the conduction band states is indicated.

the group of S_e levels is followed by a group of P_e levels, 24-fold degenerate including spin. Quantum coupling of the L-points can lead to a breakdown of the degeneracy and often to groups of *closely spaced* levels with S and P envelope functions.[346,427] This is a critical feature of PbSe nanocrystals, which becomes gradually more important with smaller sizes of the nanocrystals. The atomistic theories can explain the features in the absorption and emission spectra, including the recombination dynamics. The bands at around the L-point show a parabolic dispersion between kinetic energy and wave vector close to the L-points but evolve to a nearly linear relationship further away from the L-points.[346] The effective masses of the PbX compounds are low. This leads to a Bohr radius of the lowest exciton of PbSe of 46 nm. Thus, confinement effects are expected to be strong. This is in line with the band gap of the PbSe nanocrystals that varies from ∼0.2 eV (very weak confinement) to ∼1.5 eV at a size of 2 nm. It is also important to realize that the confinement away from the L-points is weaker, due to the nonparabolicity of the bands. Using absorption spectroscopy, Koole et al. could map the effects of electron and hole confinement at the Σ and Δ directions in the Brillouin zone and compare this with the confinement close to the L-points.[420]

4.3. Open questions regarding the electronic structure of PbSe at the beginning of 2005

4.3.1. Interpretation of the absorption spectrum. The availability of suspensions with monodisperse nanocrystals of a well-defined size enabled the study of the optical transitions in detail and the comparison of the observed transitions with calculations. It appeared that the absorption spectrum showed several peaks due to interband transitions; the first peak reflects the allowed S_h-S_e transition of lowest energy. The second peak, however, was not understood as its energy was systematically lower than that calculated for the allowed P_e-P_h transition; this was so for k.p as well as for atomistic calculations. Research groups using k.p theory proposed that possibly the second absorption peak is due to a forbidden S_h-P_e (S_e-P_h) transition.[339,411,428] Atomistic theories, however, showed that the oscillator strength of the S_h-P_e (S_e-P_h) transitions is really negligible.[337,346] Thus, the second optical interband transition in PbSe quantum dots was an unsolved question. Energy-level spectroscopy of PbSe nanocrystals helped to solve this issue. It should be noted that a similar issue exists in the interpretation of the absorption spectra of PbS quantum dots.[312]

DOI: 10.1021/acs.chemrev.5b00678
Chem. Rev. 2016, 116, 11181−11219

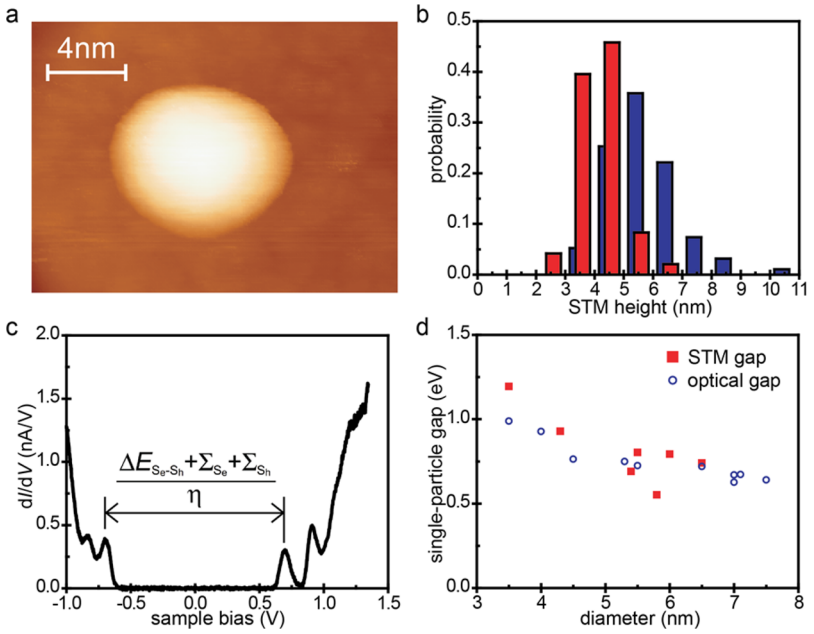

Figure 8. Scanning tunneling microscopy and spectroscopy on individual PbSe quantum dots. (a) Image obtained by scanning tunneling microscopy of an individual colloidal PbSe nanocrystal immobilized on a gold surface by dithiol linkers. The size of the nanocrystal can be measured by the STM height at constant current. (b) Occurrence of STM heights measured for two batches of PbSe quantum dots. The red results pertain to a batch for which the average diameter obtained from TEM analysis was 4 nm, and the blue results are for a batch with average TEM diameter of 5.3 nm; the measured STM height agrees well with the TEM data. (c) Shell-tunneling conductance spectrum obtained above a PbSe quantum dot of 5.5 nm in size; the peaks at positive bias reflect tunneling through the 8-fold S_e and 24-fold degenerate P_e levels, respectively. The further increase of the conductance is due to tunneling through the D_e-group of electron energy levels. The resonances at negative bias show the position of the S_h and P_h levels, respectively. The zero-conductance gap measures the band gap. (d) Comparison of the single-particle band gap vs nominal STM height with the optical gap (measured on an ensemble) vs the average TEM diameter. The results are in mutual agreement and agree well with the band gap calculated by the tight-binding method (black line). Reprinted with permission from ref 277. Copyright 2005 American Physical Society.

4.3.2. Degree of intervalley coupling. The electronic structure of the PbX QDs is peculiar, since the energy levels around the fundamental gap at the four L-points show a high degeneracy, four times that of nanocrystals with zinc blende or wurtzite crystal structure. Size-dependent intervalley coupling, however, may break this degeneracy. Below, we show that the degree of intervalley coupling can be estimated from the energy-level broadening in tunneling spectra.

4.3.3. Strength of electron−phonon coupling. The third question regards the strength of the coupling of electrons (holes) with the polar and acoustic phonons in PbX nanocrystals. It should be realized that the coupling of electrons (holes) with polar phonons is usually much stronger than for charge-neutral excitons. Below, it will be shown that the strength of electron−phonon coupling in PbSe nanocrystals can be estimated from the width of the peaks in the tunnelling spectrum.

4.4. STM and shell-tunneling spectroscopy to measure the band gap and the single-particle energy levels of individual PbSe QDs[5,277]

PbSe nanocrystals could be attached to an atomically flat surface of a Au single crystal by linking them to the Au surface with dithiols. Figures 8a and 11a show microscopic images of the nanocrystals attached to the Au surface. The pictures are obtained at sufficiently positive bias (V = 1.5 V) whereby the tunnelling current is relatively stable due to the high density of states in the PbSe QD. The following question arises: how can the size of the imaged PbSe nanocrystals be obtained? The tip height vs the position (at a constant set-point tunneling current) was measured, providing images such as those in Figures 8a and 11a. Cross sections through the microscopic image show that the cross-sectional width is not a good measure for the nanocrystal size due to the tip convolution effect: the finite radius of the STM tip enlarges the apparent radius of the nanocrystal. The height of the cross section vs the base gold surface, however, is not prone to any convolution. In Figure 8b one can see that the statistics of these STM heights agree well with the average TEM diameters of 4 and 5.3 nm measured for two batches of nanocrystals. The STM heights are nicely distributed around these main values. This is further demonstrated in Figure 11a, which shows an image of a gold sample that was brought into contact with a mixed nanocrystal suspension with nanocrystals of 4 different sizes. The STM height statistics in Figure 11b are in agreement with the main TEM diameters. We concluded that the STM height is a reliable measure of the diameter of individual nanocrystals. This allowed us to measure the direct relationship between the size of a given nanocrystal and its energy-level spectrum. It is also clear from the noise-free images that the PbSe nanocrystals attached to the gold substrate by hexane dithiols form mechanically stable junctions and that the measured samples are very clean. This enables reliable tunneling spectroscopy.

Figures 8c and 9 show tunneling spectra that were measured under shell-tunneling conditions and thus display the single-particle energy levels of the quantum dot (see section 3). This was proved by the fact that the conductance spectrum remained unchanged when the tip-to-dot distance was slightly changed. The tunneling spectra show two peaks at positive bias and two peaks at negative bias, reflecting tunneling through electron- and hole-energy levels, respectively. The less well-resolved increase of the conductance at more positive and more negative

DOI: 10.1021/acs.chemrev.5b00678
Chem. Rev. 2016, 116, 11181−11219

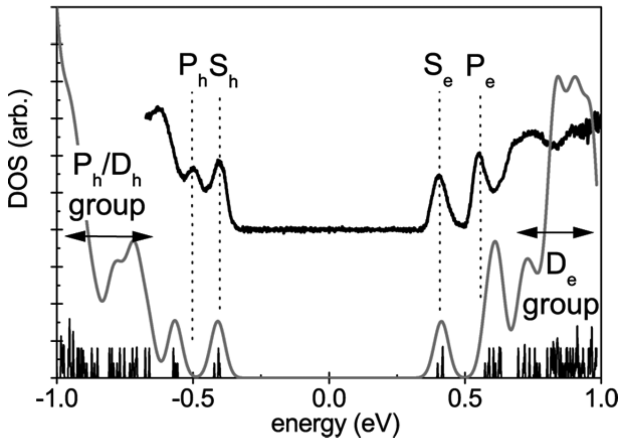

Figure 9. Comparison of a tunneling spectrum obtained above a PbSe quantum dot with a tight-binding calculation. Black line: conductance spectrum obtained above a PbSe quantum dot of 5.3 nm in STM height; the bias is converted to an energy scale by taking into account a lever arm of 0.7. Gray line and black bars: energy levels and resulting density-of-states vs the energy obtained by broadening of each energy level with a Gaussian with a full width at half maximum (fwhm) of 25 meV. It can be seen that the experimental results can be directly compared with the calculated density-of-states of the PbSe quantum dots. The results, however, show that the experimental energy separation between the S_e and P_e levels is considerably smaller than calculated; this also holds for the separation between the S_h and P_h states. Reprinted with permission from ref 277. Copyright 2005 American Physical Society.

bias is due to tunneling through the electron and hole D-levels. The zero-conductance gap is directly related to the single-particle band gap of the material. In the example here, it was estimated that 70% of the applied bias falls over the tip/dot barrier; hence, the "lever-arm" η was 0.7. Using eq 10, we find that the experimental zero-conductance gap ΔV_{zc} (between the first hole resonance and the first electron resonance) is related to the single-particle energy levels by $\Delta V_{zc} = (1/\eta)[\mu_{0/1} - \mu_{-1/0}] = (1/\eta)(\varepsilon^e_S - \varepsilon^h_{VB,1}) + 2\varepsilon_{pol}$ (see eq 8). The electron and hole charging energies (denoted together as $2\varepsilon_{pol}$) can be estimated from the dielectric constants of the PbSe nanocrystal and the surroundings.[328,342] Then, the single-particle band gap $\varepsilon^e_S - \varepsilon^h_{VB,1}$ can be obtained. The single-particle gap derived from the conductance spectra is plotted vs the STM size in Figure 8d. The single-particle gap agrees very well with results obtained from optical spectroscopy, i.e., the first peak in the absorption spectrum of a nanocrystal suspension plotted vs the average nanocrystal size in the suspension. It was explained in section 3 that, in general, the single-particle gap should be close to the optical gap. Hence, the results in Figure 8d show that measurement of the single-particle gap of individual nanocrystals for which also the size is measured in situ by the STM height is a sound procedure.

Now, the resonances (peaks) in the conductance spectrum will be discussed; see especially Figure 9. The first two peaks at positive bias show the first and second groups of electron levels, S_e and P_e, respectively. This is followed by a broad resonance reflecting electron tunneling through levels with a D-envelope function. The two peaks at negative bias reflect tunneling of holes through the groups of valence levels with S- and P-envelope functions, respectively.

Because under shell-tunnelling conditions the resonances provide the single-particle energy levels, the STM data could be used for a better understanding of the second peak in the absorption spectrum, one of the unsolved issues around 2005. In Figure 10, the energy gap between the second (third)

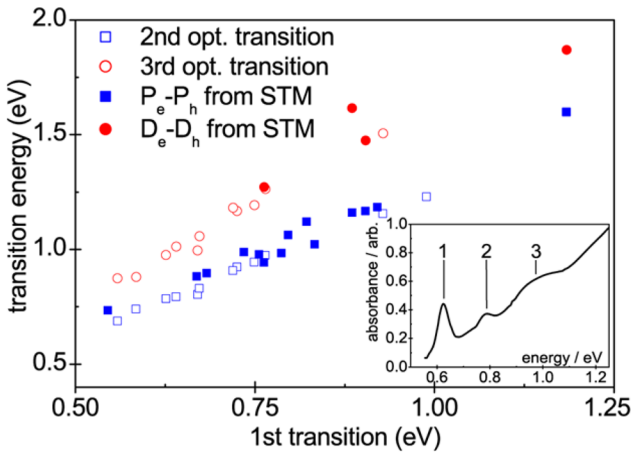

Figure 10. Comparison of valence and conduction energy-level separations obtained from STM and the optical absorption spectra. The P_e–P_h (filled blue squares) and D_e–D_h (filled red circles) energy separations obtained from scanning tunneling spectroscopy are plotted vs the energy of the HOMO (S_h) – LUMO (S_e) transition. In addition, the energy of the second and third peaks in the absorption spectrum (open symbols) is plotted vs the energy of the first peak. There is excellent agreement between the STM data and the optical data, showing that the second peak in the absorption spectrum is due to the P_h–P_e transition. Reprinted with permission from ref 277. Copyright 2005 American Physical Society.

resonance at positive and negative potentials, thus (P_e–P_h) and (D_e–D_h), respectively, are plotted vs the single particle energy gap (S_e–S_h) (filled symbols). The same is done for the optical data: the energy of the second and third peak in the absorption spectrum is plotted vs the energy of the first peak (open symbols). It is obvious that the second resonance in the absorption spectrum corresponds with the P_e–P_h energy derived from the tunnelling spectra. We remark here that atomistic theory shows that the P_h to S_e and S_h to P_e optical transitions have negligible oscillator strength compared to the allowed P_h to P_e transition. In fact, the energy differences between the valence P_h–S_h resonances and conduction P_e to S_e resonances observed from tunneling spectra were found to be significantly smaller than calculated by k.p and atomistic theories. Thus, with the help of scanning tunnelling spectroscopy, the second peak in the absorption spectrum can be attributed unambiguously to the allowed P_e to P_h transition.[277]

4.5. Measuring and understanding the line width of the resonances of individual PbSe nanocrystal[427,429]

With scanning tunneling microscopy and spectroscopy, single quantum dots are addressed; this means that inhomogeneous broadening as present in optical ensemble measurements is absent. Still, the resonances indicating the discrete energy levels are surprisingly broad; see Figures 8, 9, and 11. It is obvious from the spectra in Figure 11c that the widths of the peaks increase with decreasing size of the nanocrystals. Figure 10 d shows that the fwhm of the first electron and hole resonances are ~25 meV for PbSe nanocrystals of 10 nm in size and increase to 150 meV for nanocrystals of 4 nm in size. The widths are much too large to be explained by lifetime broadening of the tunneling electrons. Theory shows that

DOI: 10.1021/acs.chemrev.5b00678
Chem. Rev. 2016, 116, 11181–11219

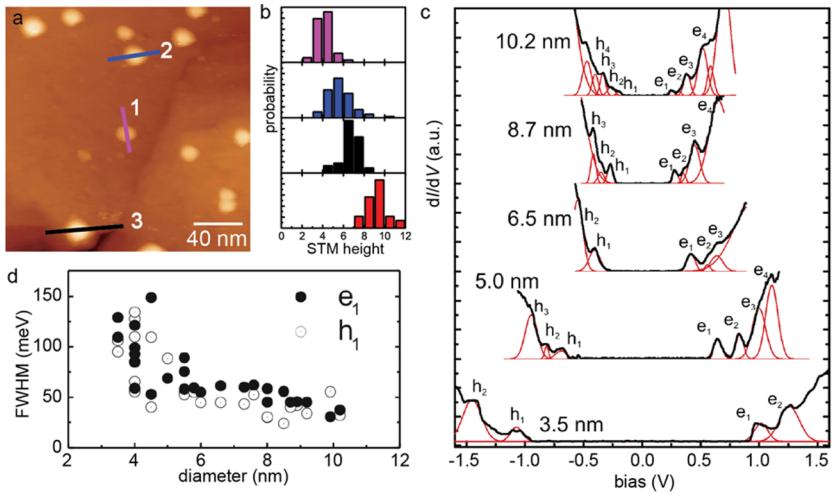

Figure 11. Shell-tunneling spectroscopy of PbSe nanocrystals of different sizes with a focus on the line width of the resonances. (a) PbSe nanocrystals from four different batches attached to a flat Au substrate; the size of the nanocrystals can be obtained from the STM height. (b) Histograms of the STM height of the nanocrystals agrees with the TEM diameters of the four different batches used. (c) Energy-level spectra obtained above PbSe nanocrystals of different sizes; the band gap and energy-level splitting is reduced with increasing nanocrystal size; the tunneling resonances become broader with decreasing particle size. (d) fwhm of the first electron (hole) resonance vs the size of the PbSe quantum dots; the level broadening is due to electron−phonon coupling and intervalley splitting at the L-points. Reprinted with permission from ref 427. Copyright 2005 AIP Publishing LLC.

there are two main contributions to the broadening. The first one is general for all quantum dots and is due to the coupling of the tunneling electrons to the lattice phonons. Coupling of the tunnelling electron to the polar phonons in the PbSe crystal results in a multipeaked and asymmetric resonance. In addition, each of the LO-vibronic peaks on itself is broadened by interaction of the electron with acoustic phonons. The spectra in Figure 10 show broadened peaks in which, however, the vibronic peaks could not be resolved. The average width of the resonances is somewhat larger than the ones calculated. Thus, electron−phonon coupling by itself is not sufficient to explain the line width of the resonances. The second contribution that was proposed is particular for the electronic structure of PbSe: coupling between the four different L-points lifts the degeneracy in the S_e and P_e groups and thus gives an intrinsic broadening within the group. This splitting is small for nanocrystals above 5 nm in size but increases rather steeply with decreasing size below 5 nm. It was shown by Overgaag et al.[427] that the experimental line width of the tunneling resonances of the S_e and S_h energy levels can be explained quantitatively by the convolution of the widths originating from electron−phonon coupling and intervalley coupling.

4.6. Breaking the degeneracy of the energy levels by Coulomb interactions in shell-filling spectroscopy[5]

In a conventional metal substrate/QD/tip double-barrier tunneling junction, the tunneling from the tip to an energy level of the quantum dot is usually much slower than tunneling from the dot to the substrate. In addition, the applied bias falls mostly over the tip/dot junction. This means that shell-tunneling conditions prevail at positive bias (at which the tip addresses the electron levels) and at negative bias (at which the valence levels are addressed) as well. Only when the tip is positioned closer to the dot and the potential drops more evenly over both barriers, anomalous conditions may occur whereby the same levels are involved in the tunneling process both at negative and positive bias. In tunneling spectroscopy of PbSe nanocrystals, shell-filling conditions were obtained in such a way, and a series of equally spaced peaks were observed in the conductance spectrum. The degeneracy of the 8-fold S_h level group was broken down by Coulomb repulsions, and thus the spacing between the peaks is essentially equal to the repulsion energy; small deviations can result from the already broken degeneracy due to intervalley coupling.

Furthermore, we should remark here that, in shell-filling spectroscopy, each resonance addresses a single energy level, which means that it should not be broadened by intervalley coupling. The shape of the hole-resonance peaks under shell-filling conditions appeared to be more asymmetric than under shell-tunneling conditions. This suggests the presence of side peak(s) at the high-energy side; such side peaks are due to the emission of one (or more) LO-phonon(s) by the tunneling electrons. However, there was not enough systematic data available to systematically separate and quantify the strength of intervalley and LO-phonon coupling by a comparison of shell-tunneling and shell-filling spectra of individual PbSe nanocrystals.

4.7. Tunneling spectroscopy on monolayers and bilayers of PbS nanocrystals[312]

Until now, we discussed results obtained on systems in which the nanocrystals were attached to a gold substrate. In a study of the energy levels of PbS nanocrystals, a transparent conducting oxide (ITO) on glass was used as an alternative substrate. The PbS crystals were drop-casted as a monolayer to bilayer on this substrate. It is remarkable that this system was flat enough to result in good quality images of the nanocrystals arranged in a monolayer. Tunneling spectra were measured above individual dots with the substrate cooled to 100 K, while the tip was at room temperature. The size of the nanocrystals was not measured from the height of the nanocrystals, but instead the band gap measured in the tunneling spectra was used. Stable tunneling spectra were acquired, and an example is presented in Figure 12.[312]

The assignment of the resonances according to the authors is indicated in Figure 12. The conductance in the band gap region

DOI: 10.1021/acs.chemrev.5b00678
Chem. Rev. 2016, 116, 11181−11219

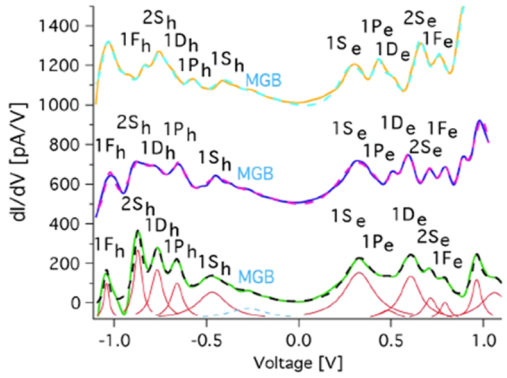

Figure 12. Tunneling spectra acquired over PbS nanocrystals of different size. The nanocrystals were present as a mono- to bilayer on top of a glass/ITO substrate. The nanocrystals were characterized with the width of their gap: top spectrum, 0.65 eV; center spectrum, 0.69 eV; bottom spectrum, 0.75 eV. Reprinted with permission from ref 312. Copyright 2013 American Physical Society.

was attributed to tunneling via midgap states localized at the surface. It should be remarked here that it is not directly expected that localized states are involved in tunneling transport between the tip and the substrate, due to their local (atomic-like) wave functions. The resonances shown in Figure 12 are considerably broadened, broader than those in Figure 11, the case of PbSe quantum dots. This might be simply caused by the larger measurement temperature and, in addition, by breakdown of the degeneracy of the energy levels by intervalley coupling (see explanation earlier for PbSe). Furthermore, because the PbS nanocrystals are arranged in an array, (limited) electronic coupling between the nanocrystals could contribute to the line broadening. The peaks are, however, sufficiently resolved to study the energy of the levels as a function of the measured band gap (Figure 12). A similar analysis as presented above for PbSe was performed to understand the nature of the optical transitions seen in the absorption spectrum. In contrast to the case of PbSe for which we concluded that the second peak in the absorption spectrum reflects the allowed P_h-P_e transitions, it was found here that the P_h-P_e transition have a higher energy than the second peak in the absorption spectrum. Hence, the results obtained for PbS suggest that the second peak might be due to "forbidden" P−S transitions.

4.8. Study of the electronic coupling between PbSe nanocrystals in an array[279,280]

Because tunnelling spectroscopy probes the energy levels (density of states) of a quantum dot sample and the energy-level spectrum can be strongly modified by quantum coupling, tunneling spectra may reveal direct information on the local strength of quantum coupling between the nanocrystals in an array. Such a study was performed for hexagonally ordered monolayers of PbSe nanocrystals.[280] Results are presented in Figure 13.

The spectra show a zero-conductance gap that varied from position to position from nearly the bulk value to larger values, although always considerably smaller than the value obtained with individual PbSe QDs. Moreover, the electron (hole) resonances were considerably broadened, and often a step-like spectrum instead of peaks was found. These features reflect lateral electronic coupling between the energy levels of the PbSe nanocrystals in the array. In another study, a monolayer matrix of CdSe nanocrystals was prepared in which individual PbSe nanocrystals, dimers, trimers, and X-mers were dispersed.[279] Such a configuration enables one to study the degree of quantum coupling in the PbSe quantum dot "molecules" by comparison of the acquired spectra with those of individual PbSe quantum dots. It was assumed that the coupling between CdSe and PbSe nanocrystals can be neglected. The tunneling spectra showed resonances that were broadened and for which the band gap was considerably reduced, compared to these features for individual PbSe nanocrystals. These results quantify the electronic coupling between the nanocrystals in the "nanocrystal" molecule. An advantage of scanning tunneling microscopy with respect to transport characterization of an

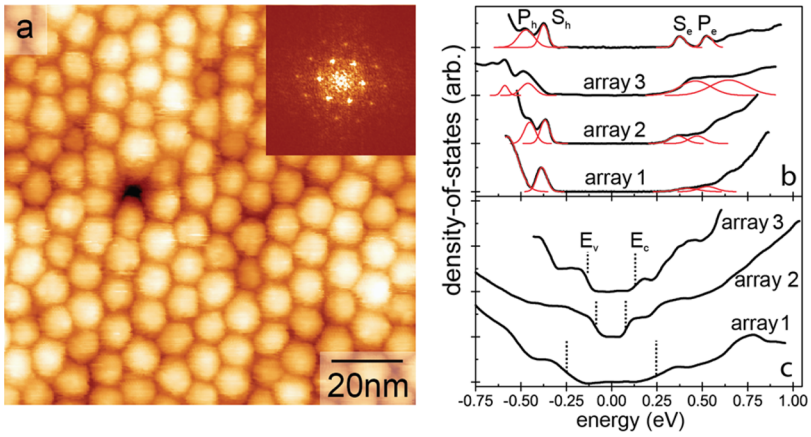

Figure 13. Measurement of the quantum coupling in a monolayer array of PbSe nanocrystals. (a) A typical microscopic picture of the STM height acquired at constant current, showing how the nanocrystals are arranged in the monolayer array; the inset shows a Fourier transform of the image. (b) Representative spectra acquired above three different samples: array 1, a monolayer array of 7.3 nm PbSe nanocrystals (NCs) on Au (111); array 2, a monolayer array of 5.3 nm PbSe nanocrystals on Au (111); array 3, similar to array 2, but separated from the gold surface by a molecular monolayer. The spectrum at the top is that of an isolated PbSe NC attached to Au (111) via dithiols linkers. These spectra show a moderate reduction of the band gap and a broadening of the resonances with respect of that of isolated nanocrystals. (c) Spectra obtained on the same arrays showing a more pronounced reduction of the gap and a step-like increase in conductance spectra, typical for a 2-dimensional quantum well, indicating strong coupling of the nanocrystals. The bias is converted to an energy scale using a lever arm of 0.85. Reprinted with permission from ref 280. Copyright 2006 American Physical Society.

DOI: 10.1021/acs.chemrev.5b00678
Chem. Rev. 2016, 116, 11181−11219

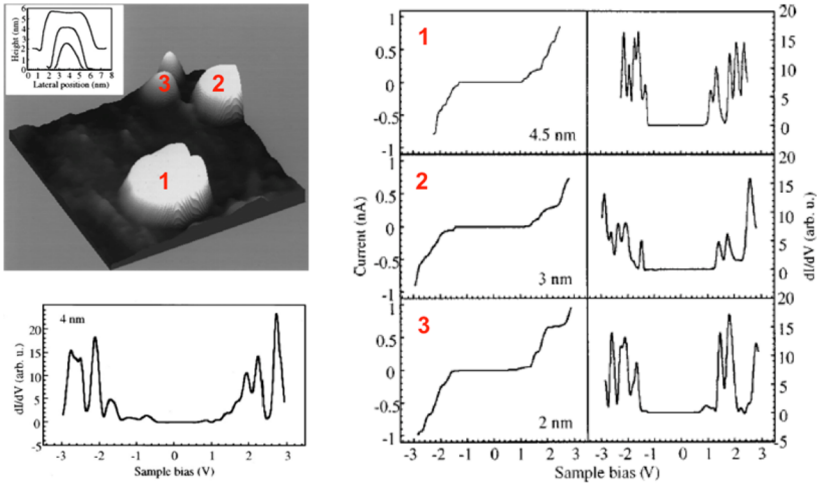

Figure 14. Scanning tunnelling microscopy and spectroscopy of CdSe nanocrystals electrodeposited on a Au substrate. (Left, top) STM image of CdSe nanocrystals of different sizes (see inset) obtained by electrodeposition. (Right) The tunnelling current vs the bias and the derived conductance spectrum of the nanocrystals (indicated with 1, 2, 3 on the microscopic image) under shell-filling conditions: the first doublet at positive bias reflects the S_e level, followed by P_e levels at higher bias. At negative bias the valence levels are measured. The spectra of quantum dot 3 shows a small resonance in the gap due to midgap surface states; a second spectrum showing several small resonances in the gap is presented in the lower left picture. Reprinted with permission from ref 1. Copyright 1999 AIP Publishing LLC.

entire sample is that it is able to measure the degree of quantum coupling in a local way and that the electronic results can be related to the local nanogeometry of the sample.

5. ENERGY LEVEL SPECTROSCOPY OF CDSE QUANTUM DOTS, QUANTUM RODS, AND HETEROSTRUCTURES

5.1. Scanning tunnelling energy-level spectroscopy of electrodeposited CdSe quantum dots[1,2]

In 1999, Alperson et al.[1] reported a first study on the energy levels of wet-chemically synthesized CdSe nanocrystals. The nanocrystals were prepared by electrodeposition on a gold substrate, and the as-prepared sample was incorporated in an UHV STM apparatus for investigations at cryogenic temperatures; the results are presented in Figure 14. Scanning tunnelling microscopy showed the presence of individual nanocrystals attached to the gold surface. The authors provide evidence for the presence of an atomic layer of Se between the gold surface and the CdSe, which might act as a tunnelling barrier. The tunnelling spectra show a well-defined zero-conductivity gap that increases with decreasing size of the nanocrystals. The zero-conductivity gap (see section 3) is the sum of the single-particle gap and the charging energy of the electron and hole. At positive bias, a doublet of peaks was observed, attributed to the two S_e orbitals. This doublet was followed by a series of resonances attributed to the P_e levels. At negative potentials a series of conductance peaks were observed reflecting the valence hole levels. The observed doublet and multiplet peaks show that the degeneracy of the levels is broken by Coulomb repulsions. Hence, the spectra were obtained under shell-filling conditions (see section 3). The spacing between the two S_e resonances provides a direct measure for the electron−electron repulsion energy, ε_{ee}. This value was measured for different sizes of nanocrystals; a value of 0.22 eV was measured for a CdSe nanocrystal of 4.5 nm.

The zero-conductivity gap (eq 11) is the sum of the single-particle gap and the charging energies of the electron and hole. The charging energies of electron and hole together should approximately equal the electron−electron repulsion energy, $2\varepsilon_{pol} \approx \varepsilon_{ee}$. Hence, the measured value of ε_{ee} can be used to correct the zero-conductivity gap for the electron and hole charging energies (see section 3) and obtain the single-particle band gap. The values for the single-particle gaps obtained in this way appeared to be in reasonable agreement with the optical gap measured for CdSe NCs of comparable size.

Furthermore, in some spectra, small peaks could be observed in the energy region of the zero-conductivity gap, attributed to tunnelling through midgap states. It should be remarked that tunnelling through localized midgap states is much less probable then tunnelling through extended eigenstates of the QD (see section 3). Despite the small resonant tunnelling current, tunnelling through such states can be observed if other transport channels are absent, i.e., in the zero-conductance gap corresponding to the band gap of the semiconductor nanocrystal. In later work by the same group, it was convincingly shown that the surface states can be reversibly passivated/activated by the adsorption/desorption of H_2O molecules on the CdSe NC.[2]

5.2. Energy-level spectroscopy on colloidal nanocrystals chemically linked to the substrate[3−7]

5.2.1. Evidence for shell-tunnelling spectra. The Vanmaekelbergh group studied the energy levels of colloidal CdSe quantum dots: in 2001, Bakkers et al. reported a study of CdSe quantum dots of 4.3 nm in diameter, connected to a gold surface by oligo(cyclohexylidene) molecules.[3] Later, quantum dots of different sizes were studied in more detail.[4] When the tip was sufficiently retracted from the CdSe quantum dot under study, the energy-level spectrum was detected under shell-tunnelling conditions. This could be proved by the fact that the tunnelling spectra remain unchanged for varying tip−dot distance (Figure 15). At positive bias, the spectrum showed peaks attributed to the S_e, P_e, and D_e levels, respectively; the energy levels at negative potentials correspond to the valence hole levels.

5.2.2. Quantifying the effects of quantum confinement. The confinement of electrons and holes in CdSe nanocrystals should become more pronounced with decreasing

DOI: 10.1021/acs.chemrev.5b00678
Chem. Rev. 2016, 116, 11181−11219

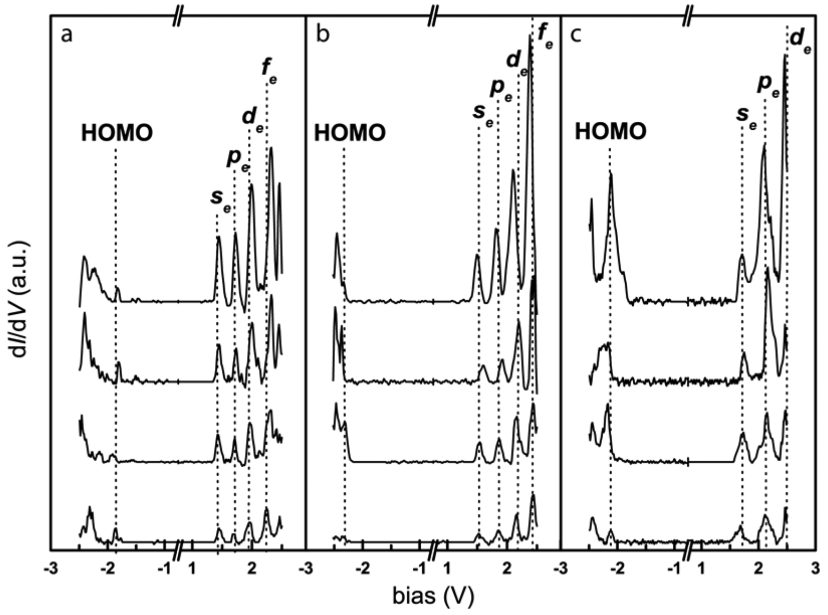

Figure 15. Energy-level spectroscopy of colloidal CdSe nanocrystals attached to a Au substrate via hexane dithiols linkers. (a, b, c) Spectra for CdSe nanocrystal of three different sizes: 5 nm (a), 3 nm (b), and 2.6 nm (c). For each CdSe quantum dot, the set-point current at 2.5 V was varied between 10 pA (lower spectra) and ~100 pA (upper spectra), without any change in the position of the peaks. This shows that the spectra were acquired under shell-tunneling conditions. The zero conductivity gap increases strongly with decreasing size due to quantum confinement and the increasing self-energy (charging energy) of the electron and hole. The resonances at positive bias show the S_e, P_e, etc. single-particle energy levels; the resonances at negative bias are due to valence hole energy levels. Reprinted with permission from ref 4. Copyright 2006 American Physical Society.

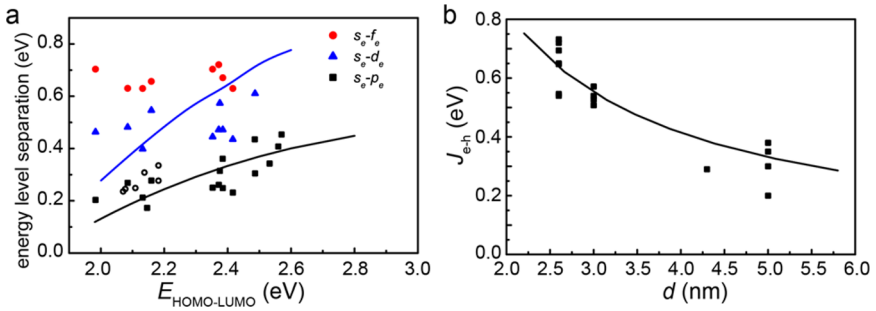

Figure 16. Comparison between the results of scanning tunnelling spectroscopy, optical absorption spectroscopy, and tight-binding theory. (a) The energy separation between the second (P_e) and first (S_e), and third (D_e) and first, single-particle peak as a function of the single-particle gap (obtained from the zero-conductivity gap). The open symbols show the P_e–S_e separation obtained from the intraband absorption spectra. The lines show the results of tight-binding calculations. (b) The electron–hole attraction energy in quantum dots of variable size obtained from the difference in the zero-conductivity gap and the optical gap. Reprinted with permission from ref 4. Copyright 2006 American Physical Society.

size of the nanocrystals. This should be reflected in a larger band gap and a stronger separation between the single-particle energy levels. These features were studied in ensembles of CdSe nanocrystals by absorption and photoluminescence excitation spectroscopy.[354,430] Here we discuss the results on single CdSe nanocrystals of variable size. The energy difference between P_e and S_e (second and first peaks) and D_e and S_e (third and first peaks) plotted as a function of the single-particle gap (Figures 15 and 16) are in good agreement with the values calculated with tight-binding theory. In addition, the energy gaps between the S_e and P_e levels obtained from intraband absorption spectroscopy of charged nanocrystals also agree with the data obtained from scanning tunnelling spectroscopy.[359] From the above results, it is clear that the energy levels of CdSe quantum dots can be detected from shell-tunnelling spectroscopy. With a good estimate of the potential distribution over the tunnelling barrier, the information is quantitative.

5.2.3. Quantifying the electron–electron and electron–hole Coulomb energies. When the tip was brought closer to the dot, the spectrum changed dramatically, and extra conductance peaks were observed. It was understood that—with the tip closer to the dot—the spectra reflect partial shell-filling conditions. From the spacing between the peaks, the electron–electron repulsion energy could be derived; ε_{ee} = 60 meV for nanocrystals of 4.3 nm. This value is much smaller than that obtained by Alperson et al. for electrodeposited quantum dots and also considerably smaller than the values predicted by theory. A possibly explanation will be discussed below.

The electron–hole Coulomb energy, ε_{eh}, obtained as the difference between the zero-conductivity gap and the optical gap (section 3), is shown in Figure 16 (right) for nanocrystal diameters between 5 and 2.5 nm; the values of ε_{eh} range between 250 meV (5 nm in diameter) and 700 meV (2.5 nm in diameter). These values are in good agreement with the values predicted by tight-binding theory and point to considerable

DOI: 10.1021/acs.chemrev.5b00678
Chem. Rev. 2016, 116, 11181–11219

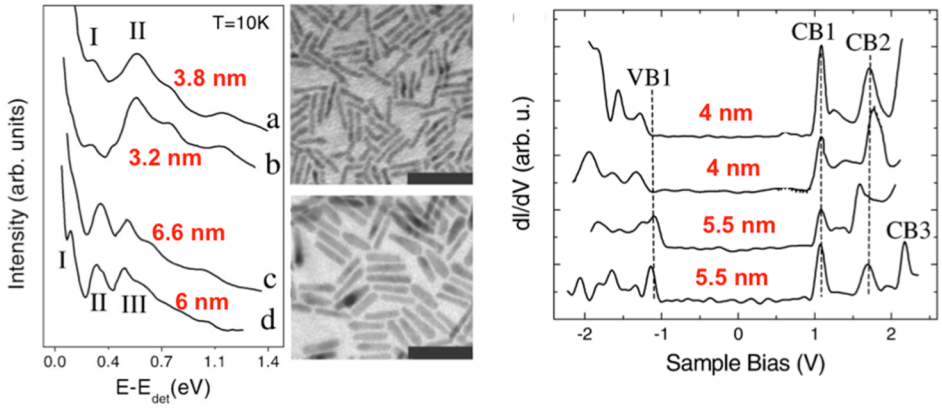

Figure 17. Optical spectroscopy and scanning tunnelling spectroscopy on CdSe quantum rods. (Left) Photoluminescence excitation spectra for CdSe quantum rods with different diameters and lengths between 11 and 60 nm. The spectra are independent of the length of the rods and depend only on their diameter indicated in the figure. (Center) TEM images of two samples of CdSe rods. (Right) Shell-tunnelling spectra of CdSe rods of 4 nm (upper two spectra) and 5.5 nm in diameter with lengths above 25 nm. The spectra are independent of the length of the CdSe nanorods. The zero-conductivity gap and the spacing between the resonances increase with decreasing diameter due to quantum and dielectric confinement in the 1-D cylindrical rod. Reprinted with permission from ref 8. Copyright 2006 American Physical Society.

charging energies, due to the dielectric contrast between the nanocrystal and its environment. In colloidal nanocrystals, dielectric-confinement effects play an equally important role as quantum-confinement effects. We should remark here that the estimation of $\mu_{0/1} - \mu_{-1/0} = \varepsilon^e_S - \varepsilon^h_{VB,1} + 2\varepsilon_{pol}$ from the zero-conductivity gap depends sensitively on the value of the lever arm. As a consequence of a small uncertainty in the lever arm, the values for ε_{eh} may vary by 50−100 meV.

Jdira et al.[4] found that the Coulomb repulsion energy ε_{ee} obtained from shell-filling spectra was systematically smaller in magnitude than ε_{eh} (obtained from the difference between the zero-conductivity gap and the independently measured optical gap; see Figure 16). This contrasts with theory (section 3), which predicts that both Coulomb energies should be comparable. We believe that this anomalous small value can be understood in part by the fact that ε_{ee} is obtained from shell-filling spectra (tip close to the dot) while ε_{eh} is obtained from shell-tunnelling spectra (tip further away). We infer that the metal tip close to the quantum dot might effectively screen the e−e repulsion energy.

5.3. Energy level spectroscopy of colloidal CdSe quantum rods[7,8]

In later work of the Vanmaekelbergh group, Sun et. al measured the energy levels of CdSe rods.[7] Due to the shape anisotropy, the P-levels are no longer degenerate. Moreover, the squared amplitude of the orbitals in the rods depends strongly on the position in the rod. The tunnelling spectra detected all energy levels; the relative amplitudes, however, depended strongly on the tip position above the rod: With the tip positioned above the center of the rod, the S-type and P_z-type orbitals showed the strongest resonances in the conductance spectra; these orbitals have no nodal plane that can be observed in electron tunnelling, and their squared amplitude is maximal in the center of the rod. When the tip was positioned more at the ends of the rod, the lateral P_x, P_y orbitals showed the strongest resonances, while they were practically invisible in the center of the rod. Scanning the tip over the entire rod and measuring the spectra at each position over a broad energy range could, in principle, provide spatial maps of the orbitals.

The groups of Banin and Millo performed a detailed study of the energy levels of colloidal CdSe rods with diameters between 4 and 6 nm and with considerable length, larger than 20 nm.[8] They compared the results of photoluminescence excitation spectroscopy with those of tunnelling spectroscopy; see Figure 17. With PL excitation spectroscopy, the three lowest allowed interband transitions (I, II, III) could be measured. With tunnelling spectroscopy, the three lowest electron resonances (CB1, 2, 3) could be obtained as well as the first hole resonances. The energies of the optical allowed transitions appeared to be independent of the exact length of the rods, indicating that the rods were genuinely 1-dimensional. This was further supported by the tunnelling spectra: the resonances of the rods of 4 (and 5.5) nm in diameter appeared to be dependent only on their diameter; see Figure 17 (right).

Figure 18 shows that the band gap determined from the tunnelling spectra increases with decreasing diameter and can be understood by a multiple-band effective mass calculation.

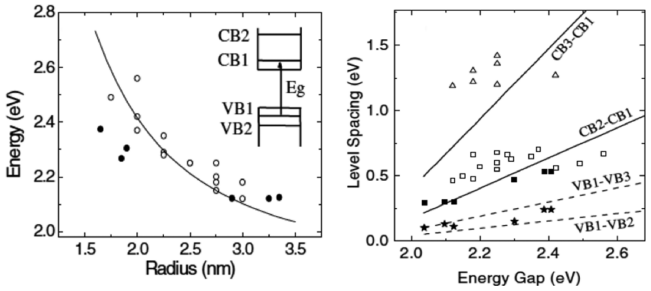

Figure 18. Comparison between the results obtained by optical and scanning tunnelling spectroscopy on CdSe quantum rods. (Left) Single-particle band gap of the CdSe rods determined from the zero-conductivity gap in the tunnelling spectra vs the diameter of the rods. The optical band gaps are presented by filled symbols. The black line presents the results obtained by a multiband effective mass model. (Right) Several energy-level spacings obtained from tunnelling spectra and the PL excitation spectra vs the single-particle band gap $\varepsilon(S_e) - \varepsilon(S_h)$. The most important is the spacing indicated with CB2 − CB1; thus, in fact, $\varepsilon(P_e) - \varepsilon(S_e)$ vs $\varepsilon(S_e) - \varepsilon(S_h)$, which is in accordance with effective-mass multiband theory (black line). The black squares show the (PLII transition − the band gap) vs the band gap. This corresponds to $[(\varepsilon(P_e) - \varepsilon(P_h)) - (\varepsilon(S_e) - \varepsilon(S_h))]$ vs the band gap $\varepsilon(S_e) - \varepsilon(S_h)$. Reprinted with permission from ref 8. Copyright 2006 American Physical Society.

DOI: 10.1021/acs.chemrev.5b00678
Chem. Rev. 2016, 116, 11181−11219

The energy difference between the second and first electron resonances [(CB2 − CB1), thus, in the terminology used here, $\varepsilon_P^e - \varepsilon_S^e$] in the tunnelling spectra was plotted as a function of the band gap (open squares), showing again good agreement with effective-mass calculations (black line) illustrating the effects of confinement in the small directions in the rod. In addition, the energy difference (PLII − band gap), thus, $(\varepsilon_P^e - \varepsilon_P^h) - (\varepsilon_S^e - \varepsilon_S^h) = (\varepsilon_P^e - \varepsilon_S^e) - (\varepsilon_P^h - \varepsilon_S^h)$, was plotted vs the band gap (black squares). These results are systematically and slightly lower than the open squares (corresponding to $\varepsilon_P^e - \varepsilon_S^e$), showing the mutual consistency of the PL excitation spectra and tunnelling spectra.

5.4. Measuring the strength of the electron−phonon coupling in CdSe quantum dots and rods[7]

The coupling of conduction electrons (valence holes) with lattice vibrations is an important physical phenomenon in understanding the optoelectronic properties of semiconductors. However, in bulk semiconductors this coupling is rather weak, due to the delocalization of the electron and hole wave functions. In nanocrystal quantum dots, enhanced coupling is expected due to the confinement of the electron and hole wave functions. Tunnelling spectroscopy offers a unique opportunity to study the coupling of single electrons (holes) to lattice phonons.

Already in the tunnelling spectra presented in Figure 15, it can be seen that each tunnelling resonance is asymmetrically broadened. The broadening increases considerably with diminishing size of the quantum dots. Jdira et al.[429] discussed the possible causes of the broadening of the tunnelling resonances: for CdSe NC, it was concluded that the broadening was mostly due to the coupling of tunnelling electrons to (LO) phonons. In a very detailed study by Sun et al.[7], the vibronic progression in each tunnelling resonance could be resolved. The progression is asymmetric and extends to the high-energy side as a result of the emission of one (or more) LO-phonon(s) to the lattice by the electron that tunnels above resonance (see Figure 19b). The vibronic progression is fully understood by the Frölich type electron−phonon coupling and can be quantitatively simulated using tight-binding electron wave functions confined in the nanocrystal incorporated in the classic electrostatic equations. The only free parameter, i.e., the Huang−Rhys coupling strength, can then be obtained. Furthermore, it was observed that the coupling strength is slightly larger for S_e orbitals than for P_e orbitals. This can be understood by the fact that P_e orbitals are slightly more extended in space. Remarkable results were obtained under shell-filling conditions with CdSe nanorods: Both S_e resonances in the doublet peak structure (split by the Coulomb energy of 60 meV) could be resolved; each of the two resonances showed a strong vibronic progression. This result is remarkable and not fully understood, as under shell-filling conditions the current is determined by the rate of electron tunnelling out of the quantum dot.

Although the *e*−phonon coupling strength in nanocrystals depends on the dielectric environment, the LO-phonon energy determining the energy gap between the vibronic peaks itself is an invariant. As a result, the ratio between the measured splittings (Figure 19d) and the true phonon energy should provide an independent measure of the potential distribution. Sun et al. found that $\eta = 0.85$, in excellent agreement with the value calculated using the Poisson equation.

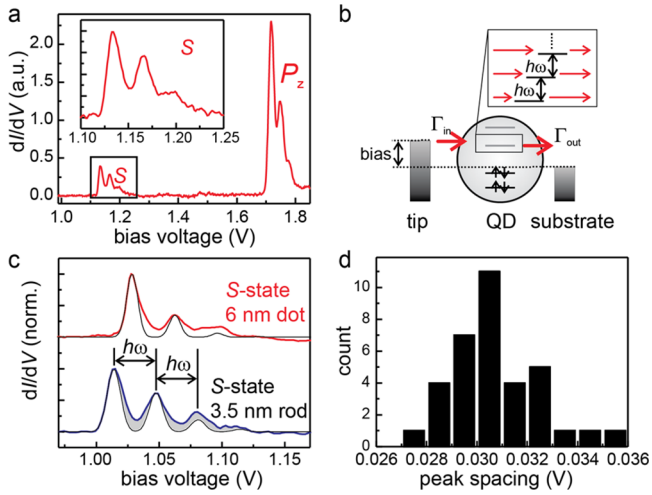

Figure 19. Measurement and analysis of the electron−phonon coupling by the tunnelling resonances of CdSe quantum dots and rods. (a) Tunnelling spectrum of a spherical CdSe nanocrystal of 3 nm in diameter, at positive bias, thus showing the S_e and P_e electron levels. Each resonance shows a vibronic progression due to coupling of the tunnelling electron with LO-phonons of the CdSe lattice, as presented in (b). (c) Vibronic progression of the S_e resonance of a 6 nm dot and a rod with a diameter of 3.5 nm. The black lines are the results of a model calculation based on Frölich coupling between electrons and LO-phonons, with a Huang−Rhys factor of 0.35 for the dot and 0.62 for the rod. (d) Statistics of the splitting between the resonances of the "vibronic" progression with a maximum probability around 30 meV; comparison with the LO-phonon energy (26 meV) provides a way to estimate the potential distribution in the double-barrier tunnelling junction (see text). Reprinted with permission from ref 7. Copyright 2009 American Physical Society.

6. STUDY OF THE ENERGY LEVELS OF COLLOIDAL AND EPITAXIAL III−V QUANTUM DOTS

6.1. Energy level spectroscopy of colloidal InAs quantum dots under shell-filling conditions

One of the first scanning tunneling microscopy experiments on colloidal quantum dots was performed on InAs QDs cross-linked onto a gold substrate using hexanedithiol.[278] In these seminal experiments, Millo and co-workers showed that colloidal QDs can be understood as artificial atoms with particle-in-a-spherical-box−type orbitals[82] and related energy levels that can be studied by tunnelling microscopy and spectroscopy. The results are summarized in Figure 20, which presents the measured (I, V) and dI/dV vs V spectra as well as the size-dependence of the measured resonances. The insets of Figure 20a show a STM topography image of a single InAs QD as well as a schematic of the double-barrier tunnel junction (DBTJ) formed by the tip−QD−substrate system. The corresponding measured (I, V) and dI/dV vs V curves are shown on the top and bottom panels of Figure 20a. The (I, V) curve shows discrete steps corresponding to peaks or sharp resonances in the tunnelling conductance spectrum. These peaks correspond to alignment between the tip Fermi level with one of the QD energy levels as discussed in section 3.

More careful analysis of the peak multiplicities at positive bias reveals that the spectra are measured in the so-called shell-filling limit: there is a double peak followed by several closely and equally spaced peaks. The first peak corresponds to addition of an electron onto the 1S level, $S_e(0) \rightarrow S_e(1)$, and the second resonance corresponds to charging the QD with a

DOI: 10.1021/acs.chemrev.5b00678
Chem. Rev. 2016, 116, 11181−11219

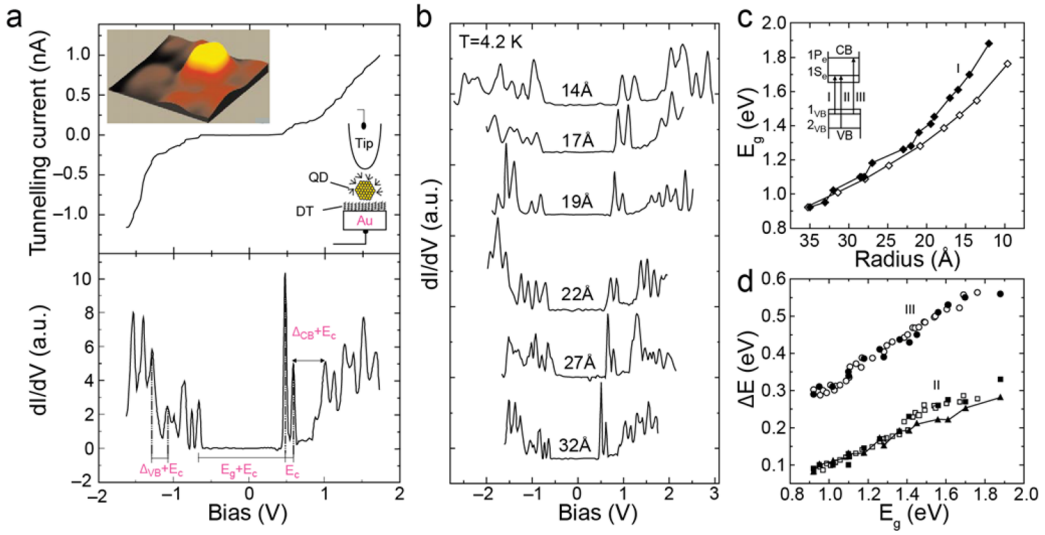

Figure 20. Energy level spectroscopy of colloidal InAs nanocrystals under shell-filling conditions compared with optical measurements. (a) Scanning tunnelling microscopy image (10×10 nm^2) of a single InAs nanocrystal (radius 32 Å) linked onto a gold substrate by hexanedithiol. The (I, V) and dI/dV vs V characteristics show steps and peaks corresponding to tunnelling through the quantum-confined QD orbitals. The spectra are measured under shell-filling conditions. (b) Size evolution of representative dI/dV vs V spectra. The nanocrystal radii are denoted in the figure. (c) Comparison of the size dependence of the optical band gap (transition I) after subtraction of the excitonic Coulomb interaction (open diamonds), with the band gap measured by the STM (filled diamonds). The different optical transitions are indicated in the inset. (d) Comparison of the energies of the excited states as a function of the band gap for tunnelling and optical spectroscopy. The two lower data sets compare the energy $\Delta E = \varepsilon^h_{VB,1} - \varepsilon^h_{VB,2}$ from STS (filled squares) with the difference between transition II and the band gap transition I (open squares). The two upper data sets show $\Delta E = \varepsilon^e_P - \varepsilon^e_S$ from STS (filled circles) and the difference between optical transitions III and I (open circles). Also shown is the size dependence of the single-electron charging energy from the tunnelling data (filled triangles). Reprinted with permission from ref 278. Copyright 1999 Macmillan Publishers Ltd.

second added electron $S_e(1) \rightarrow S_e(2)$. The energy separation between these peaks gives the electron−electron interaction energy ε_{e-e} (more precisely, the bias difference between these peaks is related to the ε_{e-e} by scaling with the lever arm of the junction $\eta\Delta V_b = \varepsilon_{e-e}$). Before reaching the second set of resonances, the bias voltage has to be raised to fulfill the resonance condition corresponding to the transition $S_e(2)P_e(0) \rightarrow S_e(2)P_e(1)$. The spacing between the second and third peaks corresponds to the energy-level separation between the S_e and P_e levels and again the $e-e$ interaction: $\eta\Delta V_b = \varepsilon^e_P - \varepsilon^e_S + \varepsilon_{ee}$ (see section 3.4). In principle, there should be six equally spaced resonances corresponding to the P_e levels, which results from the 6-fold multiplicity of this particle-in-a-box state with angular momentum $l = 1$; the spectra show 3−5 of these resonances. The resonances at negative bias corresponding to tunnelling through the valence band states are typically not as structured, which reflects the more complicated valence band structure of the III−V materials with the light, heavy, and split-off hole levels. It should be remarked here that, in another report by Katz et al., it was demonstrated that in STM experiments on InAs dots deposited on HOPG, it was possible to tune the response between shell filling and shell tunnelling by tuning the tip−sample distance.[284] This is very similar to what has been achieved with CdSe quantum dots.[4]

Figure 20b−d summarizes the size-dependence of the energy levels of the InAs QDs. As the dot size is made smaller, the energy-level spacings, the gap, and the charging energies are all increased due to quantum confinement and dielectric confinement. Tunnelling spectroscopy experiments on single QDs can be directly compared with optical experiments on QD dispersions (photoluminescence excitation spectroscopy, PLE) as illustrated in parts c and d of Figure 20. The optical gap is compared to the STM gap in Figure 20c. As discussed in section 3, the difference in these quantities is the $e-h$ attraction energy that makes the optical gap smaller than the STM transport gap. After taking this effect into account, the optical data overlay with the STM data. Similarly, the higher optical transitions can be compared with tunnelling spectroscopy results (Figure 20d), demonstrating again very good correspondence between the different types of experiments. The work by Banin et al. was the first to demonstrate that the QD energetics could be probed on the single QD level and that those results matched the ensemble averages obtained by optical measurements.[82]

In a recent study by the Banin and Millo groups,[308] InAs nanocrystals doped with Au, Ag, and Cu were investigated using tunneling spectroscopy. In analogy to bulk semiconductors, the authors demonstrated that colloidal quantum dots can be n- or p-type doped. This was followed by observing the shift of the quantum-confined levels with respect to the Fermi level using tunneling spectroscopy: in the case of Cu-doping, the onset of the conduction band states nearly merged with the Fermi energy, consistent with n-type doping. On the other hand, the Fermi level is much closer to the onset of the valence band states for the nanocrystals with Ag-doping, signifying p-type doping in this case. In addition to these effects, the authors also found evidence of the role of strong quantum confinement leading to localization of the impurity wave functions as well as disorder effects leading to band-tailing in small NCs.

6.2. Energy level spectroscopy and wave function mapping on colloidal nanocrystals of III−V compounds

6.2.1. Colloidal InAs/ZnSe core/shell quantum dots.[288] In a subsequent report, Millo et al. studied the effect of a ZnSe shell on the electronic properties of InAs QDs. They

DOI: 10.1021/acs.chemrev.5b00678
Chem. Rev. 2016, 116, 11181−11219

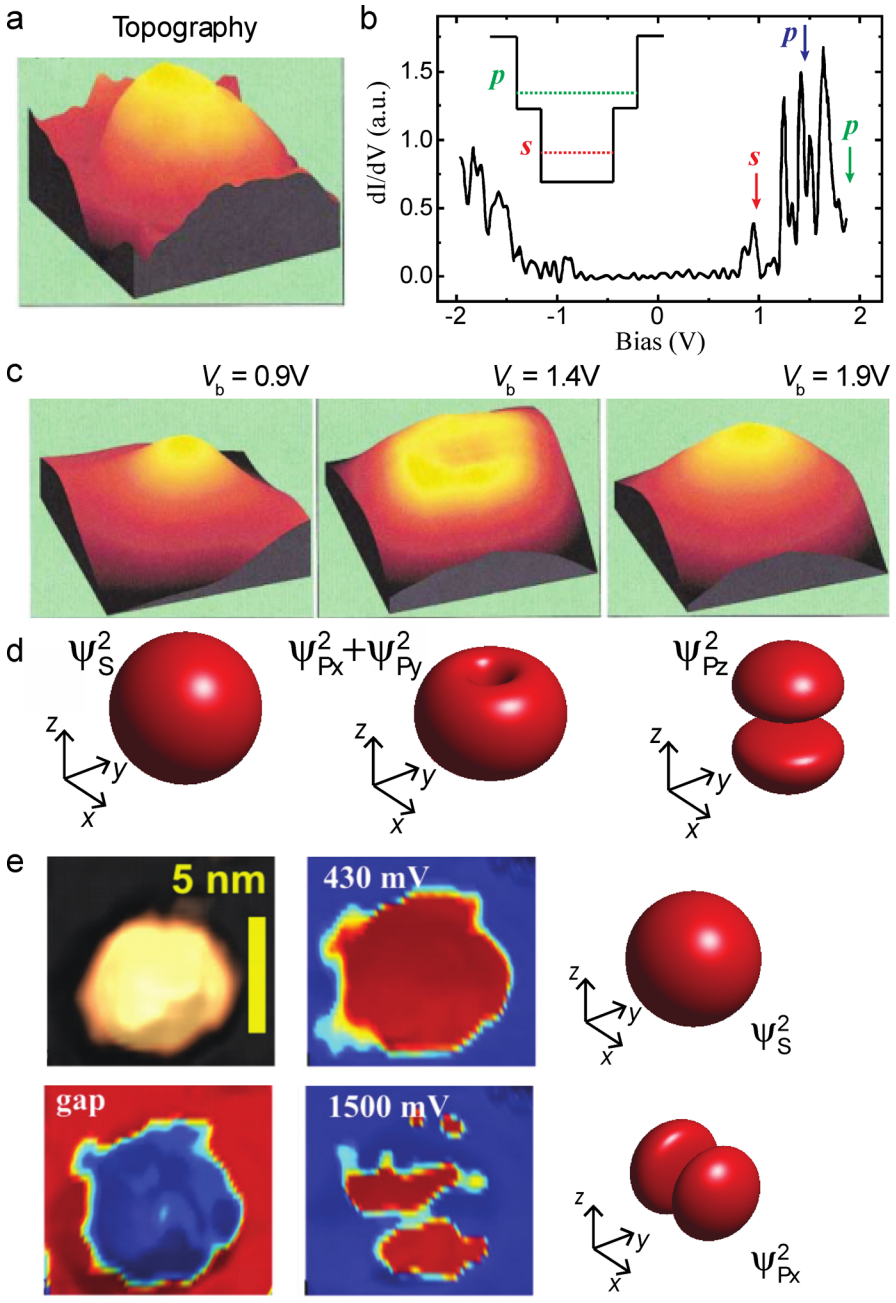

Figure 21. Visualizing the quantum-confined wave functions in colloidal InAs/ZnSe core/shell quantum dots. (a) 8 × 8 nm^2 topographic image of a single InAs/ZnSe core/shell quantum dot. (b) dI/dV spectrum acquired on an InAs/ZnSe core/shell QD having a 6 ML shell. (c) Current images obtained simultaneously with the topographic scan at three different bias values denoted by arrows in (b) and indicated above the images. (d) Schematics of the different quantum-confined wave functions visualized in (c). Reprinted with permission from ref 288. Copyright 2001 American Physical Society. (e) (Top left) Topographic image of a colloidal InP quantum dot immobilized on an Au(111) single crystal using hexanedithiol. (Middle and bottom left) Wave function maps measured by spatially resolved dI/dV spectroscopy corresponding to the voltages in the gap and at the first (430 mV) and second (1500 mV) resonances, respectively. (Right) Schematics of the quantum-confined wave functions visualized in the experimental maps. Reprinted with permission from ref 364. Copyright 2009 John Wiley & Sons, Inc.

found that the S_e to P_e energy-level spacing was reduced by the introduction of the shell; the P_e state can penetrate the shell more than the S_e state, which reduced the quantum-confinement effect and, consequently, the energy splitting between these states. In the same paper, the authors demonstrated that it was possible to use the spectroscopic imaging capability of the STM also on these extremely complicated objects and to directly visualize the envelope wave functions of the QD energy levels. These results are displayed in Figure 21a–c.

Parts a and b of Figure 21 show the topographic STM image and a dI/dV vs V spectrum measured on the QD, respectively. The spectrum is again measured under shell-filling conditions so that each resonance corresponds to an addition of an extra electron into the QD. Quantitative comparison of the spectra for different shell thicknesses indicated that the band gap is nearly unaffected by the shell growth, in accordance with optical experiments. On the other hand, the S_e–P_e level separation is substantially reduced. These observations are consistent with a

DOI: 10.1021/acs.chemrev.5b00678
Chem. Rev. 2016, 116, 11181–11219

model where the S_e state is confined to the InAs core region, while the P_e level extends to the ZnSe shell (Figure 21b, inset). This implies that the energy of the P_e level is reduced upon increasing shell thickness, whereas the S_e level does not shift much. Because of the large valence band offset between InAs and ZnSe, the VB edge state also remains intact. Therefore, the band gap is nearly unaffected by the shell growth.

The spatial extent of these quantum-confined states was directly probed in real space by STM by bias-dependent current imaging experiments. This means that first a dI/dV spectrum is acquired to determine the bias voltages corresponding to the various resonances. Then, a topographic image was measured at a bias value above the S_e and P_e states (V_b = 2.1 V, Figure 21a) simultaneously with three current images. At each point of the topography scan, the STM feedback circuit was disconnected and the current was measured at three different biases: V_b = 0.9 V, V_b = 1.4 V, and V_b = 1.9 V. These values are indicated in the dI/dV spectrum (Figure 21b) and correspond to the S_e state, within the P_e multiplet, and above the P_e multiplet. The topographic and current images are all measured with the same constant local tip−QD separation. Surprisingly, the current images show spatially dependent features in contrast to the expected response under shell-filling conditions. The authors suggested that the main factor determining the current is the tunnelling probability into the different quantum-confined orbitals, which is related to the square of the relevant wave functions at the tip position.

Comparing the current images, pronounced differences are observed in the extent and shape of the maps corresponding to the S_e and P_e states. The S_e state (Figure 21c, left) is localized to the central region of the QD, while the images corresponding to the P_e states extend out to the shell (Figure 21c, middle and right). The current images can be compared to the calculated QD envelope wave functions shown in Figure 21d.[278] Isoprobability surfaces are shown for the 1S state (Figure 21c, left), for a combination of the in-plane P_e states $(P_{e,x})^2 + (P_{e,y})^2$, having a toroid shape (Figure 21c, middle), and for the $P_{e,z}$ state (Figure 21c, right). The calculated probability density for the S_e state is spherical in shape and mostly localized in the core, consistent with the experimental image. The different shapes observed in the current images were assigned to different combinations of the probability density of the P_e components. A toroid shape can be obtained by a combination of the in-plane 1P states $P_{e,x}$ and $P_{e,y}$. In a later work, Tews and Pfannkuche explained the energy splitting of the 1 P states by the Stark effect.[431] The Millo group attributed this splitting of the P_e levels to a perturbation due to the specific geometry of the STM experiment leading to a small degeneracy lifting. While the S_e state does also contribute to the measured response, tunnelling through it is suppressed as the state is more localized to the QD core compared to the P_e states. Finally, a spherical shape consistent with summing all the P_e components with equal weights is observed in the current image measured at higher bias (Figure 21c, right).

6.2.2. Colloidal InP quantum dots. Similar wave function mapping experiments have also been carried out on colloidal InP QDs.[364] An example of the STM topography image and wave function maps is shown in Figure 21e. In these experiments, wave function mapping was carried out by positioning the STM tip above an individual QD, stabilizing the tip−surface distance at each point at a given bias voltage (higher than the bias corresponding to the resonances of interest) and current, disabling the feedback control, and measuring both the current and the differential tunnelling conductance dI/dV as a function of the applied bias voltage V. As discussed above, under shell-tunnelling conditions, the dI/dV (V,x,y) signal is to a good approximation proportional to the LDOS.[365] If the energy resolution is better than the energy-level spacing, the measured dI/dV signal corresponds to the square of the wave function at that energy.

The leftmost panel of Figure 21e shows the STM topography image, while the rest of the panels display the dI/dV signal extracted from the spectra taken at each point of the topography image (at the indicated bias voltage). The color scale increases from blue to red, with red regions corresponding to the highest LDOS. For biases corresponding to the energy gap of the QD, the LDOS inside the QD is negligible and appears blue in the map. When the bias voltage is tuned in resonance with the S_e state, the authors observe a roughly circular symmetric intensity distribution. At higher bias, the tip Fermi level becomes resonant with the P_e state and two clear P-like lobes with a pronounced node in the middle are observed. In this case, the authors found no hybridization between the $P_{e,x}$ and $P_{e,y}$ states, as was observed in most cases for InAs/ZnSe core−shell NCs by Millo et al.[288] The loss of degeneracy of the P_e states could be explained by several different mechanisms: an elongated QD shape,[261] the presence of a piezoelectric field,[432] and/or a coupling with the environment. The authors argue that, in their case, the QDs are not elongated (based on STM and TEM) and, due to the absence of strain, piezoelectric effects can also be excluded. This leads them to conclude that coupling with the Au(111) substrate is the cause of this degeneracy lifting of the P_e states.[364]

The wave function mapping experiments on InP QDs were carried out using a low stabilization current to increase the tip−QD distance for two reasons: to work under shell-tunnelling conditions and to ensure the stability of the tip−QD−substrate junction. Indeed, if the experiments are carried out under full shell filling, the total current should be limited by the QD-to-substrate tunnelling and this should not depend on the position of the STM tip. This implies that wave function mapping experiments should not be possible under full shell-filling conditions. The other requirement of the experimental stability is a stringent one: typical grid spectroscopy experiments last ∼10 h, and there should be no structural (or electrical) changes in the tip−QD−substrate junction during that time.

6.3. Scanning tunnelling microscopy and spectroscopy on 2-D arrays of colloidal InAs nanocrystals

Coupling in 2-D assemblies of InAs quantum dots has been investigated by STM[300] in a similar way as for assemblies of PbSe nanocrystals.[280] The results that were obtained corroborated the main results on the PbSe assemblies: (i) a pronounced reduction of the band gap indicative of strong coupling between the wave functions of neighboring QDs, (ii) the coupling increased with the number of nearest neighbors, and (iii) stronger coupling between the conduction band states compared to the valence band states (which can be explained by the lower effective mass of the electrons compared to the holes). Similar effects were observed in InAs nanorod arrays, while CdSe nanorod arrays exhibited a much weaker coupling.[6,281] Finally, coupling was more significant in QD arrays that had been vacuum-annealed, and evidence for the emergence of a 2-D-like level structure was found. This study again highlighted that there were strong variations in the degree of quantum mechanical coupling from one QD to another in

DOI: 10.1021/acs.chemrev.5b00678
Chem. Rev. 2016, 116, 11181−11219

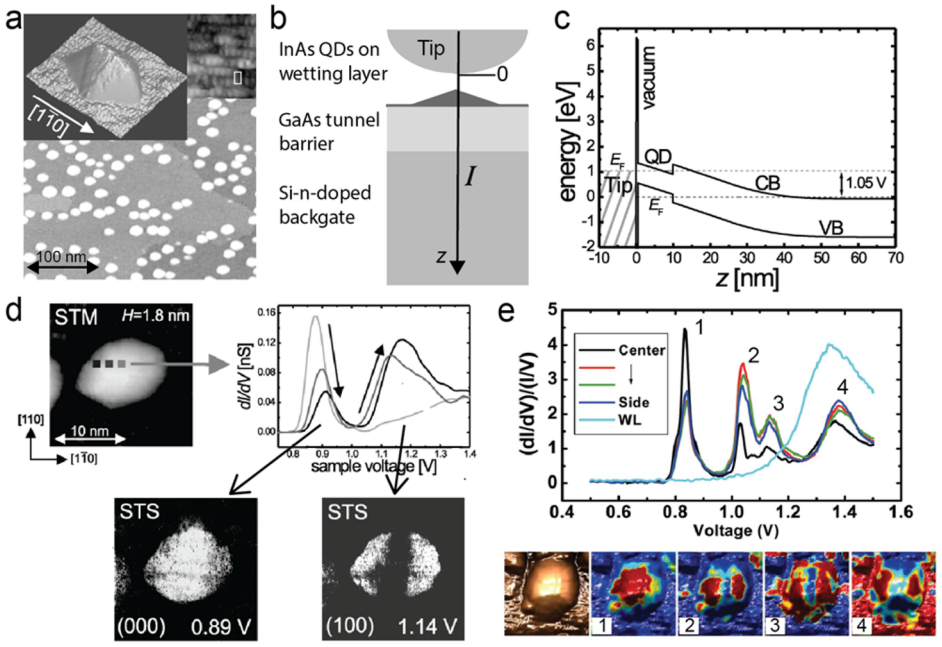

Figure 22. Visualizing the quantum-confined wave functions in colloidal InAs/ZnSe core/shell quantum dots. (a) Constant-current images of a InAs QD sample. The zoom-in shows a typical QD with the [1, −1, 0] direction marked. Inset shows an atomically resolved image on the wetting layer. (b) Sketch of STS measurement of the sample with free-standing InAs QDs, where the tunnelling path I along z is indicated. (c) A 1D calculated band profile along the z direction marked in (b), V = 1.05 V; CB denotes conduction band, VB denotes valence band, and a confined QD state is marked as a full black line. (d) (Top left) Constant-current image of a single QD. (Top right) dI/dV curves recorded at different positions above the QD as marked on the left. (Bottom) Spatially resolved dI/dV vs V data at sample biases of 0.89 and 1.14 V corresponding to the two peaks on the top. Reprinted with permission from ref 241. Copyright 2003 American Physical Society. (e) STS spectra and wave function maps on another QD sample with a less transparent tunneling barrier between the QD and the substrate. (Top) (dI/dV)/(I/V) spectra measured at different positions on a single QD, moving from the QD center to its sides. (Bottom) STS spatial maps of a single representative dot, taken at 840, 1040, 1140, and 1370 mV, for resonances 1, 2, 3, and 4, respectively. The color code represents the STS signal with respect to the topographic STM image on the left-hand side (first panel), increasing from blue to red. The lateral extension of all maps is 30 × 30 nm^2. Reprinted with permission from ref 261. Copyright 2007 American Chemical Society.

the assembly due to the extreme distance sensitivity of the wave function overlap between neighboring QDs.

6.4. Scanning tunnelling microscopy and spectroscopy on solid-state self-assembled quantum dots

6.4.1. InAs quantum dots on a GaAs substrate. Scanning tunnelling microscopy and spectroscopy has also been used to study InAs quantum dots, epitaxially grown on a GaAs substrate by gas-phase deposition. As explained in section 2, these solid-state systems are in many ways simpler for detailed spectroscopy studies compared to the colloidal nanocrystals. They are mechanically stable and do not suffer from loosely bound capping molecules. However, the growth of the quantum dots is rarely carried out within the same UHV system that also houses the STM. Hence, it is important to control the transfer without inducing contamination. The best way is to use a mobile UHV system, a so-called vacuum suitcase, that allows sample transfer between UHV systems without exposure to higher pressures.[241]

A typical STM image of an epitaxial InAs sample is shown in Figure 22a. While in this image only the wetting layer is atomically resolved (it is more difficult to resolve the QD facets due to their tilted surface), some studies have also achieved atomic resolution imaging on the InAs QD itself.[433] This would allow identification of the crystallographic orientation of the different QD facets. A schematic of the STM setup is shown in Figure 22b, and a calculated energy diagram is shown in Figure 22c. The fact that the QDs are deposited on a semiconducting substrate causes considerable differences compared to QDs on a metal. In the present case, the applied bias voltage induces a considerable band bending in the substrate, which affects the lever arm. For example, for the measurements shown in Figure 22 a−d, the lever arm was estimated to be η = 0.18. The band offsets and bending also control the tunnel barrier between the QD and the substrate. The relatively small barrier height results in a large tunnelling coupling, which corresponded to a tunnelling rate of 10^{12} to 10^{13}/s for the experiments shown in Figure 22a−d.

Figure 22d shows a zoomed-in STM image on a single InAs QD and the spectra measured on three different positions on the dot. The spectra show two prominent peaks; while the one at lower energy (bias of 0.89 V) has the highest intensity in the middle of the dot, the one at higher energy (bias of 1.14 V) shows the opposite behavior. These represent the spatial variation of the corresponding quantum-confined energy levels in the epitaxial InAs QD. The slight shift of the resonances toward higher bias on going from the middle to the edge of the QD is related to how the band bending in the substrate (Figure 22c) changes depending on the tip−sample distance.

The wave function intensities in real space can be mapped out in more detail by performing grid spectroscopy, i.e., recording a dI/dV vs V spectrum in each point of the topography scan. The dI/dV intensities at the biases corresponding to the resonances are shown in the lower part of Figure 22d. It is clear that the map at a bias voltage of 0.89 V corresponds to a state with S envelope symmetry. The second resonance has

DOI: 10.1021/acs.chemrev.5b00678
Chem. Rev. 2016, 116, 11181−11219

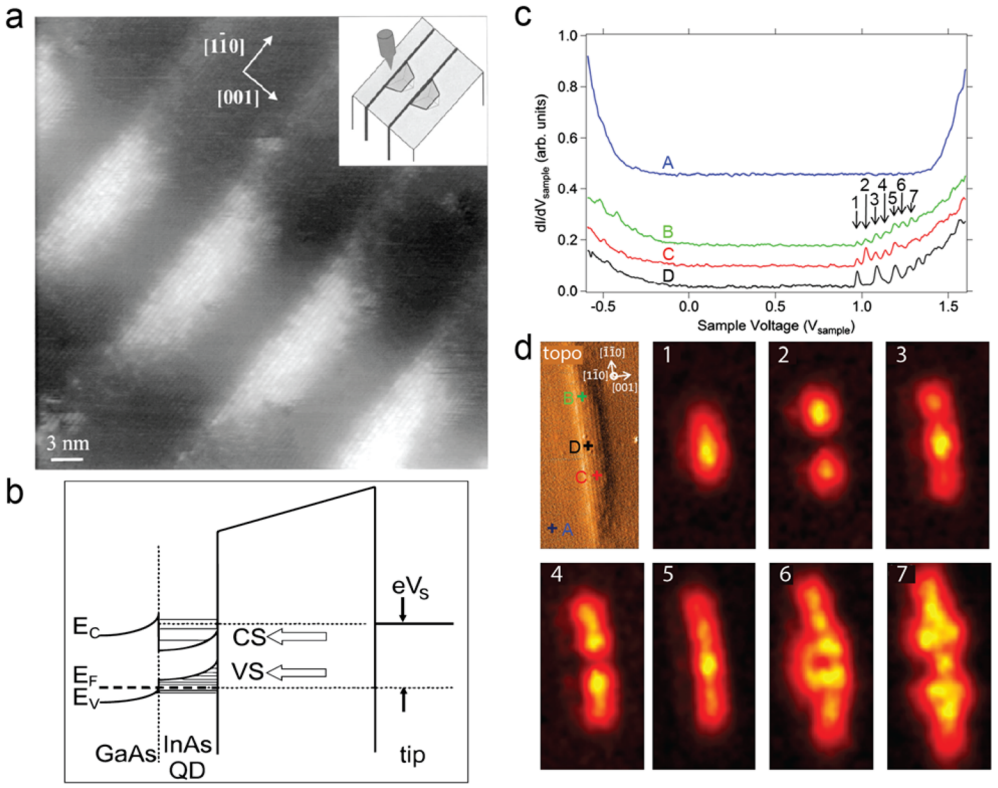

Figure 23. Cross-sectional STM on cleaved quantum dots. (a) STM image of the (110) face of an InAs quantum dot stack layer in GaAs. (Inset) Schematic diagram of STM measurements on cleaved quantum dots. Reprinted with permission from ref 264. Copyright 2000 American Physical Society. (b) Band diagram showing how band bending can be important in the experiments on cleaved QDs; both valence and conduction band states can contribute to the tunnelling current at a positive bias. (c) dI/dV vs V spectrum measured by cross-sectional STM on an InAsP quantum dot at various locations (green, red, and black lines). The background spectrum on bare InP substrate is shown by a dark blue line. (d) Quantum dot derivative image where the locations of STS spectra in panel c are indicated by crosses with corresponding colors and A, B, C, and D. Panels 1−7: 16 × 32 nm^2-sized dI/dV maps measured at 0.974 (1), 1.024 (2), 1.085 (3), 1.143 (4), 1.197 (5), 1.250 (6), and 1.289 V (7) corresponding to the arrows on the dI/dV spectra in (c). Reprinted with permission from ref 252. Copyright 2012 American Physical Society.

P_x symmetry. In these types of epitaxial QDs, the degeneracy of the 1P levels is lifted by QD shape asymmetry and strain.

By controlling the tunnelling barrier between the QDs and the substrate (by making it less transparent), it is possible to achieve higher energy resolution.[261] Spectra measured under these conditions are shown in Figure 22e. The bottom part of Figure 22e shows the spatial variation of the $(dI/dV)/(I/V)$ signal corresponding to the bias voltages of the resonances. As expected, peaks 1 and 2 have S and P_x-like symmetry, respectively. Surprisingly, state 3 shows again a P_x-like symmetry, instead of P_y as expected for the second P-like orbital. It is not possible to explain the wave function sequence (and map 3 in particular) in terms of simple particle-in-a-box states.[261] The authors also excluded the charging of the P_x orbital with a second electron and the occurrence of a phonon replica. The authors argued, based on extensive calculations, that correlation effects play a key role, and quasi-particle wave function concept is needed to understand these features.[261]

In addition to the STM experiments on the epitaxial InAs QDs discussed above, the quantum-confined levels can also be probed using an atomic force microscope (AFM) by detecting the additional electrostatic interaction due to the charges added into the QD (in shell-filling mode).[297] Discrete jumps in the measured tip−QD interaction indicate single-electron additions (removals) to (from) the QD. While the study by Stomp et al. considered large QDs where energy levels are very closely spaced and the charging energy is the dominant energy scale, detecting single-electron charging by AFM should be capable of yielding information on the quantum-confined energy-level positions.

6.5. Cross-sectional STM on epitaxial InAs quantum dots

Buried epitaxial InAs (in GaAs matrix) and InAsP (in InP matrix) quantum dots have also been studied using STM and tunneling spectroscopy.[185,238,239,251,252,434−437] The samples are prepared by cleaving the wafer containing (typically) stacked layers of Stranski−Krastanov quantum dots. Cleavage results in exposure of atomically flat QD cross sections, and hence this technique is called cross-sectional STM. The samples are cleaved in the same UHV system that houses the STM; this results in extremely clean samples, allowing high-resolution imaging and spectroscopy. Typical results are illustrated in Figure 23a, which shows an InAs quantum dot stack in GaAs matrix (the schematic of the experiment is shown in the inset). The quantum dots are lying on bright layers that correspond to the wetting layers. QDs that appear the largest can be assumed to have been cleaved near the dot center. Atomic resolution imaging allows details such as dissolution of the InAs wetting layer and the presence of indium between the dot columns,[438] lattice constant variations, strain, sharpness, and shape of the QD boundaries to be investigated.[185,239]

The energy diagram in a tunnelling spectroscopy experiment is similar to the uncapped epitaxial quantum dots; in addition to the band bending in the substrate, it might also be relevant inside the quantum dots (depending on the their size, material,

DOI: 10.1021/acs.chemrev.5b00678
Chem. Rev. 2016, 116, 11181−11219

and doping of the QDs and the substrate). Depending on the relative band alignment between the QD and the substrate, it is possible (which is illustrated in Figure 23b) that there is simultaneous tunnelling (ambipolar transport) through both the conduction and valence band states of the QD. At positive bias, the tip induces an upward band bending,[243,439] which can bring some of the QD valence states above the substrate Fermi level and result in transport through them while the tip Fermi level is resonant with the QD conduction band levels. Therefore, the valence band states contribute to the tunnel current at positive bias.

The atomically flat surface and high purity of the cleaved QD samples allows for relatively convenient and high-resolution wave function mapping experiments. This is illustrated in Figure 23 c–d on InAsP QDs embedded in an InP matrix. Figure 23c shows dI/dV spectra recorded over different locations of the QD surface.[252] On this particular sample, the flat band conditions are achieved around a bias of 1 V, which implies that band-bending effects can be neglected for the conduction band levels around this bias voltage.[252,439] The relative intensities of the different peaks depend on the measurement positions. This variation reflects the spatial distribution of the wave functions of the quantum-confined energy levels.

These levels can be mapped with recording dI/dV spectra in a grid, with the results shown in Figure 23d. They allow for an unambiguous identification of the symmetry of the successive electronic states of the QD. The first energy levels correspond simply to the quantum-confined levels with S (1), P (2), D (3), etc. symmetries. These levels can be denoted by three quantum numbers (nmp) corresponding to the number of nodes in the [110], [1$\bar{1}$0], and [001] directions. The first 5 states in Figure 23d correspond to the levels (000), (100), (200), (300), and (400) in this notation. The wave functions bow slightly toward the [001] crystal direction, which the authors attribute to either the QD shape or the composition gradient.[252] The maps at higher bias display a more complex structure and can be attributed to superpositions of two electronic states [(n00) and (n'01) states]. The state shown in panel (6) of Figure 23d is attributed to the superposition of (500) and (001) states, and the one in panel (7) is attributed to the (600) and (101) states. The observation of (001) states is due to the relatively large QD heights compared to the typical InAs QD in GaAs matrix systems.[241,252]

7. OTHER COLLOIDAL NANOCRYSTAL MATERIALS STUDIED BY SCANNING TUNNELING MICROSCOPY AND SPECTROSCOPY

While the bulk of the work on tunneling spectroscopy of nanocrystals has concentrated on three materials—InAs, CdSe, and PbSe—the technique has been applied to other nanocrystal materials as well. The methodology is general and can be used to extract the energy-level structure of any colloidal nanocrystal material.

Silicon nanocrystals have attracted enormous interest due to their promise in optoelectronic applications. While bulk Si is a poor candidate for a light-emitting material due to its indirect band gap, silicon nanocrystals can be efficient light emitters.[440,441] The discrete energy levels in silicon nanocrystals have also been studied using scanning tunnelling microscopy and spectroscopy.[315,442−444] Zaknoon et al. described experiments on silicon quantum dots formed using low-pressure CVD and subsequently characterized using STM at room temperature.[442] They interpreted their measurements as being carried out under shell-filling conditions. The results allowed them to extract the single-particle band gaps as well as the charging energies as a function of the quantum dot size. The extracted values were well in line with theoretical predictions based on pseudopotential calculations.[445] In another study, Rosso-Vasic et al. investigated ultrasmall colloidal silicon nanocrystals (average diameter 1.5 nm). Spectroscopy experiments detected a large band gap (~4 eV), consistent with optical absorbance measurements.[443]

The Millo group studied surface-functionalized colloidal silicon nanocrystals using tunnelling spectroscopy.[315] They carried out experiments on different sizes of QDs and investigated in detail the effects of different capping ligands. The energy gaps extracted from the tunnelling spectra increase with decreasing nanocrystal size, as expected due to quantum confinement. The STM experiments yielded results that were consistent with ensemble photoluminescence measurements. The nature of the ligands was found to have an effect on the level alignment: nanocrystals functionalized with NH_4Br or allylamine showed band-edge shifts toward higher energies, suggesting p-type doping. This behavior was rationalized through a combined contribution of the ligands' dipole moments and charge transfer between the Si nanocrystal and its surface groups. These types of shifts were not observed for Si nanocrystals functionalized with the more weakly bound dodecyl or trioctylphosphine oxide (TOPO) ligands.

The Millo group also carried out a similar study with colloidal germanium nanocrystals. The authors investigated Ge nanocrystals with diameters between ~3.0 and 10.5 nm with three types of organic ligands: dodecyl, 3-dimethylamino-1-propyne, and 2-dodecanone.[446] The single-particle band gaps extracted from the tunnelling spectra increase monotonically from 0.97 to 1.67 eV with decreasing nanocrystal size, irrespective of the capping ligands. The smallest quantum dots had a confinement energy of ~1 eV, suggesting that the band gap in Ge nanocrystals will eventually become larger than the band gap of Si nanocrystals with decreasing size. The different capping ligands had no measurable effect on the band gap, indicating they act merely as surface-passivating agents and do not affect the NC interior electrical properties. This also confirms that the observed zero-conductivity gap corresponds to the quantum-confined band gap, not perturbed by the presence of surface states (which would be expected to be strongly affected by the ligands).

The Cu_2S compounds form the basis of a family of more complex compounds that are of significant interest for opto-electrical applications, as they combine quantum confinement with natural electronic doping, even resulting in plasmon resonances in the IR, due to the presence of Cu vacancies. The first (STM) studies on the electronic properties have been performed recently.[447,448]

Finally, we mention experiments on InSb nanocrystals as an example of combining AFM and STM to study quantum-confined energy levels in quantum dots.[449] The authors investigated single InSb quantum dots (QDs) with diameters between 3 and 7 nm such that the topographic measurements were carried out with AFM with metal-coated conductive tips that where then employed as the STM tip in tunnelling spectroscopy experiments. In the investigated size regime, InSb QDs showed strong quantum-confinement effects, leading to the observation of discrete energy levels on both valence and conduction band states and an increase of the measured band

DOI: 10.1021/acs.chemrev.5b00678
Chem. Rev. 2016, 116, 11181−11219

gap with decreasing QD size. While the spectra were measured under shell-filling conditions similarly to InAs quantum dots, the experiments on InSb dots were qualitatively different from other III−V materials: the energy spacing between the S_e and P_e levels was much smaller than expected. Typically, within the effective mass approximation, the S_e−P_e level spacing should be on the order of the S-level confinement energy. However, experiments showed smaller energy-level separation and a larger than expected effective mass. With the help of theoretical calculations, this was interpreted as a result of electron tunnelling through the states connected with L-valley.

8. CONCLUSIONS AND OUTLOOK

This Review presents the current status of using scanning tunnelling microscopy and spectroscopy to extract quantitative values of the energies of quantum-confined states, electron−electron interaction energies, and electron−phonon interaction strengths of individual semiconductor nanocrystals. Most reports are focused on prototypical CdSe and PbSe nanocrystals. It should be clear that the methodology is general and can in principle be used to investigate nanocrystals of any composition and shape. At those fronts, there is still a lot of new territory to be conquered. In particular, colloidal heterostructures that combine two materials in a single colloid are an extremely interesting topic of further study.

Another aspect that can be studied is coupling between different nanocrystals in close-packed assemblies. Here again, groundwork has been laid, but many types of nanostructured systems remain untouched. For example, there has been a lot of work on binary superlattices of colloidal nanocrystals that offer a unique opportunity to bring together completely different materials in a well-defined and controlled manner. Another outstanding topic deals with 2-D semiconductors based on epitaxially connected colloidal nanocrystals with square or honeycomb nanoscale geometry. In addition to the choice of the QD material, these systems have an additional degree of freedom—the lattice geometry. In the simple honeycomb lattice, for instance, unseen and exciting quantum mechanical effects have been predicted.[163,166,450] Scanning tunnelling microscopy and spectroscopy will be an appropriate tool for investigating these materials in detail.

AUTHOR INFORMATION

Corresponding Author

*E-mail: d.vanmaekelbergh@uu.nl.

Notes

The authors declare no competing financial interest.

Biographies

Ingmar Swart obtained a Ph.D. degree from Utrecht University in 2008. After a postdoc at the University of Regensburg, he returned to Utrecht in 2012 to set up a research group focusing on correlating the geometric and electronic structure of (nanostructured) materials.

Peter Liljeroth was born in Lahti (Finland) in 1975; he received a M.Sc. in 1999 and a Ph.D. in 2002 in Physical Chemistry and Electrochemistry from the Helsinki University of Technology (Finland). After postdoctoral stays at Utrecht University and IBM Zurich Research Laboratory, he received a VIDI fellowship in 2007 for work on scanning tunneling microscopy on colloidal nanocrystals at the Debye Institute for Nanomaterials Science in Utrecht University. Since the beginning of 2011, he has been a full professor in physics at Aalto University (Finland). He was awarded an ERC Starting Grant in 2012, and his current research focuses on atomically well-defined graphene nanostructures and molecular self-assembly on graphene using low-temperature scanning probe microscopies.

Daniel Vanmaekelbergh was born in Brugge (Belgium) on August 18, 1958. He currently leads a group at the University of Utrecht (The Netherlands) focussed on colloidal quantum dots and 2-D nanostructured semiconductors with Dirac-type valence and conduction bands, investigated by optical and scanning tunnelling microscopy and spectroscopy.

REFERENCES

(1) Alperson, B.; Rubinstein, I.; Hodes, G.; Porath, D.; Millo, O. Energy Level Tunneling Spectroscopy and Single Electron Charging in Individual CdSe Quantum Dots. *Appl. Phys. Lett.* **1999**, *75*, 1751−1753.

(2) Alperson, B.; Rubinstein, I.; Hodes, G. Identification of Surface States on Individual CdSe Quantum, Dots by Room-Temperature Conductance Spectroscopy. *Phys. Rev. B: Condens. Matter Mater. Phys.* **2001**, *6308*, 081303.

(3) Bakkers, E.; Hens, Z.; Zunger, A.; Franceschetti, A.; Kouwenhoven, L. P.; Gurevich, L.; Vanmaekelbergh, D. Shell-Tunneling Spectroscopy of the Single-Particle Energy Levels of Insulating Quantum Dots. *Nano Lett.* **2001**, *1*, 551−556.

(4) Jdira, L.; Liljeroth, P.; Stoffels, E.; Vanmaekelbergh, D.; Speller, S. Size-Dependent Single-Particle Energy Levels and Interparticle Coulomb Interactions in CdSe Quantum Dots Measured by Scanning Tunneling Spectroscopy. *Phys. Rev. B: Condens. Matter Mater. Phys.* **2006**, *73*, 115305.

(5) Liljeroth, P.; Jdira, L.; Overgaag, K.; Grandidier, B.; Speller, S.; Vanmaekelbergh, D. Can Scanning Tunnelling Spectroscopy Measure the Density of States of Semiconductor Quantum Dots? *Phys. Chem. Chem. Phys.* **2006**, *8*, 3845−3850.

(6) Jdira, L.; Overgaag, K.; Gerritsen, J.; Vanmaekelbergh, D.; Liljeroth, P.; Speller, S. Scanning Tunnelling Spectroscopy on Arrays of CdSe Quantum Dots: Response of Wave Functions to Local Electric Fields. *Nano Lett.* **2008**, *8*, 4014−4019.

(7) Sun, Z.; Swart, I.; Delerue, C.; Vanmaekelbergh, D.; Liljeroth, P. Orbital and Charge-Resolved Polaron States in CdSe Dots and Rods Probed by Scanning Tunneling Spectroscopy. *Phys. Rev. Lett.* **2009**, *102*, 196401.

(8) Katz, D.; Wizansky, T.; Millo, O.; Rothenberg, E.; Mokari, T.; Banin, U. Size Dependent Tunneling and Optical Spectroscopy of CdSe Quantum Rods. *Phys. Rev. Lett.* **2002**, *89*, 086801.

(9) Murray, C. B.; Norris, D. J.; Bawendi, M. G. Synthesis and Characterization of Nearly Monodisperse CdE (E = S, Se, Te) Semiconductor Nanocrystallites. *J. Am. Chem. Soc.* **1993**, *115*, 8706−8715.

(10) Norris, D. J.; Nirmal, M.; Murray, C. B.; Sacra, A.; Bawendi, M. G. Size-Dependent Optical Spectroscopy of II-VI Semiconductor Nanocrystallites (Quantum Dots). *Z. Phys. D: At., Mol. Clusters* **1993**, *26*, 355−357.

(11) Ekimov, A. I.; Efros, A. L.; Onushchenko, A. A. Quantum Size Effect in Semiconductor Microcrystals. *Solid State Commun.* **1985**, *56*, 921−924.

(12) Ekimov, A. I.; Hache, F.; Schanneklein, M. C.; Ricard, D.; Flytzanis, C.; Kudryavtsev, I. A.; Yazeva, T. V.; Rodina, A. V.; Efros, A. L. Absorption and Intensity-Dependent Photoluminescence Measurements on CdSe Quantum Dots - Assignment of the 1st Electronic-Transitions. *J. Opt. Soc. Am. B* **1993**, *10*, 100−107.

(13) Rossetti, R.; Nakahara, S.; Brus, L. E. Quantum Size Effects in the Redox Potentials, Resonance Raman Spectra, and Electronic Spectra of Cadmium Sulfide Crystallites in Aqueous Solution. *J. Chem. Phys.* **1983**, *79*, 1086−1088.

(14) Brus, L. E. Electron-Electron and Electron-Hole Interactions in Small Semiconductor Crystallites: The Size Dependence of the Lowest Excited Electronic State. *J. Chem. Phys.* **1984**, *80*, 4403−4409.

DOI: 10.1021/acs.chemrev.5b00678
Chem. Rev. 2016, 116, 11181−11219

(15) Efros, A. L.; Rodina, A. V. Confined Excitons, Trions and Biexcitons in Semiconductor Microcrystals. *Solid State Commun.* **1989**, *72*, 645−649.
(16) Proot, J. P.; Delerue, C.; Allan, G. Electronic-Structure and Optical-Properties of Silicon Crystallites - Application to Porous Silicon. *Appl. Phys. Lett.* **1992**, *61*, 1948−1950.
(17) Delerue, C.; Lannoo, M.; Allan, G.; Martin, E.; Mihalcescu, I.; Vial, J. C.; Romestain, R.; Muller, F.; Bsiesy, A. Auger and Coulomb Charging Effects in Semiconductor Nanocrystallites. *Phys. Rev. Lett.* **1995**, *75*, 2228−2231.
(18) Wang, L.-W.; Zunger, A. Pseudopotential Calculations of Nanoscale CdSe Quantum Dots. *Phys. Rev. B: Condens. Matter Mater. Phys.* **1996**, *53*, 9579−9582.
(19) Franceschetti, A.; Zunger, A. Direct Pseudopotential Calculation of Exciton Coulomb and Exchange Energies in Semiconductor Quantum Dots. *Phys. Rev. Lett.* **1997**, *78*, 915−918.
(20) Micic, O. I.; Cheong, H. M.; Fu, H.; Zunger, A.; Sprague, J. R.; Mascarenhas, A.; Nozik, A. J. Size-Dependent Spectroscopy of InP Quantum Dots. *J. Phys. Chem. B* **1997**, *101*, 4904−4912.
(21) Donega, C. D.; Liljeroth, P.; Vanmaekelbergh, D. Physicochemical Evaluation of the Hot-Injection Method, a Synthesis Route for Monodisperse Nanocrystals. *Small* **2005**, *1*, 1152−1162.
(22) Talapin, D. V.; Rogach, A. L.; Shevchenko, E. V.; Kornowski, A.; Haase, M.; Weller, H. Dynamic Distribution of Growth Rates within the Ensembles of Colloidal II-VI and III-V Semiconductor Nanocrystals as a Factor Governing Their Photoluminescence Efficiency. *J. Am. Chem. Soc.* **2002**, *124*, 5782−5790.
(23) Chan, E. M.; Mathies, R. A.; Alivisatos, A. P. Size-Controlled Growth of CdSe Nanocrystals in Microfluidic Reactors. *Nano Lett.* **2003**, *3*, 199−201.
(24) Abe, S.; Capek, R. K.; De Geyter, B.; Hens, Z. Reaction Chemistry/Nanocrystal Property Relations in the Hot Injection Synthesis, the Role of the Solute Solubility. *ACS Nano* **2013**, *7*, 943−949.
(25) Hendricks, M. P.; Campos, M. P.; Cleveland, G. T.; Jen-La Plante, I.; Owen, J. S. A Tunable Library of Substituted Thiourea Precursors to Metal Sulfide Nanocrystals. *Science* **2015**, *348*, 1226−1230.
(26) Owen, J. S.; Chan, E. M.; Liu, H. T.; Alivisatos, A. P. Precursor Conversion Kinetics and the Nucleation of Cadmium Selenide Nanocrystals. *J. Am. Chem. Soc.* **2010**, *132*, 18206−18213.
(27) Allen, P. M.; Walker, B. J.; Bawendi, M. G. Mechanistic Insights into the Formation of InP Quantum Dots. *Angew. Chem., Int. Ed.* **2010**, *49*, 760−762.
(28) Owen, J. S.; Park, J.; Trudeau, P. E.; Alivisatos, A. P. Reaction Chemistry and Ligand Exchange at Cadmium-Selenide Nanocrystal Surfaces. *J. Am. Chem. Soc.* **2008**, *130*, 12279−12281.
(29) Liu, H. T.; Owen, J. S.; Alivisatos, A. P. Mechanistic Study of Precursor Evolution in Colloidal Group II-VI Semiconductor Nanocrystal Synthesis. *J. Am. Chem. Soc.* **2007**, *129*, 305−312.
(30) Steckel, J. S.; Yen, B. K. H.; Oertel, D. C.; Bawendi, M. G. On the Mechanism of Lead Chalcogenide Nanocrystal Formation. *J. Am. Chem. Soc.* **2006**, *128*, 13032−13033.
(31) van Embden, J.; Mulvaney, P. Nucleation and Growth of CdSe Nanocrystals in a Binary Ligand System. *Langmuir* **2005**, *21*, 10226−10233.
(32) Bullen, C. R.; Mulvaney, P. Nucleation and Growth Kinetics of CdSe Nanocrystals in Octadecene. *Nano Lett.* **2004**, *4*, 2303−2307.
(33) Yu, W. W.; Peng, X. G. Formation of High-Quality CdS and Other II-VI Semiconductor Nanocrystals in Noncoordinating Solvents: Tunable Reactivity of Monomers. *Angew. Chem., Int. Ed.* **2002**, *41*, 2368−2371.
(34) Yarema, M.; Kovalenko, M. V.; Hesser, G.; Talapin, D. V.; Heiss, W. Highly Monodisperse Bismuth Nanoparticles and Their Three-Dimensional Superlattices. *J. Am. Chem. Soc.* **2010**, *132*, 15158−15159.
(35) Yarema, M.; Caputo, R.; Kovalenko, M. V. Precision Synthesis of Colloidal Inorganic Nanocrystals Using Metal and Metalloid Amides. *Nanoscale* **2013**, *5*, 8398−8410.
(36) Talapin, D. V.; Lee, J. S.; Kovalenko, M. V.; Shevchenko, E. V. Prospects of Colloidal Nanocrystals for Electronic and Optoelectronic Applications. *Chem. Rev.* **2010**, *110*, 389−458.
(37) Jiang, Y.; Wu, Y.; Yuan, S. W.; Xie, B.; Zhang, S. Y.; Qian, Y. T. Preparation and Characterization of CuInS2 Nanorods and Nanotubes from an Elemental Solvothermal Reaction. *J. Mater. Res.* **2001**, *16*, 2805−2809.
(38) Kan, S. H.; Aharoni, A.; Mokari, T.; Banin, U. Shape Control of III-V Semiconductor Nanocrystals: Synthesis and Properties of InAs Quantum Rods. *Faraday Discuss.* **2004**, *125*, 23−38.
(39) Steiner, D.; Katz, D.; Millo, O.; Aharoni, A.; Kan, S.; Mokari, T.; Banin, U. Zero-Dimensional and Quasi One-Dimensional Effects in Semiconductor Nanorods. *Nano Lett.* **2004**, *4*, 1073−1077.
(40) Sitt, A.; Sala, F. D.; Menagen, G.; Banin, U. Multiexciton Engineering in Seeded Core/Shell Nanorods: Transfer from Type-I to Quasi-Type-II Regimes. *Nano Lett.* **2009**, *9*, 3470−3476.
(41) Manna, L.; Scher, E. C.; Alivisatos, A. P. Synthesis of Soluble and Processable Rod-, Arrow-, Teardrop-, and Tetrapod-Shaped CdSe Nanocrystals. *J. Am. Chem. Soc.* **2000**, *122*, 12700−12706.
(42) Hu, J.; Li, L.-s.; Yang, W.; Manna, L.; Wang, L.-w.; Alivisatos, A. P. Linearly Polarized Emission from Colloidal Semiconductor Quantum Rods. *Science* **2001**, *292*, 2060−2063.
(43) Pacholski, C.; Kornowski, A.; Weller, H. Self-Assembly of ZnO: From Nanodots to Nanorods. *Angew. Chem., Int. Ed.* **2002**, *41*, 1188−1191.
(44) Kan, S.; Mokari, T.; Rothenberg, E.; Banin, U. Synthesis and Size-Dependent Properties of Zinc-Blende Semiconductor Quantum Rods. *Nat. Mater.* **2003**, *2*, 155−158.
(45) Li, L. S.; Alivisatos, A. P. Semiconductor Nanorod Liquid Crystals and Their Assembly on a Substrate. *Adv. Mater.* **2003**, *15*, 408−411.
(46) Talapin, D. V.; Shevchenko, E. V.; Murray, C. B.; Kornowski, A.; Forster, S.; Weller, H. CdSe and CdSe/CdS Nanorod Solids. *J. Am. Chem. Soc.* **2004**, *126*, 12984−12988.
(47) Yin, M.; Gu, Y.; Kuskovsky, I. L.; Andelman, T.; Zhu, Y.; Neumark, G. F.; O'Brien, S. Zinc Oxide Quantum Rods. *J. Am. Chem. Soc.* **2004**, *126*, 6206−6207.
(48) Carbone, L.; Nobile, C.; De Giorgi, M.; Sala, F. D.; Morello, G.; Pompa, P.; Hytch, M.; Snoeck, E.; Fiore, A.; Franchini, I. R.; et al. Synthesis and Micrometer-Scale Assembly of Colloidal CdSe/CdS Nanorods Prepared by a Seeded Growth Approach. *Nano Lett.* **2007**, *7*, 2942−2950.
(49) Talapin, D. V.; Nelson, J. H.; Shevchenko, E. V.; Aloni, S.; Sadtler, B.; Alivisatos, A. P. Seeded Growth of Highly Luminescent CdSe/CdS Nanoheterostructures with Rod and Tetrapod Morphologies. *Nano Lett.* **2007**, *7*, 2951−2959.
(50) Lutich, A. A.; Mauser, C.; Da Como, E.; Huang, J.; Vaneski, A.; Talapin, D. V.; Rogach, A. L.; Feldmann, J. Multiexcitonic Dual Emission in CdSe/CdS Tetrapods and Nanorods. *Nano Lett.* **2010**, *10*, 4646−4650.
(51) Khan, A. H.; Ji, Q.; Ariga, K.; Thupakula, U.; Acharya, S. Size Controlled Ultranarrow PbS Nanorods: Spectroscopy and Robust Stability. *J. Mater. Chem.* **2011**, *21*, 5671−5676.
(52) Pietra, F.; Rabouw, F. T.; Evers, W. H.; Byelov, D. V.; Petukhov, A. V.; de Mello Donega, C.; Vanmaekelbergh, D. Semiconductor Nanorod Self-Assembly at the Liquid/Air Interface Studied by in Situ Gisaxs and Ex Situ Tem. *Nano Lett.* **2012**, *12*, 5515−5523.
(53) Ithurria, S.; Tessier, M. D.; Mahler, B.; Lobo, R. P. S. M.; Dubertret, B.; Efros, A. L. Colloidal Nanoplatelets with Two-Dimensional Electronic Structure. *Nat. Mater.* **2011**, *10*, 936−941.
(54) Mahler, B.; Nadal, B.; Bouet, C.; Patriarche, G.; Dubertret, B. Core/Shell Colloidal Semiconductor Nanoplatelets. *J. Am. Chem. Soc.* **2012**, *134*, 18591−18598.
(55) Bouet, C.; Mahler, B.; Nadal, B.; Abecassis, B.; Tessier, M. D.; Ithurria, S.; Xu, X.; Dubertret, B. Two-Dimensional Growth of CdSe Nanocrystals, from Nanoplatelets to Nanosheets. *Chem. Mater.* **2013**, *25*, 639−645.

DOI: 10.1021/acs.chemrev.5b00678
Chem. Rev. 2016, 116, 11181−11219

(56) Bouet, C.; Tessier, M. D.; Ithurria, S.; Mahler, B.; Nadal, B.; Dubertret, B. Flat Colloidal Semiconductor Nanoplatelets. *Chem. Mater.* **2013**, *25*, 1262−1271.
(57) Bals, S.; Casavola, M.; van Huis, M. A.; Van Aert, S.; Batenburg, K. J.; Van Tendeloo, G.; Vanmaekelbergh, D. Three-Dimensional Atomic Imaging of Colloidal Core-Shell Nanocrystals. *Nano Lett.* **2011**, *11*, 3420−3424.
(58) Evers, W. H.; Goris, B.; Bals, S.; Casavola, M.; de Graaf, J.; van Roij, R.; Dijkstra, M.; Vanmaekelbergh, D. Low-Dimensional Semiconductor Superlattices Formed by Geometric Control over Nanocrystal Attachment. *Nano Lett.* **2013**, *13*, 2317−2323.
(59) Hutter, E. M.; Bladt, E.; Goris, B.; Pietra, F.; van der Bok, J. C.; Boneschanscher, M. P.; de Mello Donega, C.; Bals, S.; Vanmaekelbergh, D. Conformal and Atomic Characterization of Ultrathin CdSe Platelets with a Helical Shape. *Nano Lett.* **2014**, *14*, 6257−6262.
(60) van Huis, M. A.; Young, N. P.; Pandraud, G.; Creemer, J. F.; Vanmaekelbergh, D.; Kirkland, A. I.; Zandbergen, H. W. Atomic Imaging of Phase Transitions and Morphology Transformations in Nanocrystals. *Adv. Mater.* **2009**, *21*, 4992−4995.
(61) Fang, C.; van Huis, M. A.; Vanmaekelbergh, D.; Zandbergen, H. W. Energetics of Polar and Nonpolar Facets of PbSe Nanocrystals from Theory and Experiment. *ACS Nano* **2010**, *4*, 211−218.
(62) Schapotschnikow, P.; van Huis, M. A.; Zandbergen, H. W.; Vanmaekelbergh, D.; Vlugt, T. J. H. Morphological Transformations and Fusion of PbSe Nanocrystals Studied Using Atomistic Simulations. *Nano Lett.* **2010**, *10*, 3966−3971.
(63) Weller, H. Quantized Semiconductor Particles: A Novel State of Matter for Materials Science. *Adv. Mater.* **1993**, *5*, 88−95.
(64) Talapin, D. V.; Rogach, A. L.; Kornowski, A.; Haase, M.; Weller, H. Highly Luminescent Monodisperse CdSe and CdSe/ZnS Nanocrystals Synthesized in a Hexadecylamine-Trioctylphosphine Oxide-Trioctylphospine Mixture. *Nano Lett.* **2001**, *1*, 207−211.
(65) Peng, X.; Manna, L.; Yang, W.; Wickham, J.; Scher, E.; Kadavanich, A.; Alivisatos, A. P. Shape Control of CdSe Nanocrystals. *Nature* **2000**, *404*, 59−61.
(66) Jacobs, K.; Wickham, J.; Alivisatos, A. P. Threshold Size for Ambient Metastability of Rocksalt CdSe Nanocrystals. *J. Phys. Chem. B* **2002**, *106*, 3759−3762.
(67) Scher, E. C.; Manna, L.; Alivisatos, A. P. Shape Control and Applications of Nanocrystals. *Philos. Trans. R. Soc., A* **2003**, *361*, 241−255.
(68) Milliron, D. J.; Hughes, S. M.; Cui, Y.; Manna, L.; Li, J. B.; Wang, L. W.; Alivisatos, A. P. Colloidal Nanocrystal Heterostructures with Linear and Branched Topology. *Nature* **2004**, *430*, 190−195.
(69) Son, D. H.; Hughes, S. M.; Yin, Y.; Alivisatos, A. P. Cation Exchange Reactions in Ionic Nanocrystals. *Science* **2004**, *306*, 1009−1012.
(70) Hassinen, A.; Gomes, R.; De Nolf, K.; Zhao, Q.; Vantomme, A.; Martins, J. C.; Hens, Z. Surface Chemistry of CdTe Quantum Dots Synthesized in Mixtures of Phosphonic Acids and Amines: Formation of a Mixed Ligand Shell. *J. Phys. Chem. C* **2013**, *117*, 13936−13943.
(71) Hassinen, A.; Moreels, I.; De Nolf, K.; Smet, P. F.; Martins, J. C.; Hens, Z. Short-Chain Alcohols Strip X-Type Ligands and Quench the Luminescence of PbSe and CdSe Quantum Dots, Acetonitrile Does Not. *J. Am. Chem. Soc.* **2012**, *134*, 20705−20712.
(72) Hassinen, A.; Moreels, I.; de Mello Donega, C.; Martins, J. C.; Hens, Z. Nuclear Magnetic Resonance Spectroscopy Demonstrating Dynamic Stabilization of CdSe Quantum Dots by Alkylamines. *J. Phys. Chem. Lett.* **2010**, *1*, 2577−2581.
(73) Moreels, I.; Fritzinger, B.; Martins, J. C.; Hens, Z. Surface Chemistry of Colloidal PbSe Nanocrystals. *J. Am. Chem. Soc.* **2008**, *130*, 15081−15086.
(74) Hens, Z.; Moreels, I.; Martins, J. C. In Situ H-1 Nmr Study on the Trioctylphosphine Oxide Capping of Colloidal InP Nanocrystals. *ChemPhysChem* **2005**, *6*, 2578−2584.
(75) Anderson, N. C.; Owen, J. S. Soluble, Chloride-Terminated CdSe Nanocrystals: Ligand Exchange Monitored by H-1 and P-31 NMR Spectroscopy. *Chem. Mater.* **2013**, *25*, 69−76.
(76) Anderson, N. C.; Hendricks, M. P.; Choi, J. J.; Owen, J. S. Ligand Exchange and the Stoichiometry of Metal Chalcogenide Nanocrystals: Spectroscopic Observation of Facile Metal-Carboxylate Displacement and Binding. *J. Am. Chem. Soc.* **2013**, *135*, 18536−18548.
(77) Kreider-Mueller, A. R.; Parkin, G.; Owen, J. S. Modeling Ligand Exchange at Carboxylate Terminated CdSe Nanocrystal Surfaces by Employing Tris(2-Mercapto-1-T-Butylimidazolyl)Hydroborato Cadmium Complexes. *Abstr. Pap., Am. Chem. Soc.* **2012**, *244*.
(78) Yin, Y.; Alivisatos, A. P. Colloidal Nanocrystal Synthesis and the Organic-Inorganic Interface. *Nature* **2005**, *437*, 664−670.
(79) Hines, M. A.; Guyot-Sionnest, P. Synthesis and Characterization of Strongly Luminescing ZnS-Capped CdSe Nanocrystals. *J. Phys. Chem.* **1996**, *100*, 468−471.
(80) Dabbousi, B. O.; RodriguezViejo, J.; Mikulec, F. V.; Heine, J. R.; Mattoussi, H.; Ober, R.; Jensen, K. F.; Bawendi, M. G. (CdSe)ZnS Core-Shell Quantum Dots: Synthesis and Characterization of a Size Series of Highly Luminescent Nanocrystallites. *J. Phys. Chem. B* **1997**, *101*, 9463−9475.
(81) Peng, X. G.; Schlamp, M. C.; Kadavanich, A. V.; Alivisatos, A. P. Epitaxial Growth of Highly Luminescent CdSe/CdS Core/Shell Nanocrystals with Photostability and Electronic Accessibility. *J. Am. Chem. Soc.* **1997**, *119*, 7019−7029.
(82) Banin, U.; Bruchez, M.; Alivisatos, A. P.; Ha, T.; Weiss, S.; Chemla, D. S. Evidence for a Thermal Contribution to Emission Intermittency in Single CdSe/CdS Core/Shell Nanocrystals. *J. Chem. Phys.* **1999**, *110*, 1195−1201.
(83) Harrison, M. T.; Kershaw, S. V.; Rogach, A. L.; Kornowski, A.; Eychmuller, A.; Weller, H. Wet Chemical Synthesis of Highly Luminescent HgTe/CdS Core/Shell Nanocrystals. *Adv. Mater.* **2000**, *12*, 123−125.
(84) Reiss, P.; Bleuse, J.; Pron, A. Highly Luminescent CdSe/ZnSe Core/Shell Nanocrystals of Low Size Dispersion. *Nano Lett.* **2002**, *2*, 781−784.
(85) Li, J. J.; Wang, Y. A.; Guo, W.; Keay, J. C.; Mishima, T. D.; Johnson, M. B.; Peng, X. Large-Scale Synthesis of Nearly Monodisperse CdSe/CdS Core/Shell Nanocrystals Using Air-Stable Reagents Via Successive Ion Layer Adsorption and Reaction. *J. Am. Chem. Soc.* **2003**, *125*, 12567−12575.
(86) Kim, S.; Fisher, B.; Eisler, H.-J.; Bawendi, M. Type-II Quantum Dots: CdTe/CdSe(Core/Shell) and CdSe/ZnTe(Core/Shell) Heterostructures. *J. Am. Chem. Soc.* **2003**, *125*, 11466−11467.
(87) Balet, L. P.; Ivanov, S. A.; Piryatinski, A.; Achermann, M.; Klimov, V. I. Inverted Core/Shell Nanocrystals Continuously Tunable between Type-I and Type-II Localization Regimes. *Nano Lett.* **2004**, *4*, 1485−1488.
(88) Bao, H. B.; Gong, Y. J.; Li, Z.; Gao, M. Y. Enhancement Effect of Illumination on the Photoluminescence of Water-Soluble CdTe Nanocrystals: Toward Highly Fluorescent CdTe/CdS Core-Shell Structure. *Chem. Mater.* **2004**, *16*, 3853−3859.
(89) Chen, C. Y.; Cheng, C. T.; Yu, J. K.; Pu, S. C.; Cheng, Y. M.; Chou, P. T.; Chou, Y. H.; Chiu, H. T. Spectroscopy and Femtosecond Dynamics of Type-II CdSe/ZnTe Core-Shell Semiconductor Synthesized Via the Cdo Precursor. *J. Phys. Chem. B* **2004**, *108*, 10687−10691.
(90) Ivanov, S. A.; Nanda, J.; Piryatinski, A.; Achermann, M.; Balet, L. P.; Bezel, I. V.; Anikeeva, P. O.; Tretiak, S.; Klimov, V. I. Light Amplification Using Inverted Core/Shell Nanocrystals: Towards Lasing in the Single-Exciton Regime. *J. Phys. Chem. B* **2004**, *108*, 10625−10630.
(91) Li, J. B.; Wang, L. W. First Principle Study of Core/Shell Structure Quantum Dots. *Appl. Phys. Lett.* **2004**, *84*, 3648−3650.
(92) Talapin, D. V.; Mekis, I.; Gotzinger, S.; Kornowski, A.; Benson, O.; Weller, H. CdSe/CdS/ZnS and CdSe/ZnSe/ZnS Core-Shell-Shell Nanocrystals. *J. Phys. Chem. B* **2004**, *108*, 18826−18831.
(93) Brumer, M.; Kigel, A.; Amirav, L.; Sashchiuk, A.; Solomesch, O.; Tessler, N.; Lifshitz, E. PbSe/PbS and PbSe/PbSe$_x$S$_{1-X}$ Core/Shell Nanoparticles. *Adv. Funct. Mater.* **2005**, *15*, 1111−1116.

DOI: 10.1021/acs.chemrev.5b00678
Chem. Rev. 2016, 116, 11181−11219

(94) Chen, C.-Y.; Cheng, C.-T.; Lai, C.-W.; Hu, Y.-H.; Chou, P.-T.; Chou, Y.-H.; Chiu, H.-T. Type-II CdSe/CdTe/ZnTe(Core-Shell-Shell) Quantum Dots with Cascade Band Edges: The Separation of Electron (at CdSe) and Hole (at ZnTe) by the CdTe Layer. *Small* **2005**, *1*, 1215.
(95) Cheng, C. T.; Chen, C. Y.; Lai, C. W.; Liu, W. H.; Pu, S. C.; Chou, P. T.; Chou, Y. H.; Chiu, H. T. Syntheses and Photophysical Properties of Type-II CdSe/ZnTe/ZnS (Core/Shell/Shell) Quantum Dots. *J. Mater. Chem.* **2005**, *15*, 3409−3414.
(96) Fradkin, L.; Langof, L.; Lifshitz, E.; Gaponik, N.; Rogach, A.; Eychmuller, A.; Weller, H.; Micic, O. I.; Nozik, A. J. A Direct Measurement of g-Factors in II-VI and III-V Core-Shell Nanocrystals. *Phys. E* **2005**, *26*, 9−13.
(97) Xie, R.; Kolb, U.; Li, J.; Basche, T.; Mews, A. Synthesis and Characterization of Highly Luminescent CdSe−Core CdS/Zn0.5cd0.5s/ZnS Multishell Nanocrystals. *J. Am. Chem. Soc.* **2005**, *127*, 7480−7488.
(98) Chou, P. T.; Chen, C. Y.; Cheng, C. T.; Pu, S. C.; Wu, K. C.; Cheng, Y. M.; Lai, C. W.; Chou, Y. H.; Chiu, H. T. Spectroscopy and Femtosecond Dynamics of Type-II CdTe/CdSe Core-Shell Quantum Dots. *ChemPhysChem* **2006**, *7*, 222−228.
(99) Nanda, J.; Ivanov, S. A.; Htoon, H.; Bezel, I.; Piryatinski, A.; Tretiak, S.; Klimov, V. I. Absorption Cross Sections and Auger Recombination Lifetimes in Inverted Core-Shell Nanocrystals: Implications for Lasing Performance. *J. Appl. Phys.* **2006**, *99*, 034309.
(100) Pandey, A.; Guyot-Sionnest, P. Intraband Spectroscopy and Band Offsets of Colloidal II−VI Core/Shell Structures. *J. Chem. Phys.* **2007**, *127*, 104710.
(101) Piryatinski, A.; Ivanov, S. A.; Tretiak, S.; Klimov, V. I. Effect of Quantum and Dielectric Confinement on the Exciton-Exciton Interaction Energy in Type II Core/Shell Semiconductor Nanocrystals. *Nano Lett.* **2007**, *7*, 108−115.
(102) Stouwdam, J. W.; Shan, J.; van Veggel, F. C. J. M.; Pattantyus-Abraham, A. G.; Young, J. F.; Raudsepp, M. Photostability of Colloidal PbSe and PbSe/PbS Core/Shell Nanocrystals in Solution and in the Solid State. *J. Phys. Chem. C* **2007**, *111*, 1086−1092.
(103) Talapin, D. V.; Yu, H.; Shevchenko, E. V.; Lobo, A.; Murray, C. B. Synthesis of Colloidal PbSe/PbS Core-Shell Nanowires and PbS/Au Nanowire-Nanocrystal Heterostructures. *J. Phys. Chem. C* **2007**, *111*, 14049−14054.
(104) Lee, J.-S.; Shevchenko, E. V.; Talapin, D. V. Au-PbS Core-Shell Nanocrystals: Plasmonic Absorption Enhancement and Electrical Doping Via Intra-Particle Charge Transfer. *J. Am. Chem. Soc.* **2008**, *130*, 9673−9675.
(105) Lupo, M. G.; Della Sala, F.; Carbone, L.; Zavelani-Rossi, M.; Fiore, A.; Lueer, L.; Polli, D.; Cingolani, R.; Manna, L.; Lanzani, G. Ultrafast Electron-Hole Dynamics in Core/Shell CdSe/CdS Dot/Rod Nanocrystals. *Nano Lett.* **2008**, *8*, 4582−4587.
(106) Bang, J.; Park, J.; Lee, J. H.; Won, N.; Nam, J.; Lim, J.; Chang, B. Y.; Lee, H. J.; Chon, B.; Shin, J.; et al. ZnTe/ZnSe (Core/Shell) Type-II Quantum Dots: Their Optical and Photovoltaic Properties. *Chem. Mater.* **2010**, *22*, 233−240.
(107) Gomez, D. E.; van Embden, J.; Mulvaney, P.; Fernee, M. J.; Rubinsztein-Dunlop, H. Exciton-Trion Transitions in Single CdSe-CdS Core-Shell Nanocrystals. *ACS Nano* **2009**, *3*, 2281−2287.
(108) Ithurria, S.; Guyot-Sionnest, P.; Mahler, B.; Dubertret, B. Radial Pressure Measurement in Core/Shell Nanocrystals. *Proc. SPIE* **2009**, *7189*, 718908.
(109) Lambert, K.; De Geyter, B.; Moreels, I.; Hens, Z. PbTelCdTe Corelshell Particles by Cation Exchange, a HR-Tem Study. *Chem. Mater.* **2009**, *21*, 778−780.
(110) Li, L.; Daou, T. J.; Texier, I.; Kim Chi, T. T.; Liem, N. Q.; Reiss, P. Highly Luminescent $CuInS_2$/ZnS Core/Shell Nanocrystals: Cadmium-Free Quantum Dots for in Vivo Imaging. *Chem. Mater.* **2009**, *21*, 2422−2429.
(111) Nizamoglu, S.; Demir, H. V. In *2009 IEEE LEOS Annual Meeting Conference Proceedings, Vol. 1 and 2*; IEEE Lasers and Electro-Optics Society (LEOS 2009) Annual Meeting, Belek-Antalya, Turkey, October 4−8, 2009; pp 280−281.
(112) Pons, T.; Lequeux, N.; Mahler, B.; Sasnouski, S.; Fragola, A.; Dubertret, B. Synthesis of near-Infrared-Emitting, Water-Soluble CdTeSe/CdZnS Core/Shell Quantum Dots. *Chem. Mater.* **2009**, *21*, 1418−1424.
(113) van Embden, J.; Jasieniak, J.; Mulvaney, P. Mapping the Optical Properties of CdSe/CdS Heterostructure Nanocrystals: The Effects of Core Size and Shell Thickness. *J. Am. Chem. Soc.* **2009**, *131*, 14299−14309.
(114) Chao, H. Y.; Cheng, J. H.; Lu, J. Y.; Chang, Y. H.; Cheng, C. L.; Chen, Y. F. Growth and Characterization of Type-II ZnO/ZnTe Core-Shell Nanowire Arrays for Solar Cell Applications. *Superlattices Microstruct.* **2010**, *47*, 160−164.
(115) De Geyter, B.; Hens, Z. The Absorption Coefficient of PbSe/CdSe Core/Shell Colloidal Quantum Dots. *Appl. Phys. Lett.* **2010**, *97*, 161908.
(116) De Geyter, B.; Justo, Y.; Moreels, I.; Lambert, K.; Smet, P. F.; Van Thourhout, D.; Houtepen, A. J.; Grodzinska, D.; de Mello Donega, C.; Meijerink, A.; et al. The Different Nature of Band Edge Absorption and Emission in Colloidal PbSe/CdSe Core/Shell Quantum Dots. *ACS Nano* **2011**, *5*, 58−66.
(117) Htoon, H.; Malko, A. V.; Bussian, D.; Vela, J.; Chen, Y.; Hollingsworth, J. A.; Klimov, V. I. Highly Emissive Multiexcitons in Steady-State Photoluminescence of Individual "Giant" CdSe/CdS Core/Shell Nanocrystals. *Nano Lett.* **2010**, *10*, 2401−2407.
(118) Swart, I.; Sun, Z.; Vanmaekelbergh, D.; Liljeroth, P. Hole-Induced Electron Transport through Core-Shell Quantum Dots: A Direct Measurement of the Electron-Hole Interaction. *Nano Lett.* **2010**, *10*, 1931−1935.
(119) Zavelani-Rossi, M.; Lupo, M. G.; Krahne, R.; Manna, L.; Lanzani, G. Lasing in Self-Assembled Microcavities of CdSe/CdS Core/Shell Colloidal Quantum Rods. *Nanoscale* **2010**, *2*, 931−935.
(120) Algra, R. E.; Hocevar, M.; Verheijen, M. A.; Zardo, I.; Immink, G. G. W.; van Enckevort, W. J. P.; Abstreiter, G.; Kouwenhoven, L. P.; Vlieg, E.; Bakkers, E. P. A. M. Crystal Structure Transfer in Core/Shell Nanowires. *Nano Lett.* **2011**, *11*, 1690−1694.
(121) Grodzińska, D.; Evers, W. H.; Dorland, R.; van Rijssel, J.; van Huis, M. A.; Meijerink, A.; de Mello Donegá, C.; Vanmaekelbergh, D. Two-Fold Emission from the S-Shell of PbSe/CdSe Core/Shell Quantum Dots. *Small* **2011**, *7*, 3493−3501.
(122) Casavola, M.; van Huis, M. A.; Bals, S.; Lambert, K.; Hens, Z.; Vanmaekelbergh, D. Anisotropic Cation Exchange in PbSe/CdSe Core/Shell Nanocrystals of Different Geometry. *Chem. Mater.* **2012**, *24*, 294−302.
(123) Li, H.; Brescia, R.; Krahne, R.; Bertoni, G.; Alcocer, M. J. P.; D'Andrea, C.; Scotognella, F.; Tassone, F.; Zanella, M.; De Giorgi, M.; et al. Blue-UV-Emitting ZnSe(Dot)/ZnS(Rod) Core/Shell Nanocrystals Prepared from CdSe/CdS Nanocrystals by Sequential Cation Exchange. *ACS Nano* **2012**, *6*, 1637−1647.
(124) Perera, D.; Lorek, R.; Khnayzer, R. S.; Moroz, P.; O'Connor, T.; Khon, D.; Diederich, G.; Kinder, E.; Lambright, S.; Castellano, F. N.; et al. Photocatalytic Activity of Core/Shell Semiconductor Nanocrystals Featuring Spatial Separation of Charges. *J. Phys. Chem. C* **2012**, *116*, 22786−22793.
(125) Zhao, J.; Chen, O.; Strasfeld, D. B.; Bawendi, M. G. Biexciton Quantum Yield Heterogeneities in Single CdSe (CdS) Core (Shell) Nanocrystals and Its Correlation to Exciton Blinking. *Nano Lett.* **2012**, *12*, 4477−4483.
(126) Zolotavin, P.; Guyot-Sionnest, P. Superconductivity in Films of Pb/PbSe Core/Shell Nanocrystals. *ACS Nano* **2012**, *6*, 8094−8104.
(127) Allione, M.; Ballester, A.; Li, H.; Comin, A.; Movilla, J. L.; Climente, J. I.; Manna, L.; Moreels, I. Two-Photon-Induced Blue Shift of Core and Shell Optical Transitions in Colloidal CdSe/CdS Quasi-Type II Quantum Rods. *ACS Nano* **2013**, *7*, 2443−2452.
(128) Pisanello, F.; Lemenager, G.; Martiradonna, L.; Carbone, L.; Bramati, A.; De Vittorio, M. Effect of Shell Size on Single Photon Emission Performances of Core/Shell Dot-in-Rods Colloidal Nanocrystals. 15th International Conference on Transparent Optical Networks (ICTON 2013), Cartagena, Spain, June 23−27, 2013.

DOI: 10.1021/acs.chemrev.5b00678
Chem. Rev. 2016, 116, 11181−11219

(129) Tessier, M. D.; Mahler, B.; Nadal, B.; Heuclin, H.; Pedetti, S.; Dubertret, B. Spectroscopy of Colloidal Semiconductor Core/Shell Nanoplatelets with High Quantum Yield. *Nano Lett.* **2013**, *13*, 3321−3328.
(130) Coropceanu, I.; Bawendi, M. G. Core/Shell Quantum Dot Based Luminescent Solar Concentrators with Reduced Reabsorption and Enhanced Efficiency. *Nano Lett.* **2014**, *14*, 4097−4101.
(131) Murray, C. B.; Kagan, C. R.; Bawendi, M. G. Self-Organization of CdSe Nanocrystallites into Three-Dimensional Quantum Dot Superlattices. *Science* **1995**, *270*, 1335−1338.
(132) Redl, F. X.; Cho, K. S.; Murray, C. B.; O'Brien, S. Three-Dimensional Binary Superlattices of Magnetic Nanocrystals and Semiconductor Quantum Dots. *Nature* **2003**, *423*, 968−971.
(133) Vanmaekelbergh, D. Self-Assembly of Colloidal Nanocrystals as Route to Novel Classes of Nanostructured Materials. *Nano Today* **2011**, *6*, 419−437.
(134) Brust, M.; Bethell, D.; Kiely, C. J.; Schiffrin, D. J. Self-Assembled Gold Nanoparticle Thin Films with Nonmetallic Optical and Electronic Properties. *Langmuir* **1998**, *14*, 5425−5429.
(135) Kiely, C. J.; Fink, J.; Brust, M.; Bethell, D.; Schiffrin, D. J. Spontaneous Ordering of Bimodal Ensembles of Nanoscopic Gold Clusters. *Nature* **1998**, *396*, 444−446.
(136) Rogach, A. L. Binary Superlattices of Nanoparticles: Self-Assembly Leads to "Metamaterials". *Angew. Chem., Int. Ed.* **2004**, *43*, 148−149.
(137) Evers, W. H.; Nijs, B. D.; Filion, L.; Castillo, S.; Dijkstra, M.; Vanmaekelbergh, D. Entropy-Driven Formation of Binary Semiconductor-Nanocrystal Superlattices. *Nano Lett.* **2010**, *10*, 4235−4241.
(138) Chen, Z.; O'Brien, S. Structure Direction of II-VI Semiconductor Quantum Dot Binary Nanoparticle Superlattices by Tuning Radius Ratio. *ACS Nano* **2008**, *2*, 1219−1229.
(139) Bodnarchuk, M. I.; Kovalenko, M. V.; Heiss, W.; Talapin, D. V. Energetic and Entropic Contributions to Self-Assembly of Binary Nanocrystal Superlattices: Temperature as the Structure-Directing Factor. *J. Am. Chem. Soc.* **2010**, *132*, 11967−11977.
(140) Bartlett, P.; Ottewill, R. H.; Pusey, P. N. Superlattice Formation in Binary-Mixtures of Hard-Sphere Colloids. *Phys. Rev. Lett.* **1992**, *68*, 3801−3804.
(141) Eldridge, M. D.; Madden, P. A.; Frenkel, D. Entropy-Driven Formation of a Superlattice in a Hard-Sphere Binary Mixture. *Nature* **1993**, *365*, 35−37.
(142) Dijkstra, M.; van Roij, R.; Evans, R. Phase Diagram of Highly Asymmetric Binary Hard-Sphere Mixtures. *Phys. Rev. E: Stat. Phys., Plasmas, Fluids, Relat. Interdiscip. Top.* **1999**, *59*, 5744−5771.
(143) Fang, C. M.; van Huis, M. A.; Vanmaekelbergh, D.; Zandbergen, H. W. Energetics of Polar and Nonpolar Facets of PbSe Nanocrystals from Theory and Experiment. *ACS Nano* **2010**, *4*, 211−218.
(144) van Huis, M. A.; Kunneman, L. T.; Overgaag, K.; Xu, Q.; Pandraud, G.; Zandbergen, H. W.; Vanmaekelbergh, D. Low-Temperature Nanocrystal Unification through Rotations and Relaxations Probed by in Situ Transmission Electron Microscopy. *Nano Lett.* **2008**, *8*, 3959−3963.
(145) Cho, K. S.; Talapin, D. V.; Gaschler, W.; Murray, C. B. Designing PbSe Nanowires and Nanorings through Oriented Attachment of Nanoparticles. *J. Am. Chem. Soc.* **2005**, *127*, 7140−7147.
(146) Koh, W. K.; Bartnik, A. C.; Wise, F. W.; Murray, C. B. Synthesis of Monodisperse PbSe Nanorods: A Case for Oriented Attachment. *J. Am. Chem. Soc.* **2010**, *132*, 3909−3913.
(147) Schliehe, C.; Juarez, B. H.; Pelletier, M.; Jander, S.; Greshnykh, D.; Nagel, M.; Meyer, A.; Foerster, S.; Kornowski, A.; Klinke, C.; et al. Ultrathin PbS Sheets by Two-Dimensional Oriented Attachment. *Science* **2010**, *329*, 550−553.
(148) Evers, W. H.; Goris, B.; Bals, S.; Casavola, M.; de Graaf, J.; van Roij, R.; Dijkstra, M.; Vanmaekelbergh, D. Low-Dimensional Semiconductor Superlattices Formed by Geometric Control over Nanocrystal Attachment. *Nano Lett.* **2013**, *13*, 2317−2323.
(149) Sandeep, C. S. S.; Azpiroz, J. M.; Evers, W. H.; Boehme, S.-C.; Moreels, I.; Kinge, S.; Siebbeles, L. D. A.; Infante, I.; Houtepen, A. J. Epitaxially Connected PbSe Quantum-Dot Films: Controlled Neck Formation and Optoelectronic Properties. *ACS Nano* **2014**, *8*, 11499−11511.
(150) Boneschanscher, M. P.; Evers, W. H.; Geuchies, J. J.; Altantzis, T.; Goris, B.; Rabouw, F. T.; van Rossum, S. A. P.; van der Zant, H. S. J.; Siebbeles, L. D. A.; Van Tendeloo, G.; et al. Long-Range Orientation and Atomic Attachment of Nanocrystals in 2d Honeycomb Superlattices. *Science* **2014**, *344*, 1377−1380.
(151) Turk, M. E.; Choi, J.-H.; Oh, S. J.; Fafarman, A. T.; Diroll, B. T.; Murray, C. B.; Kagan, C. R.; Kikkawa, J. M. Gate-Induced Carrier De Localization in Quantum Dot Field Effect Transistors. *Nano Lett.* **2014**, *14*, 5948−5952.
(152) Oh, S. J.; Berry, N. E.; Choi, J. H.; Gaulding, E. A.; Paik, T.; Hong, S. H.; Murray, C. B.; Kagan, C. R. Stoichiometric Control of Lead Chalcogenide Nanocrystal Solids to Enhance Their Electronic and Optoelectronic Device Performance. *ACS Nano* **2013**, *7*, 2413−2421.
(153) Choi, J. H.; Fafarman, A. T.; Oh, S. J.; Ko, D. K.; Kim, D. K.; Diroll, B. T.; Muramoto, S.; Gillen, J. G.; Murray, C. B.; Kagan, C. R. Bandlike Transport in Strongly Coupled and Doped Quantum Dot Solids: A Route to High-Performance Thin-Film Electronics. *Nano Lett.* **2012**, *12*, 2631−2638.
(154) Ko, D. K.; Urban, J. J.; Murray, C. B. Carrier Distribution and Dynamics of Nanocrystal Solids Doped with Artificial Atoms. *Nano Lett.* **2010**, *10*, 1842−1847.
(155) Urban, J. J.; Talapin, D. V.; Shevchenko, E. V.; Kagan, C. R.; Murray, C. B. Synergism in Binary Nanocrystal Superlattices Leads to Enhanced P-Type Conductivity in Self-Assembled PbTe/Ag_2te Thin Films. *Nat. Mater.* **2007**, *6*, 115−121.
(156) Zhang, H.; Jang, J.; Liu, W.; Talapin, D. V. Colloidal Nanocrystals with Inorganic Halide, Pseudohalide, and Halometallate Ligands. *ACS Nano* **2014**, *8*, 7359−7369.
(157) Jang, J.; Liu, W.; Son, J. S.; Talapin, D. V. Temperature-Dependent Hall and Field-Effect Mobility in Strongly Coupled All-Inorganic Nanocrystal Arrays. *Nano Lett.* **2014**, *14*, 653−662.
(158) Liu, W.; Lee, J.-S.; Talapin, D. V. III-V Nanocrystals Capped with Molecular Metal Chalcogenide Ligands: High Electron Mobility and Ambipolar Photoresponse. *J. Am. Chem. Soc.* **2013**, *135*, 1349−1357.
(159) Lee, J.-S.; Kovalenko, M. V.; Huang, J.; Chung, D. S.; Talapin, D. V. Band-Like Transport, High Electron Mobility and High Photoconductivity in All-Inorganic Nanocrystal Arrays. *Nat. Nanotechnol.* **2011**, *6*, 348−352.
(160) Kovalenko, M. V.; Manna, L.; Cabot, A.; Hens, Z.; Talapin, D. V.; Kagan, C. R.; Klimov, V. I.; Rogach, A. L.; Reiss, P.; Milliron, D. J.; et al. Prospects of Nanoscience with Nanocrystals. *ACS Nano* **2015**, *9*, 1012−1057.
(161) Dolzhnikov, D. S.; Zhang, H.; Jang, J.; Son, J. S.; Panthani, M. G.; Shibata, T.; Chattopadhyay, S.; Talapin, D. V. Composition-Matched Molecular "Solders" for Semiconductors. *Science* **2015**, *347*, 425−428.
(162) Kalesaki, E.; Evers, W. H.; Allan, G.; Vanmaekelbergh, D.; Delerue, C. Electronic Structure of Atomically Coherent Square Semiconductor Superlattices with Dimensionality Below Two. *Phys. Rev. B: Condens. Matter Mater. Phys.* **2013**, *88*, 115431.
(163) Kalesaki, E.; Boneschanscher, M. P.; Geuchies, J. J.; Delerue, C.; Morais Smith, C.; Evers, W. H.; Allan, G.; Altantzis, T.; Bals, S.; Vanmaekelbergh, D. Preparation and Study of 2-D Semiconductors with Dirac Type Bands Due to the Honeycomb Nanogeometry. *Proc. SPIE* **2014**, *8981*, 898107.
(164) Kalesaki, E.; Delerue, C.; Morais Smith, C.; Beugeling, W.; Allan, G.; Vanmaekelbergh, D. Dirac Cones, Topological Edge States, and Nontrivial Flat Bands in Two-Dimensional Semiconductors with a Honeycomb Nanogeometry. *Phys. Rev. X* **2014**, *4*, 011010.
(165) Beugeling, W.; Kalesaki, E.; Delerue, C.; Niquet, Y. M.; Vanmaekelbergh, D.; Smith, C. M. Topological States in Multi-Orbital HgTe Honeycomb Lattices. *Nat. Commun.* **2015**, *6*, 6316−6316.

DOI: 10.1021/acs.chemrev.5b00678
Chem. Rev. 2016, 116, 11181−11219

(166) Beugeling, W.; Kalesaki, E.; Delerue, C.; Niquet, Y. M.; Vanmaekelbergh, D.; Morais Smith, C. Topological States in Multi-Orbital HgTe Honeycomb Lattices. *Nat. Commun.* **2015**, *6*, 6316.
(167) Delerue, C. Prediction of Robust Two-Dimensional Topological Insulators Based on Ge/Si Nanotechnology. *Phys. Rev. B: Condens. Matter Mater. Phys.* **2014**, *90*, 075424.
(168) Sushkov, O. P.; Castro Neto, A. H. Topological Insulating States in Laterally Patterned Ordinary Semiconductors. *Phys. Rev. Lett.* **2013**, *110*, 186601.
(169) MedeirosRibeiro, G.; Pikus, F. G.; Petroff, P. M.; Efros, A. L. Single-Electron Charging and Coulomb Interaction in InAs Self-Assembled Quantum Dot Arrays. *Phys. Rev. B: Condens. Matter Mater. Phys.* **1997**, *55*, 1568−1573.
(170) Hameau, S.; Guldner, Y.; Verzelen, O.; Ferreira, R.; Bastard, G.; Zeman, J.; Lemaitre, A.; Gerard, J. M. Strong Electron-Phonon Coupling Regime in Quantum Dots: Evidence for Everlasting Resonant Polarons. *Phys. Rev. Lett.* **1999**, *83*, 4152−4155.
(171) Hapke-Wurst, I.; Zeitler, U.; Schumacher, H. W.; Haug, R. J.; Pierz, K.; Ahlers, F. J. Size Determination of InAs Quantum Dots Using Magneto-Tunnelling Experiments. *Semicond. Sci. Technol.* **1999**, *14*, L41−L43.
(172) Lundstrom, T.; Schoenfeld, W.; Lee, H.; Petroff, P. M. Exciton Storage in Semiconductor Self-Assembled Quantum Dots. *Science* **1999**, *286*, 2312−2314.
(173) Luyken, R. J.; Lorke, A.; Govorov, A. O.; Kotthaus, J. P.; Medeiros-Ribeiro, G.; Petroff, P. M. The Dynamics of Tunneling into Self-Assembled InAs Dots. *Appl. Phys. Lett.* **1999**, *74*, 2486−2488.
(174) Robinson, L. M.; Rho, H.; Kim, J. C.; Jackson, H. E.; Smith, L. M.; Lee, S.; Dobrowolska, M.; Furdyna, J. K. Quantum Dot Exciton Dynamics through a Nanoaperture: Evidence for Two Confined States. *Phys. Rev. Lett.* **1999**, *83*, 2797−2800.
(175) Hawrylak, P.; Narvaez, G. A.; Bayer, M.; Forchel, A. Excitonic Absorption in a Quantum Dot. *Phys. Rev. Lett.* **2000**, *85*, 389−392.
(176) Patane, A.; Polimeni, A.; Eaves, L.; Main, P. C.; Henini, M.; Dubrovskii, Y. V.; Belyaev, A. E.; Brounkov, P. N.; Vdovin, E. E.; Khanin, Y. N.; et al. Resonant Tunneling and Photoluminescence Spectroscopy in Quantum Wells Containing Self-Assembled Quantum Dots. *J. Appl. Phys.* **2000**, *88*, 2005−2012.
(177) Vdovin, E. E.; Levin, A.; Patane, A.; Eaves, L.; Main, P. C.; Khanin, Yu. N.; Dubrovskii, Yu. V.; Henini, M.; Hill, G. Imaging the Electron Wave Function in Self-Assembled Quantum Dots. *Science* **2000**, *290*, 122−124.
(178) Williamson, A. J.; Wang, L. W.; Zunger, A. Theoretical Interpretation of the Experimental Electronic Structure of Lens-Shaped Self-Assembled InAs/GaAs Quantum Dots. *Phys. Rev. B: Condens. Matter Mater. Phys.* **2000**, *62*, 12963−12977.
(179) Williamson, A. J.; Franceschetti, A.; Zunger, A. Multi-Excitons in Self-Assembled InAs/GaAs Quantum Dots: A Pseudopotential, Many-Body Approach. *Europhys. Lett.* **2001**, *53*, 59−65.
(180) Zwiller, V.; Blom, H.; Jonsson, P.; Panev, N.; Jeppesen, S.; Tsegaye, T.; Goobar, E.; Pistol, M. E.; Samuelson, L.; Bjork, G. Single Quantum Dots Emit Single Photons at a Time: Antibunching Experiments. *Appl. Phys. Lett.* **2001**, *78*, 2476−2478.
(181) Hakanson, U.; Johansson, M. K. J.; Persson, J.; Johansson, J.; Pistol, M. E.; Montelius, L.; Samuelson, L. Single InP/GaInP Quantum Dots Studied by Scanning Tunneling Microscopy and Scanning Tunneling Microscopy Induced Luminescence. *Appl. Phys. Lett.* **2002**, *80*, 494−496.
(182) Kiraz, A.; Falth, S.; Becher, C.; Gayral, B.; Schoenfeld, W. V.; Petroff, P. M.; Zhang, L.; Hu, E.; Imamoglu, A. Photon Correlation Spectroscopy of a Single Quantum Dot. *Phys. Rev. B: Condens. Matter Mater. Phys.* **2002**, *65*, 161303.
(183) Patane, A.; Hill, R. J. A.; Eaves, L.; Main, P. C.; Henini, M.; Zambrano, M. L.; Levin, A.; Mori, N.; Hamaguchi, C.; Dubrovskii, Y. V. Probing the Quantum States of Self-Assembled InAs Dots by Magnetotunneling Spectroscopy. *Phys. Rev. B: Condens. Matter Mater. Phys.* **2002**, *65*, 165308.
(184) Sebald, K.; Michler, P.; Passow, T.; Hommel, D.; Bacher, G.; Forchel, A. Single-Photon Emission of CdSe Quantum Dots at Temperatures up to 200 K. *Appl. Phys. Lett.* **2002**, *81*, 2920−2922.
(185) Bruls, D. M.; Koenraad, P. M.; Salemink, H. W. M.; Wolter, J. H.; Hopkinson, M.; Skolnick, M. S. Stacked Low-Growth-Rate InAs Quantum Dots Studied at the Atomic Level by Cross-Sectional Scanning Tunneling Microscopy. *Appl. Phys. Lett.* **2003**, *82*, 3758−3760.
(186) Mackowski, S.; Jackson, H. E.; Smith, L. M.; Kossut, J.; Karczewski, G.; Heiss, W. Tuning the Properties of Magnetic Cdmnte Quantum Dots. *Appl. Phys. Lett.* **2003**, *83*, 3575−3577.
(187) Gong, Q.; Offermans, P.; Notzel, R.; Koenraad, P. M.; Wolter, J. H. Capping Process of InAs/GaAs Quantum Dots Studied by Cross-Sectional Scanning Tunneling Microscopy. *Appl. Phys. Lett.* **2004**, *85*, 5697−5699.
(188) Nguyen, T. A.; Mackowski, S.; Jackson, H. E.; Smith, L. M.; Wrobel, J.; Fronc, K.; Karczewski, G.; Kossut, J.; Dobrowolska, M.; Furdyna, J. K.; et al. Resonant Spectroscopy of II-VI Self-Assembled Quantum Dots: Excited States and Exciton-Longitudinal Optical Phonon Coupling. *Phys. Rev. B: Condens. Matter Mater. Phys.* **2004**, *70*, 125306.
(189) Blokland, J. H.; Wijnen, F. J. P.; Christianen, P. C. M.; Zeitler, U.; Maan, J. C. Hole Levels in InAs Self-Assembled Quantum Dots. *Phys. Rev. B: Condens. Matter Mater. Phys.* **2007**, *75*, 233305.
(190) Springholz, G.; Abtin, L.; Holy, V. Shape and Composition of Buried PbSe Quantum Dots Determined by Scanning Tunneling Microscopy. *Appl. Phys. Lett.* **2007**, *90*, 113119.
(191) Marquardt, B.; Geller, M.; Lorke, A.; Reuter, D.; Wieck, A. D. Using a Two-Dimensional Electron Gas to Study Nonequilibrium Tunneling Dynamics and Charge Storage in Self-Assembled Quantum Dots. *Appl. Phys. Lett.* **2009**, *95*, 022113.
(192) Giddings, A. D.; Keizer, J. G.; Hara, M.; Hamhuis, G. J.; Yuasa, H.; Fukuzawa, H.; Koenraad, P. M. Composition Profiling of InAs Quantum Dots and Wetting Layers by Atom Probe Tomography and Cross-Sectional Scanning Tunneling Microscopy. *Phys. Rev. B: Condens. Matter Mater. Phys.* **2011**, *83*, 205308.
(193) Keizer, J. G.; Bozkurt, M.; Bocquel, J.; Koenraad, P. M.; Mano, T.; Noda, T.; Sakoda, K.; Clark, E. C.; Bichler, M.; Abstreiter, G.; et al. Shape Control of Quantum Dots Studied by Cross-Sectional Scanning Tunneling Microscopy. *J. Appl. Phys.* **2011**, *109*, 102413.
(194) Shibata, K.; Umeno, A.; Cha, K. M.; Hirakawa, K. Photon-Assisted Tunneling through Self-Assembled InAs Quantum Dots in the Terahertz Frequency Range. *Phys. Rev. Lett.* **2012**, *109*, 077401.
(195) Talapin, D. V.; Lee, J.-S.; Kovalenko, M. V.; Shevchenko, E. V. Prospects of Colloidal Nanocrystals for Electronic and Optoelectronic Applications. *Chem. Rev.* **2010**, *110*, 389−458.
(196) Akkerman, Q. A.; Genovese, A.; George, C.; Prato, M.; Moreels, I.; Casu, A.; Marras, S.; Curcio, A.; Scarpellini, A.; Pellegrino, T.; et al. From Binary Cu_2S to Ternary Cu-In-S and Quaternary Cu-In-Zn-S Nanocrystals with Tunable Composition Via Partial Cation Exchange. *ACS Nano* **2015**, *9*, 521−531.
(197) Stolle, C. J.; Harvey, T. B.; Pernik, D. R.; Hibbert, J. I.; Du, J.; Rhee, D. J.; Akhavan, V. A.; Schaller, R. D.; Korgel, B. A. Multiexciton Solar Cells of $CuInSe_2$ Nanocrystals. *J. Phys. Chem. Lett.* **2014**, *5*, 304−309.
(198) Han, Z.; Zhang, D.; Chen, Q.; Hong, R.; Tao, C.; Huang, Y.; Ni, Z.; Zhuang, S. Synthesis of Single Phase Chalcopyrite $CuIn_{1-X}Ga_xSe_2$ ($0 \leq X \leq 1$) Nanoparticles by One-Pot Method. *Mater. Res. Bull.* **2014**, *51*, 302−308.
(199) Chen, Z.; Xie, C.; Yang, F.; Feng, L.; Liang, X.; Xiang, W. Controllable Synthesis of Colloidal $CuInS_2$ Nanocrystals with Tunable Structures and Its Nonlinear Optical Properties. *J. Alloys Compd.* **2014**, *594*, 107−113.
(200) Asgary, S.; Mirabbaszadeh, K.; Nayebi, P.; Emadi, H. Synthesis and Investigation of Optical Properties of Topo-Capped $CuInS_2$ Semiconductor Nanocrystal in the Presence of Different Solvent. *Mater. Res. Bull.* **2014**, *51*, 411−417.
(201) Panthani, M. G.; Stolle, C. J.; Reid, D. K.; Rhee, D. J.; Harvey, T. B.; Akhavan, V. A.; Yu, Y.; Korgel, B. A. $CuInSe_2$ Quantum Dot

DOI: 10.1021/acs.chemrev.5b00678
Chem. Rev. 2016, 116, 11181−11219

Solar Cells with High Open-Circuit Voltage. *J. Phys. Chem. Lett.* **2013**, *4*, 2030−2034.
(202) McDaniel, H.; Fuke, N.; Pietryga, J. M.; Klimov, V. I. Engineered $CuInSe_xS_{2-X}$ Quantum Dots for Sensitized Solar Cells. *J. Phys. Chem. Lett.* **2013**, *4*, 355−361.
(203) Liu, Z.; Wang, L.; Hao, Q.; Wang, D.; Tang, K.; Zuo, M.; Yang, Q. Facile Synthesis and Characterization of $CuInS_2$ Nanocrystals with Different Structures and Shapes. *CrystEngComm* **2013**, *15*, 7192−7198.
(204) Yarema, M.; Kovalenko, M. V. Colloidal Synthesis of InSb Nanocrystals with Controlled Polymorphism Using Indium and Antimony Amides. *Chem. Mater.* **2013**, *25*, 1788−1792.
(205) Protesescu, L.; Yakunin, S.; Bodnarchuk, M. I.; Krieg, F.; Caputo, R.; Hendon, C. H.; Yang, R. X.; Walsh, A.; Kovalenko, M. V. Nanocrystals of Cesium Lead Halide Perovskites (CsPbX3, X = Cl, Br, and I): Novel Optoelectronic Materials Showing Bright Emission with Wide Color Gamut. *Nano Lett.* **2015**, *15*, 3692−3696.
(206) Akkerman, Q. A.; D'Innocenzo, V.; Accornero, S.; Scarpellini, A.; Petrozza, A.; Prato, M.; Manna, L. Tuning the Optical Properties of Cesium Lead Halide Perovskite Nanocrystals by Anion Exchange Reactions. *J. Am. Chem. Soc.* **2015**, *137*, 10276−10281.
(207) Flissikowski, T.; Hundt, A.; Lowisch, M.; Rabe, M.; Henneberger, F. Photon Beats from a Single Semiconductor Quantum Dot. *Phys. Rev. Lett.* **2001**, *86*, 3172−3175.
(208) Moreau, E.; Robert, I.; Gerard, J. M.; Abram, I.; Manin, L.; Thierry-Mieg, V. Single-Mode Solid-State Single Photon Source Based on Isolated Quantum Dots in Pillar Microcavities. *Appl. Phys. Lett.* **2001**, *79*, 2865−2867.
(209) Regelman, D. V.; Dekel, E.; Gershoni, D.; Ehrenfreund, E.; Williamson, A. J.; Shumway, J.; Zunger, A.; Schoenfeld, W. V.; Petroff, P. M. Optical Spectroscopy of Single Quantum Dots at Tunable Positive, Neutral, and Negative Charge States. *Phys. Rev. B: Condens. Matter Mater. Phys.* **2001**, *64*, 165301.
(210) Santori, C.; Pelton, M.; Solomon, G.; Dale, Y.; Yamamoto, E. Triggered Single Photons from a Quantum Dot. *Phys. Rev. Lett.* **2001**, *86*, 1502−1505.
(211) van Sark, W. G. J. H. M.; Frederix, P. L. T. M.; Asselbergs, M. A. H.; van den Heuvel, D. J.; Meijerink, A.; Gerritsen, H. C. Spectral Imaging of Single CdSe/ZnS Quantum Dots Employing Spectrally- and Time-Resolved Confocal Microscopy. In *Fluorescence Spectroscopy, Imaging and Probes*; Springer Series on Fluorescence; Springer: Berlin/Heidelberg, 2002; Vol. *2*, pp 317−335.10.1007/978-3-642-56067-5_19
(212) van Sark, W.; Frederix, P.; Bol, A. A.; Gerritsen, H. C.; Meijerink, A. Blueing, Bleaching, and Blinking of Single CdSe/ZnS Quantum Dots. *ChemPhysChem* **2002**, *3*, 871−879.
(213) Besombes, L.; Kheng, K.; Marsal, L.; Mariette, H. Excited States and Multi-Exciton Complexes in Single CdTe Quantum Dots. *Europhys. Lett.* **2004**, *65*, 144−150.
(214) Fisher, B. R.; Eisler, H. J.; Stott, N. E.; Bawendi, M. G. Emission Intensity Dependence and Single-Exponential Behavior in Single Colloidal Quantum Dot Fluorescence Lifetimes. *J. Phys. Chem. B* **2004**, *108*, 143−148.
(215) Peterson, J. J.; Krauss, T. D. Fluorescence Spectroscopy of Single Lead Sulfide Quantum Dots. *Nano Lett.* **2006**, *6*, 510−514.
(216) Osovsky, R.; Cheskis, D.; Kloper, V.; Sashchiuk, A.; Kroner, M.; Lifshitz, E. Continuous-Wave Pumping of Multiexciton Bands in the Photoluminescence Spectrum of a Single CdTe-CdSe Core-Shell Colloidal Quantum Dot. *Phys. Rev. Lett.* **2009**, *102*, 197401.
(217) Wu, X. W.; Gong, M.; Dong, C. H.; Cui, J. M.; Yang, Y.; Han, Z. F.; Guo, G. C. Anti-Bunching from Plasmon Induced Non-Blinking Single CdSe/ZnS Quantum Dot. 2010 IEEE 3rd International Nanoelectronics Conference (INEC), Hong Kong, China, Jan 3−8, 2010; Chu, P. K. I., Ed.; pp 299−300.
(218) Vanmaekelbergh, D.; Casavola, M. Single-Dot Microscopy and Spectroscopy for Comprehensive Study of Colloidal Nanocrystals. *J. Phys. Chem. Lett.* **2011**, *2*, 2024−2031.
(219) Buckley, S.; Rivoire, K.; Vuckovic, J. Engineered Quantum Dot Single-Photon Sources. *Rep. Prog. Phys.* **2012**, *75*, 126503.
(220) Manceau, M.; Vezzoli, S.; Glorieux, Q.; Pisanello, F.; Giacobino, E.; Carbone, L.; De Vittorio, M.; Bramati, A. Effect of Charging on CdSe/CdS Dot-in-Rods Single-Photon Emission. *Phys. Rev. B: Condens. Matter Mater. Phys.* **2014**, *90*, 035311.
(221) Park, Y.-S.; Bae, W. K.; Padilha, L. A.; Pietryga, J. M.; Klimov, V. I. Effect of the Core/Shell Interface on Auger Recombination Evaluated by Single-Quantum-Dot Spectroscopy. *Nano Lett.* **2014**, *14*, 396−402.
(222) Nirmal, M.; Dabbousi, B. O.; Bawendi, M. G.; Macklin, J. J.; Trautman, J. K.; Harris, T. D.; Brus, L. E. Fluorescence Intermittency in Single Cadmium Selenide Nanocrystals. *Nature* **1996**, *383*, 802−804.
(223) Brus, L. Spectroscopy and "Blinking" of Single Semiconductor Nanocrystals at Room Temperature. *Book of Abstracts*; 215th ACS National Meeting, Dallas, TX, March 29−April 2, 1998; PHYS-195.
(224) Kuno, M.; Fromm, D. P.; Hamann, H. F.; Gallagher, A.; Nesbitt, D. J. Nonexponential "Blinking" Kinetics of Single CdSe Quantum Dots: A Universal Power Law Behavior. *J. Chem. Phys.* **2000**, *112*, 3117−3120.
(225) Chen, Y.; Vela, J.; Htoon, H.; Casson, J. L.; Werder, D. J.; Bussian, D. A.; Klimov, V. I.; Hollingsworth, J. A. "Giant" Multishell CdSe Nanocrystal Quantum Dots with Suppressed Blinking. *J. Am. Chem. Soc.* **2008**, *130*, 5026−5027.
(226) Kloper, V.; Osovsky, R.; Cheskis, D.; Sashchiuk, A.; Lifshitz, E. Suppressed blinking in CdTe/CdSe core-shell quantum dots. *Phys. Status Solidi C* **2009**, *6*, 2719−2721.
(227) Peterson, J. J.; Nesbitt, D. J. Modified Power Law Behavior in Quantum Dot Blinking: A Novel Role for Biexcitons and Auger Ionization. *Nano Lett.* **2009**, *9*, 338−345.
(228) Spinicelli, P.; Buil, S.; Quelin, X.; Mahler, B.; Dubertret, B.; Hermier, J. P. Bright and Grey States in CdSe-CdS Nanocrystals Exhibiting Strongly Reduced Blinking. *Phys. Rev. Lett.* **2009**, *102*, 136801.
(229) Spinicelli, P.; Mahler, B.; Buil, S.; Quelin, X.; Dubertret, B.; Hermier, J.-P. Non-Blinking Semiconductor Colloidal Quantum Dots for Biology, Optoelectronics and Quantum Optics. *ChemPhysChem* **2009**, *10*, 879−882.
(230) Krauss, T. D.; Peterson, J. J. Bright Future for Fluorescence Blinking in Semiconductor Nanocrystals. *J. Phys. Chem. Lett.* **2010**, *1*, 1377−1382.
(231) Dennis, A. M.; Mangum, B. D.; Piryatinski, A.; Park, Y. S.; Hannah, D. C.; Casson, J. L.; Williams, D. J.; Schaller, R. D.; Htoon, H.; Hollingsworth, J. A. Suppressed Blinking and Auger Recombination in near-Infrared Type-II InP/CdS Nanocrystal Quantum Dots. *Nano Lett.* **2012**, *12*, 5545−5551.
(232) Qin, W.; Guyot-Sionnest, P. Evidence for the Role of Holes in Blinking: Negative and Oxidized CdSe/CdS Dots. *ACS Nano* **2012**, *6*, 9125−9132.
(233) Qin, W.; Shah, R. A.; Guyot-Sionnest, P. CdSeS/ZnS Alloyed Nanocrystal Lifetime and Blinking Studies under Electrochemical Control. *ACS Nano* **2012**, *6*, 912−918.
(234) Hollingsworth, J. A.; Htoon, H.; Kundu, J.; Pal, B. N.; Ghosh, Y.; Dennis, A. M.; Acharya, K.; Mangum, B. D.; Ma, X. "Giant" Heterostructured Nanocrystal Quantum Dots: From Suppressed Blinking to Solid-State Lighting. *Abstr. Pap., Am. Chem. Soc.* **2013**, *246*.
(235) Canneson, D.; Biadala, L.; Buil, S.; Quelin, X.; Javaux, C.; Dubertret, B.; Hermier, J. P. Blinking Suppression and Biexcitonic Emission in Thick-Shell CdSe/CdS Nanocrystals at Cryogenic Temperature. *Phys. Rev. B: Condens. Matter Mater. Phys.* **2014**, *89*, 035303.
(236) Fukuda, M.; Nakagawa, K.; Miyazaki, S.; Hirose, M. Resonant Tunneling through a Self-Assembled Si Quantum Dot. *Appl. Phys. Lett.* **1997**, *70*, 2291−2293.
(237) Suzuki, T.; Nomoto, K.; Taira, K.; Hase, I. Tunneling Spectroscopy of InAs Wetting Layers and Self-Assembled Quantum Dots: Resonant Tunneling through Two- and Zero-Dimensional Electronic States. *Jpn. J. Appl. Phys.* **1997**, *36*, 1917−1921.

DOI: 10.1021/acs.chemrev.5b00678
Chem. Rev. 2016, 116, 11181−11219

(238) Wu, W.; Tucker, J. R.; Solomon, G. S.; Harris, J. S. Atom-Resolved Scanning Tunneling Microscopy of Vertically Ordered InAs Quantum Dots. *Appl. Phys. Lett.* **1997**, *71*, 1083−1085.
(239) Legrand, B.; Grandidier, B.; Nys, J. P.; Stievenard, D.; Gerard, J. M.; Thierry-Mieg, V. Scanning Tunneling Microscopy and Scanning Tunneling Spectroscopy of Self Assembled InAs Quantum Dots. *Appl. Phys. Lett.* **1998**, *73*, 96−98.
(240) Liu, N.; Lyeo, H. K.; Shih, C. K.; Oshima, M.; Mano, T.; Koguchi, N. Cross-Sectional Scanning Tunneling Microscopy Study of InGaAs Quantum Dots on GaAs(001) Grown by Heterogeneous Droplet Epitaxy. *Appl. Phys. Lett.* **2002**, *80*, 4345−4347.
(241) Maltezopoulos, T.; Bolz, A.; Meyer, C.; Heyn, C.; Hansen, W.; Morgenstern, M.; Wiesendanger, R. Wave-Function Mapping of InAs Quantum Dots by Scanning Tunneling Spectroscopy. *Phys. Rev. Lett.* **2003**, *91*, 196804.
(242) Ouattara, L.; Mikkelsen, A.; Lundgren, E.; Borgstrom, M.; Samuelson, L.; Seifert, W. Stacked InAs Quantum Dots in InP Studied by Cross-Sectional Scanning Tunnelling Microscopy. *Nanotechnology* **2004**, *15*, 1701−1707.
(243) Mahieu, G.; Grandidier, B.; Deresmes, D.; Nys, J. P.; Stievenard, D.; Ebert, P. Direct Evidence for Shallow Acceptor States with Nonspherical Symmetry in GaAs. *Phys. Rev. Lett.* **2005**, *94*, 026407.
(244) Ouattara, L.; Mikkelsen, A.; Lundgren, E.; Hoglund, L.; Asplund, C.; Andersson, J. Y. A Cross-Sectional Scanning Tunneling Microscopy Study of a Quantum Dot Infrared Photodetector Structure. *J. Appl. Phys.* **2006**, *100*, 044320.
(245) Murata, Y.; Kimura, T.; Matsumoto, T.; Honda, S.-i.; Katayama, M. Scanning Tunneling Microscopy Imaging of Facet Surfaces of Self-Organized Nanocrystal Using Metal-Coated Carbon Nanotube Tip. *Surf. Sci.* **2008**, *602*, L29−L32.
(246) Suto, H.; Murata, Y.; Matsumoto, T.; Enomoto, Y.; Morifuji, M.; Honda, S.-i.; Katayama, M. Scanning Tunneling Microscopy and Spectroscopy Study of a Steep Facet Surface on Ge Nanocrystal Grown on Si(111). *Appl. Phys. Express* **2009**, *2*, 035002.
(247) Ulloa, J. M.; Bozkurt, M.; Koenraad, P. M. Intrinsic and Mn Doped InAs Quantum Dots Studied at the Atomic Scale by Cross-Sectional Scanning Tunneling Microscopy. *Solid State Commun.* **2009**, *149*, 1410−1418.
(248) Ulloa, J. M.; Gargallo-Caballero, R.; Bozkurt, M.; del Moral, M.; Guzman, A.; Koenraad, P. M.; Hierro, A. GaAsSb-Capped InAs Quantum Dots: From Enlarged Quantum Dot Height to Alloy Fluctuations. *Phys. Rev. B: Condens. Matter Mater. Phys.* **2010**, *81*, 165305.
(249) Ulloa, J. M.; Koenraad, P. M.; Bonnet-Eymard, M.; Letoublon, A.; Bertru, N. Effect of a Lattice-Matched GaAsSb Capping Layer on the Structural Properties of InAs/Ingaas/InP Quantum Dots. *J. Appl. Phys.* **2010**, *107*, 074309.
(250) Ulloa, J. M.; Llorens, J. M.; del Moral, M.; Bozkurt, M.; Koenraad, P. M.; Hierro, A. Analysis of the Modified Optical Properties and Band Structure of $GaAs_{1-X}Sb_x$-Capped InAs/GaAs Quantum Dots. *J. Appl. Phys.* **2012**, *112*, 074311.
(251) Gaan, S.; He, G.; Feenstra, R. M.; Walker, J.; Towe, E. Size, Shape, Composition, and Electronic Properties of InAs/GaAs Quantum Dots by Scanning Tunneling Microscopy and Spectroscopy. *J. Appl. Phys.* **2010**, *108*, 114315.
(252) Fain, B.; Robert-Philip, I.; Beveratos, A.; David, C.; Wang, Z. Z.; Sagnes, I.; Girard, J. C. Discretization of Electronic States in Large InAsP/InP Multilevel Quantum Dots Probed by Scanning Tunneling Spectroscopy. *Phys. Rev. Lett.* **2012**, *108*, 126808.
(253) Keizer, J. G.; Clark, E. C.; Bichler, M.; Abstreiter, G.; Finley, J. J.; Koenraad, P. M. An Atomically Resolved Study of InGaAs Quantum Dot Layers Grown with an Indium Flush Step. *Nanotechnology* **2010**, *21*, 215705.
(254) Keizer, J. G.; Henriques, A. B.; Maia, A. D. B.; Quivy, A. A.; Koenraad, P. M. Atomically Resolved Study of the Morphology Change of InAs/GaAs Quantum Dot Layers Induced by Rapid Thermal Annealing. *Appl. Phys. Lett.* **2012**, *101*, 243113.
(255) Keizer, J. G.; Koenraad, P. M.; Smereka, P.; Ulloa, J. M.; Guzman, A.; Hierro, A. Kinetic Monte Carlo Simulations and Cross-Sectional Scanning Tunneling Microscopy as Tools to Investigate the Heteroepitaxial Capping of Self-Assembled Quantum Dots. *Phys. Rev. B: Condens. Matter Mater. Phys.* **2012**, *85*, 155326.
(256) Keizer, J. G.; Jo, M.; Mano, T.; Noda, T.; Sakodam, K.; Koenraad, P. M. Structural Atomic-Scale Analysis of GaAs/AlGaAs Quantum Wires and Quantum Dots Grown by Droplet Epitaxy on a (311)A Substrate. *Appl. Phys. Lett.* **2011**, *98*, 193112.
(257) Smakman, E. P.; Garleff, J. K.; Young, R. J.; Hayne, M.; Rambabu, P.; Koenraad, P. M. GaSb/GaAs Quantum Dot Formation and Demolition Studied with Cross-Sectional Scanning Tunneling Microscopy. *Appl. Phys. Lett.* **2012**, *100*, 142116.
(258) Yamagishi, M.; Watase, N.; Hashisaka, M.; Muraki, K.; Fujisawa, T. Spin-Dependent Tunneling Rates for Electrostatically Defined GaAs Quantum Dots. *Phys. Rev. B: Condens. Matter Mater. Phys.* **2014**, *90*, 035306.
(259) Ota, T.; Rontani, M.; Tarucha, S.; Nakata, Y.; Song, H. Z.; Miyazawa, T.; Usuki, T.; Takatsu, M.; Yokoyama, N. Few-Electron Molecular States and Their Transitions in a Single InAs Quantum Dot Molecule. *Phys. Rev. Lett.* **2005**, *95*, 236801.
(260) Rontani, M.; Molinari, E. Imaging Quasiparticle Wave Functions in Quantum Dots Via Tunneling Spectroscopy. *Phys. Rev. B: Condens. Matter Mater. Phys.* **2005**, *71*, 233106.
(261) Maruccio, G.; Janson, M.; Schramm, A.; Meyer, C.; Matsui, T.; Heyn, C.; Hansen, W.; Wiesendanger, R.; Rontani, M.; Molinari, E. Correlation Effects in Wave Function Mapping of Molecular Beam Epitaxy Grown Quantum Dots. *Nano Lett.* **2007**, *7*, 2701−2706.
(262) Eisele, H.; Flebbe, O.; Kalka, T.; Preinesberger, C.; Heinrichsdorff, F.; Krost, A.; Bimberg, D.; Dahne-Prietsch, M. Cross-Sectional Scanning-Tunneling Microscopy of Stacked InAs Quantum Dots. *Appl. Phys. Lett.* **1999**, *75*, 106−108.
(263) Legrand, B.; Nys, J. P.; Grandidier, B.; Stievenard, D.; Lemaitre, A.; Gerard, J. M.; Thierry-Mieg, V. Quantum Box Size Effect on Vertical Self-Alignment Studied Using Cross-Sectional Scanning Tunneling Microscopy. *Appl. Phys. Lett.* **1999**, *74*, 2608−2610.
(264) Grandidier, B.; Niquet, Y. M.; Legrand, B.; Nys, J. P.; Priester, C.; Stievenard, D.; Gerard, J. M.; Thierry-Mieg, V. Imaging the Wave-Function Amplitudes in Cleaved Semiconductor Quantum Boxes. *Phys. Rev. Lett.* **2000**, *85*, 1068−1071.
(265) Grandidier, B.; Nys, J. P.; Delerue, C.; Stievenard, D.; Higo, Y.; Tanaka, M. Atomic-Scale Study of (Ga,Mn)As/GaAs Layers. *Appl. Phys. Lett.* **2000**, *77*, 4001−4003.
(266) Springholz, G.; Pinczolits, M.; Bauer, G.; Kang, H. H.; Salamanca-Riba, L. Phase Diagram of Lateral and Vertical Ordering in Self-Organized PbSe Quantum Dot Superlattice Grown Mbe. *J. Cryst. Growth* **2001**, *227-228*, 1126−1131.
(267) Kleemans, N.; van Bree, J.; Bozkurt, M.; van Veldhoven, P. J.; Nouwens, P. A.; Notzel, R.; Silov, A. Y.; Koenraad, P. M.; Flatte, M. E. Size-Dependent Exciton G Factor in Self-Assembled InAs/InP Quantum Dots. *Phys. Rev. B: Condens. Matter Mater. Phys.* **2009**, *79*, 045311.
(268) Taboada, A. G.; Sanchez, A. M.; Beltran, A. M.; Bozkurt, M.; Alonso-Alvarez, D.; Alen, B.; Rivera, A.; Ripalda, J. M.; Llorens, J. M.; Martin-Sanchez, J.; et al. Structural and Optical Changes Induced by Incorporation of Antimony into InAs/GaAs(001) Quantum Dots. *Phys. Rev. B: Condens. Matter Mater. Phys.* **2010**, *82*, 235316.
(269) Bozkurt, M.; Ulloa, J. M.; Koenraad, P. M. An Atomic Scale Study on the Effect of Sb During Capping of MBE Grown III-V Semiconductor Qds. *Semicond. Sci. Technol.* **2011**, *26*, 064007.
(270) Garleff, J. K.; Wijnheijmer, A. P.; Koenraad, P. M. Challenges in Cross-Sectional Scanning Tunneling Microscopy on Semiconductors. *Semicond. Sci. Technol.* **2011**, *26*, 064001.
(271) Mauger, S. J. C.; Bozkurt, M.; Koenraad, P. M.; Giddings, A. D.; Campion, R. P.; Gallagher, B. L. Short-Period (Ga,Mn)As/(Al,Ga)As Multilayer Structures Studied by Cross-Sectional Scanning Tunneling Microscopy. *Phys. Rev. B: Condens. Matter Mater. Phys.* **2011**, *84*, 104432.

DOI: 10.1021/acs.chemrev.5b00678
Chem. Rev. 2016, 116, 11181−11219

(272) Jovanov, V.; Eissfeller, T.; Kapfinger, S.; Clark, E. C.; Klotz, F.; Bichler, M.; Keizer, J. G.; Koenraad, P. M.; Brandt, M. S.; Abstreiter, G.; et al. Highly Nonlinear Excitonic Zeeman Spin Splitting in Composition-Engineered Artificial Atoms. *Phys. Rev. B: Condens. Matter Mater. Phys.* **2012**, *85*, 165433.
(273) Nowozin, T.; Marent, A.; Bonato, L.; Schliwa, A.; Bimberg, D.; Smakman, E. P.; Garleff, J. K.; Koenraad, P. M.; Young, R. J.; Hayne, M. Linking Structural and Electronic Properties of High-Purity Self-Assembled GaSb/GaAs Quantum Dots. *Phys. Rev. B: Condens. Matter Mater. Phys.* **2012**, *86*, 035305.
(274) Hayne, M.; Young, R. J.; Smakman, E. P.; Nowozin, T.; Hodgson, P.; Garleff, J. K.; Rambabu, P.; Koenraad, P. M.; Marent, A.; Bonato, L.; et al. The Structural, Electronic and Optical Properties of GaSb/GaAs Nanostructures for Charge-Based Memory. *J. Phys. D: Appl. Phys.* **2013**, *46*, 264001.
(275) Martin, A. J.; Hwang, J.; Marquis, E. A.; Smakman, E.; Saucer, T. W.; Rodriguez, G. V.; Hunter, A. H.; Sih, V.; Koenraad, P. M.; Phillips, J. D. The Disintegration of GaSb/GaAs Nanostructures Upon Capping. *Appl. Phys. Lett.* **2013**, *102*, 113103.
(276) Urbanczyk, A.; Keizer, J. G.; Koenraad, P. M.; Noetzel, R. Long Wavelength (> 1.55 Mu M) Room Temperature Emission and Anomalous Structural Properties of InAs/GaAs Quantum Dots Obtained by Conversion of in Nanocrystals. *Appl. Phys. Lett.* **2013**, *102*, 073103.
(277) Liljeroth, P.; van Emmichoven, P. A. Z.; Hickey, S. G.; Weller, H.; Grandidier, B.; Allan, G.; Vanmaekelbergh, D. Density of States Measured by Scanning-Tunneling Spectroscopy Sheds New Light on the Optical Transitions in PbSe Nanocrystals. *Phys. Rev. Lett.* **2005**, *95*, 086801.
(278) Banin, U.; Cao, Y.; Katz, D.; Millo, O. Identification of Atomic-Like Electronic States in Indium Arsenide Nanocrystal Quantum Dots. *Nature* **1999**, *400*, 542−544.
(279) Overgaag, K.; Liljeroth, P.; Grandidier, B.; Vanmaekelbergh, D. Scanning Tunneling Spectroscopy of Individual PbSe Quantum Dots and Molecular Aggregates Stabilized in an Inert Nanocrystal Matrix. *ACS Nano* **2008**, *2*, 600−606.
(280) Liljeroth, P.; Overgaag, K.; Urbieta, A.; Grandidier, B.; Hickey, S. G.; Vanmaekelbergh, D. Variable Orbital Coupling in a Two-Dimensional Quantum-Dot Solid Probed on a Local Scale. *Phys. Rev. Lett.* **2006**, *97*, 096803.
(281) Steiner, D.; Azulay, D.; Aharoni, A.; Salant, A.; Banin, U.; Millo, O. Electronic Structure and Self-Assembly of Cross-Linked Semiconductor Nanocrystal Arrays. *Nanotechnology* **2008**, *19*, 065201.
(282) Bakkers, E. P. A. M.; Vanmaekelbergh, D. Resonant Electron Tunneling through Semiconducting Nanocrystals in a Symmetrical and an Asymmetrical Junction. *Phys. Rev. B: Condens. Matter Mater. Phys.* **2000**, *62*, R7743−R7746.
(283) Katz, D.; Kan, S. H.; Banin, U.; Millo, O. Junction Symmetry Effects in Resonant Tunneling through InAs Nanocrystal Quantum Dots. *Phys. A* **2001**, *302*, 328−334.
(284) Katz, D.; Millo, O.; Kan, S. H.; Banin, U. Control of Charging in Resonant Tunneling through InAs Nanocrystal Quantum Dots. *Appl. Phys. Lett.* **2001**, *79*, 117−119.
(285) Millo, O.; Katz, D.; Cao, Y.; Banin, U. Scanning Tunneling Spectroscopy of InAs Nanocrystal Quantum Dots. *Phys. Rev. B: Condens. Matter Mater. Phys.* **2000**, *61*, 16773−16777.
(286) Katz, D.; Millo, O.; Levi, Y.; Banin, U.; Cao, Y. W. Size-Dependent Tunneling Spectroscopy of InAs Nanocrystals. *Phys. B* **2000**, *284-288*, 1760−1761.
(287) Millo, O.; Katz, D.; Cao, Y. W.; Banin, U. Tunneling and Optical Spectroscopy of InAs and InAs/ZnSe Core/Shell Nanocrystalline Quantum Dots. *Phys. Status Solidi B* **2001**, *224*, 271−276.
(288) Millo, O.; Katz, D.; Cao, Y. W.; Banin, U. Imaging and Spectroscopy of Artificial-Atom States in Core/Shell Nanocrystal Quantum Dots. *Phys. Rev. Lett.* **2001**, *86*, 5751−5754.
(289) Bakkers, E. P. A. M.; Hens, Z.; Kouwenhoven, L. P.; Gurevich, L.; Vanmaekelbergh, D. A Tunneling Spectroscopy Study on the Single-Particle Energy Levels and Electron-Electron Interactions in CdSe Quantum Dots. *Nanotechnology* **2002**, *13*, 258−262.
(290) Hens, Z.; Vanmaekelbergh, D.; Stoffels, E. J. A. J.; Van Kempen, H. Effects of Crystal Shape on the Energy Levels of Zero-Dimensional PbS Quantum Dots. *Phys. Rev. Lett.* **2002**, *88*, 236803.
(291) Banin, U.; Millo, O. Tunneling and Optical Spectroscopy of Semiconductor Nanocrystals. *Annu. Rev. Phys. Chem.* **2003**, *54*, 465−492.
(292) Rothenberg, E.; Mokari, T.; Kazes, M.; Banin, U.; Katz, D.; Steiner, D.; Millo, O. Electronic Level Structure and Single Electron Tunneling Effects in CdSe Quantum Rods. *Isr. J. Chem.* **2004**, *44*, 391−400.
(293) Hens, Z.; Grandidier, B.; Deresmes, D.; Allan, G.; Delerue, C.; Stievenard, D.; Vanmaekelbergh, D. Evolution of the Density of States on Going from a Two- to a Zero-Dimensional Semiconductor. *Europhys. Lett.* **2004**, *65*, 809−815.
(294) Millo, O.; Katz, D.; Steiner, D.; Rothenberg, E.; Mokari, T.; Kazes, M.; Banin, U. Charging and Quantum Size Effects in Tunneling and Optical Spectroscopy of CdSe Nanorods. *Nanotechnology* **2004**, *15*, R1−R6.
(295) Nahum, E.; Ebenstein, Y.; Aharoni, A.; Mokari, T.; Banin, U.; Shimoni, N.; Millo, O. Transport and Charging in Single Semiconductor Nanocrystals Studied by Conductance Atomic Force Microscopy. *Nano Lett.* **2004**, *4*, 103−108.
(296) Borys, N. J.; Walter, M. J.; Huang, J.; Talapin, D. V.; Lupton, J. M. The Role of Particle Morphology in Interfacial Energy Transfer in CdSe/CdS Heterostructure Nanocrystals. *Science* **2010**, *330*, 1371−1374.
(297) Stomp, R.; Miyahara, Y.; Schaer, S.; Sun, Q.; Guo, H.; Grutter, P.; Studenikin, S.; Poole, P.; Sachrajda, A. Detection of Single-Electron Charging in an Individual InAs Quantum Dot by Noncontact Atomic-Force Microscopy. *Phys. Rev. Lett.* **2005**, *94*, 056802.
(298) Vanmaekelbergh, D.; Liljeroth, P. Electron-Conducting Quantum Dot Solids: Novel Materials Based on Colloidal Semiconductor Nanocrystals. *Chem. Soc. Rev.* **2005**, *34*, 299−312.
(299) Azulay, D.; Kopnov, F.; Tenne, R.; Balberg, I.; Millo, O. Observation of Current Reversal in the Scanning Tunneling Spectra of Fullerene-Like WS_2 Nanoparticles. *Nano Lett.* **2006**, *6*, 760−764.
(300) Steiner, D.; Aharoni, A.; Banin, U.; Millo, O. Level Structure of InAs Quantum Dots in Two-Dimensional Assemblies. *Nano Lett.* **2006**, *6*, 2201−2205.
(301) Toker, D.; Balberg, I.; Zelaya-Angel, O.; Savir, E.; Millo, O. Size-Dependent Local Conductance Properties of CdSe Nanocrystal Ensembles. *Phys. Rev. B: Condens. Matter Mater. Phys.* **2006**, *73*, 045317.
(302) Liljeroth, P.; Overgaag, K.; Urbieta, A.; Grandidier, B.; Hickey, S. G.; Vanmaekelbergh, D. Variable Orbital Coupling in a Two-Dimensional Quantum-Dot Solid Probed on a Local Scale. *Phys. Rev. Lett.* **2006**, *97*, 096803.
(303) Hens, Z.; Kooij, E. S.; Allan, G.; Grandidier, B.; Vanmaekelbergh, D. Electrodeposited Nanocrystalline PbSe Quantum Wells: Synthesis, Electrical and Optical Properties. *Nanotechnology* **2005**, *16*, 339−343.
(304) Steiner, D.; Dorfs, D.; Banin, U.; Della Sala, F.; Manna, L.; Millo, O. Determination of Band Offsets in Heterostructured Colloidal Nanorods Using Scanning Tunneling Spectroscopy. *Nano Lett.* **2008**, *8*, 2954−2958.
(305) Soreni-Harari, M.; Yaacobi-Gross, N.; Steiner, D.; Aharoni, A.; Banin, U.; Millo, O.; Tessler, N. Tuning Energetic Levels in Nanocrystal Quantum Dots through Surface Manipulations. *Nano Lett.* **2008**, *8*, 678−684.
(306) Costi, R.; Cohen, G.; Salant, A.; Rabani, E.; Banin, U. Electrostatic Force Microscopy Study of Single Au-CdSe Hybrid Nanodumbbells: Evidence for Light-Induced Charge Separation. *Nano Lett.* **2009**, *9*, 2031−2039.
(307) Cockins, L.; Miyahara, Y.; Bennett, S. D.; Clerk, A. A.; Studenikin, S.; Poole, P.; Sachrajda, A.; Grutter, P. Energy Levels of Few-Electron Quantum Dots Imaged and Characterized by Atomic Force Microscopy. *Proc. Natl. Acad. Sci. U. S. A.* **2010**, *107*, 9496−9501.

DOI: 10.1021/acs.chemrev.5b00678
Chem. Rev. 2016, 116, 11181−11219

(308) Mocatta, D.; Cohen, G.; Schattner, J.; Millo, O.; Rabani, E.; Banin, U. Heavily Doped Semiconductor Nanocrystal Quantum Dots. *Science* **2011**, *332*, 77−81.
(309) Toker, D.; Balberg, I.; Zelaya-Angel, O.; Savir, E.; Millo, O. Local Charging Effects in Nanocrystalline CdSe Films. *Phys. Rev. B: Condens. Matter Mater. Phys.* **2011**, *83*, 085303.
(310) Toker, D.; Balberg, I.; Zelaya-Angel, O.; Savir, E.; Millo, O. Local Charging Effects in Nanocrystalline CdSe Films. *Phys. Rev. B: Condens. Matter Mater. Phys.* **2011**, *83*, 085303.
(311) Nguyen, T. H.; Habinshuti, J.; Justo, Y.; Gomes, R.; Mahieu, G.; Godey, S.; Nys, J. P.; Carrillo, S.; Hens, Z.; Robbe, O.; et al. Charge Carrier Identification in Tunneling Spectroscopy of Core-Shell Nanocrystals. *Phys. Rev. B: Condens. Matter Mater. Phys.* **2011**, *84*, 195133.
(312) Diaconescu, B.; Padilha, L. A.; Nagpal, P.; Swartzentruber, B. S.; Klimov, V. I. Measurement of Electronic States of PbS Nanocrystal Quantum Dots Using Scanning Tunneling Spectroscopy: The Role of Parity Selection Rules in Optical Absorption. *Phys. Rev. Lett.* **2013**, *110*, 127406.
(313) Gupta, S. K.; He, H.; Banyai, D.; Kandalam, A. K.; Pandey, R. Electron Tunneling Characteristics of a Cubic Quantum Dot, (PbS)(32). *J. Chem. Phys.* **2013**, *139*, 244307.
(314) Kuo, D. M. T. Tunneling Current Spectra of a Metal Core/Semiconductor Shell Quantum Dot Molecule. *Jpn. J. Appl. Phys.* **2013**, *52*, 065001.
(315) Wolf, O.; Dasog, M.; Yang, Z.; Balberg, I.; Veinot, J. G. C.; Millo, O. Doping and Quantum Confinement Effects in Single Si Nanocrystals Observed by Scanning Tunneling Spectroscopy. *Nano Lett.* **2013**, *13*, 2516−2521.
(316) Roy-Gobeil, A.; Miyahara, Y.; Grutter, P. Revealing Energy Level Structure of Individual Quantum Dots by Tunneling Rate Measured by Single-Electron Sensitive Electrostatic Force Spectroscopy. *Nano Lett.* **2015**, *15*, 2324−2328.
(317) Wang, T.; Vaxenburg, R.; Liu, W.; Rupich, S. M.; Lifshitz, E.; Efros, A. L.; Talapin, D. V.; Sibener, S. J. Size-Dependent Energy Levels of InSb Quantum Dots Measured by Scanning Tunneling Spectroscopy. *ACS Nano* **2015**, *9*, 725−732.
(318) Binning, G.; Rohrer, H.; Gerber, C.; Weibel, E. Tunneling through a Controllable Vacuum Gap. *Appl. Phys. Lett.* **1982**, *40*, 178.
(319) Binnig, G.; Rohrer, H.; Gerber, C.; Weibel, E. Surface Studies by Scanning Tunneling Microscopy. *Phys. Rev. Lett.* **1982**, *49*, 57−61.
(320) Binnig, G.; Rohrer, H.; Gerber, C.; Weibel, E. 7 by 7 Reconstruction on Si(111) Resolved in Real Space. *Phys. Rev. Lett.* **1983**, *50*, 120−123.
(321) Binnig, G.; Rohrer, H.; Gerber, C.; Weibel, E. 7 × 7 Reconstruction on Si(111) Resolved in Real Space. *Phys. Rev. Lett.* **1983**, *50*, 120−123.
(322) Binnig, G.; Rohrer, H. Scanning Tunneling Microscopy - from Birth to Adolescence. *Rev. Mod. Phys.* **1987**, *59*, 615−625.
(323) Chamarro, M.; Dib, M.; Voliotis, V.; Filoramo, A.; Roussignol, P.; Gacoin, T.; Boilot, J. P.; Delerue, C.; Allan, G.; Lannoo, M. Interplay of Coulomb, Exchange, and Spin-Orbit Effects in Semiconductor Nanocrystallites. *Phys. Rev. B: Condens. Matter Mater. Phys.* **1998**, *57*, 3729−3732.
(324) Allan, G.; Delerue, C.; Lannoo, M. Nature of Impurity States in Doped Amorphous Silicon. *Phys. Rev. B: Condens. Matter Mater. Phys.* **2000**, *61*, 10206−10210.
(325) Niquet, Y. M.; Allan, G.; Delerue, C.; Lannoo, M. Quantum Confinement in Germanium Nanocrystals. *Appl. Phys. Lett.* **2000**, *77*, 1182−1184.
(326) Niquet, Y. M.; Delerue, C.; Allan, G.; Lannoo, M. Method for Tight-Binding Parametrization: Application to Silicon Nanostructures. *Phys. Rev. B: Condens. Matter Mater. Phys.* **2000**, *62*, 5109−5116.
(327) Niquet, Y. M.; Delerue, C.; Lannoo, M.; Allan, G. Single-Particle Tunneling in Semiconductor Quantum Dots. *Phys. Rev. B: Condens. Matter Mater. Phys.* **2001**, *64*, 113305.
(328) Niquet, Y. M.; Delerue, C.; Allan, G.; Lannoo, M. Interpretation and Theory of Tunneling Experiments on Single Nanostructures. *Phys. Rev. B: Condens. Matter Mater. Phys.* **2002**, *65*, 165334.
(329) Hens, Z.; Vanmaekelbergh, D.; Kooij, E. S.; Wormeester, H.; Allan, G.; Delerue, C. Effect of Quantum Confinement on the Dielectric Function of PbSe. *Phys. Rev. Lett.* **2004**, *92*, 026808.
(330) Bartnik, A. C.; Efros, A. L.; Koh, W. K.; Murray, C. B.; Wise, F. W. Electronic States and Optical Properties of PbSe Nanorods and Nanowires. *Phys. Rev. B: Condens. Matter Mater. Phys.* **2010**, *82*, 195313.
(331) Moreels, I.; Lambert, K.; Smeets, D.; De Muynck, D.; Nollet, T.; Martins, J. C.; Vanhaecke, F.; Vantomme, A.; Delerue, C.; Allan, G.; et al. Size-Dependent Optical Properties of Colloidal PbS Quantum Dots. *ACS Nano* **2009**, *3*, 3023−3030.
(332) Efros, A. L.; Rosen, M.; Kuno, M.; Nirmal, M.; Norris, D. J.; Bawendi, M. Band-Edge Exciton in Quantum Dots of Semiconductors with a Degenerate Valence Band: Dark and Bright Exciton States. *Phys. Rev. B: Condens. Matter Mater. Phys.* **1996**, *54*, 4843−4856.
(333) Efros, A. L.; Rosen, M. The Electronic Structure of Semiconductor Nanocrystals. *Annu. Rev. Mater. Sci.* **2000**, *30*, 475−521.
(334) Franceschetti, A.; Fu, H.; Wang, L. W.; Zunger, A. Many-Body Pseudopotential Theory of Excitons in InP and CdSe Quantum Dots. *Phys. Rev. B: Condens. Matter Mater. Phys.* **1999**, *60*, 1819−1829.
(335) Franceschetti, A.; Williamson, A.; Zunger, A. Addition Spectra of Quantum Dots: The Role of Dielectric Mismatch. *J. Phys. Chem. B* **2000**, *104*, 3398−3401.
(336) Franceschetti, A.; Zunger, A. Pseudopotential Calculations of Electron and Hole Addition Spectra of InAs, InP, and Si Quantum Dots. *Phys. Rev. B: Condens. Matter Mater. Phys.* **2000**, *62*, 2614−2623.
(337) An, J. M.; Franceschetti, A.; Dudiy, S. V.; Zunger, A. The Peculiar Electronic Structure of PbSe Quantum Dots. *Nano Lett.* **2006**, *6*, 2728−2735.
(338) An, J. M.; Califano, M.; Franceschetti, A.; Zunger, A. Excited-State Relaxation in PbSe Quantum Dots. *J. Chem. Phys.* **2008**, *128*, 164720.
(339) Kang, I.; Wise, F. W. Electronic Structure and Optical Properties of PbS and PbSe Quantum Dots. *J. Opt. Soc. Am. B* **1997**, *14*, 1632−1646.
(340) Wise, F. W. Lead Salt Quantum Dots: The Limit of Strong Quantum Confinement. *Acc. Chem. Res.* **2000**, *33*, 773−780.
(341) Zunger, A.; Franceschetti, A.; Bester, G.; Jones, W. B.; Kim, K.; Graf, P. A.; Wang, L. W.; Canning, A.; Marques, O.; Voemel, C. Predicting the electronic properties of 3D, million-atom semiconductor nanostructure architectures. *J. Phys.: Conf. Ser.* **2006**, *46*, 292−298.
(342) Delerue, C.; Lannoo, M. *Nanostructures. Theory and Modelling*; Springer-Verlag: 2004.
(343) Zunger, A. Electronic-Structure Theory of Semiconductor Quantum Dots. *MRS Bull.* **1998**, *23*, 35−42.
(344) Wang, L. W.; Franceschetti, A.; Zunger, A. Million-Atom Pseudopotential Calculation of Gamma-X Mixing in GaAs/Alas Superlattices and Quantum Dots. *Phys. Rev. Lett.* **1997**, *78*, 2819−2822.
(345) Germeau, A.; Roest, A. L.; Vanmaekelbergh, D.; Allan, G.; Delerue, C.; Meulenkamp, E. A. Optical Transitions in Artificial Few-Electron Atoms Strongly Confined inside ZnO Nanocrystals. *Phys. Rev. Lett.* **2003**, *90*, 097401.
(346) Allan, G.; Delerue, C. Confinement Effects in PbSe Quantum Wells and Nanocrystals. *Phys. Rev. B: Condens. Matter Mater. Phys.* **2004**, *70*, 245321.
(347) Franceschetti, A.; Zunger, A. Addition Energies and Quasiparticle Gap of CdSe Nanocrystals. *Appl. Phys. Lett.* **2000**, *76*, 1731−1733.
(348) Franceschetti, A.; Williamson, A.; Zunger, A. Addition Spectra of Quantum Dots: The Role of Dielectric Mismatch. *J. Phys. Chem. B* **2000**, *104*, 3398−3401.
(349) Habinshuti, J.; Kilian, O.; Cristini-Robbe, O.; Sashchiuk, A.; Addad, A.; Turrell, S.; Lifshitz, E.; Grandidier, B.; Wirtz, L. Anomalous Quantum Confinement of the Longitudinal Optical Phonon Mode in

DOI: 10.1021/acs.chemrev.5b00678
Chem. Rev. 2016, 116, 11181−11219

PbSe Quantum Dots. *Phys. Rev. B: Condens. Matter Mater. Phys.* **2013**, *88*, 115313.
(350) Franceschetti, A.; Zunger, A. Pseudopotential Calculations of Electron and Hole Addition Spectra of InAs, InP, and Si Quantum Dots. *Phys. Rev. B: Condens. Matter Mater. Phys.* **2000**, *62*, 2614−2623.
(351) Norris, D. J.; Bawendi, M. G. Structure in the Lowest Absorption Feature of CdSe Quantum Dots. *J. Chem. Phys.* **1995**, *103*, 5260−5268.
(352) Empedocles, S. A.; Norris, D. J.; Bawendi, M. G. Photoluminescence Spectroscopy of Single CdSe Nanocrystallite Quantum Dots. *Phys. Rev. Lett.* **1996**, *77*, 3873−3876.
(353) Norris, D. J.; Efros, A. L.; Rosen, M.; Bawendi, M. G. Size Dependence of Exciton Fine Structure in CdSe Quantum Dots. *Phys. Rev. B: Condens. Matter Mater. Phys.* **1996**, *53*, 16347−16354.
(354) Norris, D. J.; Bawendi, M. G.; Brus, L. E. Optical Properties of Semiconductor Nanocrystals (Quantum Dots). *Mol. Electron.* **1997**, 281−323.
(355) Guyot-Sionnest, P.; Hines, M. A. Intraband Transitions in Semiconductor Nanocrystals. *Appl. Phys. Lett.* **1998**, *72*, 686−688.
(356) Shim, M.; Guyot-Sionnest, P. N-Type Colloidal Semiconductor Nanocrystals. *Nature* **2000**, *407*, 981−983.
(357) Shim, M.; Wang, C.; Guyot-Sionnest, P. Charge-Tunable Optical Properties in Colloidal Semiconductor Nanocrystals. *J. Phys. Chem. B* **2001**, *105*, 2369−2373.
(358) Shim, M.; Wang, C. J.; Norris, D. J.; Guyot-Sionnest, P. Doping and Charging in Colloidal Semiconductor Nanocrystals. *MRS Bull.* **2001**, *26*, 1005−1008.
(359) Wang, C.; Shim, M.; Guyot-Sionnest, P. Electrochromic Nanocrystal Quantum Dots. *Science* **2001**, *291*, 2390−2392.
(360) Wang, C.; Shim, M.; Guyot-Sionnest, P. Electrochromic Semiconductor Nanocrystal Films. *Appl. Phys. Lett.* **2002**, *80*, 4−6.
(361) Wehrenberg, B. L.; Wang, C.; Guyot-Sionnest, P. Interband and Intraband Optical Studies of PbSe Colloidal Quantum Dots. *J. Phys. Chem. B* **2002**, *106*, 10634−10640.
(362) Yu, D.; Wang, C.; Guyot-Sionnest, P. N-Type Conducting CdSe Nanocrystal Solids. *Science* **2003**, *300*, 1277−1280.
(363) Grandidier, B. Scanning Tunnelling Spectroscopy of Low-Dimensional Semiconductor Systems. *J. Phys.: Condens. Matter* **2004**, *16*, S161−S170.
(364) Maruccio, G.; Meyer, C.; Matsui, T.; Talapin, D. V.; Hickey, S. G.; Weller, H.; Wiesendanger, R. Wavefunction Mapping of Immobilized InP Semiconductor Nanocrystals. *Small* **2009**, *5*, 808−812.
(365) Tersoff, J.; Hamann, D. R. Theory and Application for the Scanning Tunneling Microscope. *Phys. Rev. Lett.* **1983**, *50*, 1998.
(366) Hämäläinen, S. K.; Sun, Z.; Boneschanscher, M. P.; Uppstu, A.; Ijas, M.; Harju, A.; Vanmaekelbergh, D.; Liljeroth, P. Quantum-Confined Electronic States in Atomically Well-Defined Graphene Nanostructures. *Phys. Rev. Lett.* **2011**, *107*, 236803.
(367) van der Lit, J.;Boneschanscher, M. P.;Vanmaekelbergh, D.;Ijas, M.;Uppstu, A.;Ervasti, M.;Harju, A.;Liljeroth, P.;Swart, I. Suppression of Electron-Vibron Coupling in Graphene Nanoribbons Contacted Via a Single Atom. *Nat. Commun.* **2013**, *4*.10.1038/ncomms3023
(368) Schulz, F.; Ijaes, M.; Drost, R.; Hämäläinen, S. K.; Harju, A.; Seitsonen, A. P.; Liljeroth, P. Many-Body Transitions in a Single Molecule Visualized by Scanning Tunnelling Microscopy. *Nat. Phys.* **2015**, *11*, 229−234.
(369) Repp, J.; Liljeroth, P.; Meyer, G. Coherent Electron-Nuclear Coupling in Oligothiophene Molecular Wires. *Nat. Phys.* **2010**, *6*, 975−979.
(370) Venema, L. C.; Wildoer, J. W. G.; Janssen, J. W.; Tans, S. J.; Tuinstra, H.; Kouwenhoven, L. P.; Dekker, G. Imaging Electron Wave Functions of Quantized Energy Levels in Carbon Nanotubes. *Science* **1999**, *283*, 52−55.
(371) Lemay, S. G.; Janssen, J. W.; van den Hout, M.; Mooij, M.; Bronikowski, M. J.; Willis, P. A.; Smalley, R. E.; Kouwenhoven, L. P.; Dekker, C. Two-Dimensional Imaging of Electronic Wavefunctions in Carbon Nanotubes. *Nature* **2001**, *412*, 617−620.
(372) Jarvinen, P.; Hämäläinen, S. K.; Ijas, M.; Harju, A.; Liljeroth, P. Self-Assembly and Orbital Imaging of Metal Phthalocyanines on a Graphene Model Surface. *J. Phys. Chem. C* **2014**, *118*, 13320−13325.
(373) Crommie, M. F.; Lutz, C. P.; Eigler, D. M. Imaging Standing Waves in a 2-Dimensional Electron-Gas. *Nature* **1993**, *363*, 524−527.
(374) Voyles, P. M.; Muller, D. A.; Grazul, J. L.; Citrin, P. H.; Gossmann, H. J. L. Atomic-Scale Imaging of Individual Dopant Atoms and Clusters in Highly N-Type Bulk Si. *Nature* **2002**, *416*, 826−829.
(375) Grandidier, B.; Niquet, Y. M.; Legrand, B.; Nys, J. P.; Priester, C.; Stievenard, D.; Gerard, J. M.; Thierry-Mieg, V. Imaging the Wave-Function Amplitudes in Cleaved Semiconductor Quantum Boxes. *Phys. Rev. Lett.* **2000**, *85*, 1068−1071.
(376) Rontani, M.; Molinari, E. Imaging Quasiparticle Wave Functions in Quantum Dots Via Tunneling Spectroscopy. *Phys. Rev. B: Condens. Matter Mater. Phys.* **2005**, *71*, 233106.
(377) Atanasov, V.; Saxena, A. Tuning the Electronic Properties of Corrugated Graphene: Confinement, Curvature, and Band-Gap Opening. *Phys. Rev. B: Condens. Matter Mater. Phys.* **2010**, *81*, 205409.
(378) Eckart, F.; Raithel, K. The Amphoteric Behaviour of Lead Selenide as an Electronic Semi-Conductor. *Naturwissenschaften* **1941**, *29*, 572−573.
(379) Blackwell, D. E.; Simpson, O.; Sutherland, G. Lead Selenide Cells for Infra-Red Spectroscopy. *Nature* **1947**, *160*, 793−793.
(380) Simpson, O. Conductivity of Evaporated Films of Lead Selenide. *Nature* **1947**, *160*, 791−792.
(381) Darby, J.; Hatton, J.; Rollin, B. V. Superconductivity of Lead Sulphide, Selenide and Telluride. *Proc. Phys. Soc., London, Sect. A* **1950**, *63*, 1181−1182.
(382) Gibson, A. F. The Absorption Spectra of Solid Lead Sulphide, Selenide and Telluride. *Proc. Phys. Soc., London, Sect. B* **1950**, *63*, 756−767.
(383) Hirahara, E.; Murakami, M. Hall Effect and Electrical Conductivity of Lead Selenide. *J. Phys. Soc. Jpn.* **1954**, *9*, 671−681.
(384) Rossetti, R.; Hull, R.; Gibson, J. M.; Brus, L. E. Hybrid Electronic Properties between the Molecular and Solid State Limits: Lead Sulfide and Silver Halide Crystallites. *J. Chem. Phys.* **1985**, *83*, 1406−1410.
(385) Putley, E. H. Electrical Conductivity in the Compounds PbS, PbSe, PbTe. *Proc. Phys. Soc., London, Sect. B* **1952**, *65*, 388−389.
(386) Silverman, S. J.; Levinstein, H. Electrical Properties of Single Crystals and Thin Films of PbSe and PbTe. *Phys. Rev.* **1954**, *94*, 871−876.
(387) Smith, R. A. Bestimmung Der Verbotenen Zone, Tragerbeweglichkeiten Und Lebensdauern Von PbS, PbSe Und PbTe. *Angew. Chem., Int. Ed.* **1954**, *66*, 645−645.
(388) Mackintosh, I. M. Photon-Radiative Recombination in PbSe, PbTe and PbS. *Proc. Phys. Soc., London, Sect. B* **1956**, *69*, 115−118.
(389) Jones, R. H. The Effect of Oxygen on an Evaporated PbSe Layer. *Proc. Phys. Soc., London, Sect. B* **1957**, *70*, 704−708.
(390) Allgaier, R. S.; Scanlon, W. W. Mobility of Electrons and Holes in PbS, PbSe, and PbTe between Room Temperature and 4.2-Degrees-K. *Phys. Rev.* **1958**, *111*, 1029−1037.
(391) Baryshev, N. S. Radiative Recombination of Holes and Electrons in PbS, PbSe and PbTe. *Sov. Phys. - Solid State* **1961**, *3*, 1037−1038.
(392) Lin, P. J.; Kleinman, L. Energy Bands of PbTe, PbSe and PbS. *Phys. Rev.* **1966**, *142*, 478−489.
(393) Dubrovsk, In; Efimova, B. A.; Nensberg, E. D. Investigation of Nonparabolicity of Conduction Bands of PbSe and PbS. *Sov. Phys. Semicond.* **1968**, *2*, 436.
(394) Rabii, S. Investigation of Energy-Band Structures and Electronic Properties of PbS and PbSe. *Phys. Rev.* **1968**, *167*, 801−808.
(395) Bailey, P. T.; O'Brien, M. W.; Rabii, S. Direct-Transition Optical Absorption in PbS PbSe and PbTe from Relativistic Augmented-Plane-Wave Functions. *Phys. Rev.* **1969**, *179*, 735.
(396) Dalven, R. A Review of Semiconductor Properties of PbTe, PbSe, PbS and PbO. *Infrared Phys.* **1969**, *9*, 141.
(397) Overhof, H.; Rossler, U. Electronic Structure of PbS, PbSe, and PbTe. *Phys. Status Solidi B* **1970**, *37*, 691.

DOI: 10.1021/acs.chemrev.5b00678
Chem. Rev. 2016, 116, 11181−11219

(398) Kucheren, Iv; Korolev, Y. N.; Shotov, A. P. Carrier Mobility in PbSe Crystals in Temperaure Range 4.2−300 Degrees K. *Sov. Phys. Semicond.* **1971**, *5*, 868.
(399) Kinoshita, J.; Glosser, R. Band-Structure Identification and Measurement of Spin-Orbit-Splitting in PbSe by Electroreflectance. *Phys. Lett. A* **1974**, *48*, 393−394.
(400) Martinez, G.; Schluter, M.; Cohen, M. L. Electronic-Structure of PbSe and PbTe 0.1. Band Structures, Densities of States, and Effective Masses. *Phys. Rev. B* **1975**, *11*, 651−659.
(401) Grandke, T.; Ley, L.; Cardona, M.; Preier, H. Spin-Orbit-Splitting in Valence Bands of PbSe from Angle-Resolved Uv Photoemission. *Solid State Commun.* **1977**, *24*, 287−290.
(402) Freik, D. M.; Shperun, V. M.; Solonichnyi, Y. V.; Brodin, I. I. Synthesis and Growth of PbTe and PbSe Films. *Kristallografiya* **1979**, *24*, 636−640.
(403) Ravindra, N. M.; Auluck, S.; Srivastava, V. K. Temperature-Dependence of the Energy-Gap in PbS, PbSe, and PbTe. *Phys. Status Solidi A* **1979**, *52*, K151−K155.
(404) Candea, R. M.; Dadarlat, D.; Turcu, R.; Indrea, E. Properties of PbSe Films Prepared by Chemical Anorganic Deposition. *Phys. Status Solidi A* **1985**, *90*, K91−K95.
(405) Molin, A. N.; Dikusar, A. I. Electrochemical Deposition of PbSe Thin-Films from Aqueous- Solutions. *Thin Solid Films* **1995**, *265*, 3−9.
(406) Streltsov, E. A.; Osipovich, N. P.; Ivashkevich, L. S.; Lyakhov, A. S.; Sviridov, V. V. Electrochemical Deposition of PbSe Films. *Electrochim. Acta* **1998**, *43*, 869−873.
(407) Arivazhagan, V.; Manonmani Parvathi, M. M.; Rajesh, S. Investigation of the Quantum Well Width on the Size Effect of PbSe/ZnSe Multiple Quantum Well Structures by Non-Epitaxial Growth. *J. Alloys Compd.* **2013**, *577*, 431−435.
(408) Henglein, A. Q-Particles: Size Quantization Effects in Colloidal Semiconductors. *Prog. Coll. Polym. Sci. S* **1987**, *73*, 1−3.
(409) Henglein, A. Small-Particle Research: Physicochemical Properties of Extremely Small Colloidal Metal and Semiconductor Particles. *Chem. Rev.* **1989**, *89*, 1861−1873.
(410) Guha, S.; Leppert, V. J.; Risbud, S. H.; Kang, I. Observation of Excitonic States in PbSe Nanocrystals. *Solid State Commun.* **1998**, *105*, 695−699.
(411) Du, H.; Chen, C. L.; Krishnan, R.; Krauss, T. D.; Harbold, J. M.; Wise, F. W.; Thomas, M. G.; Silcox, J. Optical Properties of Colloidal PbSe Nanocrystals. *Nano Lett.* **2002**, *2*, 1321−1324.
(412) Murray, C. B. PbSe Quantum Dots and Quantum Cubes. *Abstr. Pap., Am. Chem. Soc.* **2003**, *225*, U441−U442.
(413) Sashchiuk, A.; Amirav, L.; Bashouti, M.; Krueger, M.; Sivan, U.; Lifshitz, E. PbSe Nanocrystal Assemblies: Synthesis and Structural, Optical, and Electrical Characterization. *Nano Lett.* **2004**, *4*, 159−165.
(414) Houtepen, A. J.; Koole, R.; Vanmaekelbergh, D.; Meeldijk, J.; Hickey, S. G. The Hidden Role of Acetate in the PbSe Nanocrystal Synthesis. *J. Am. Chem. Soc.* **2006**, *128*, 6792−6793.
(415) Murray, C. B.; Sun, S.; Gaschler, W.; Doyle, H.; Betley, T. A.; Kagan, C. R. Colloidal Synthesis of Nanocrystals and Nanocrystal Superlattices. *IBM J. Res. Dev.* **2001**, *45*, 47−56.
(416) Lu, W.; Fang, J.; Ding, Y.; Wang, Z. L. Formation of PbSe Nanocrystals: A Growth toward Nanocubes. *J. Phys. Chem. B* **2005**, *109*, 19219−19222.
(417) Yong, K. T.; Sahoo, Y.; Choudhury, K. R.; Swihart, M. T.; Minter, J. R.; Prasad, P. N. Shape Control of PbSe Nanocrystals Using Noble Metal Seed Particles. *Nano Lett.* **2006**, *6*, 709−714.
(418) Harbold, J. M.; Wise, F. W. Photoluminescence Spectroscopy of PbSe Nanocrystals. *Phys. Rev. B: Condens. Matter Mater. Phys.* **2007**, *76*, 125304.
(419) Moreels, I.; Allan, G.; De Geyter, B.; Wirtz, L.; Delerue, C.; Hens, Z. Dielectric Function of Colloidal Lead Chalcogenide Quantum Dots Obtained by a Kramers-Kronig Analysis of the Absorbance Spectrum. *Phys. Rev. B: Condens. Matter Mater. Phys.* **2010**, *81*, 235319.
(420) Koole, R.; Allan, G.; Delerue, C.; Meijerink, A.; Vanmaekelbergh, D.; Houtepen, A. J. Optical Investigation of Quantum Confinement in PbSe Nanocrystals at Different Points in the Brillouin Zone. *Small* **2008**, *4*, 127−133.
(421) An, J. M.; Franceschetti, A.; Zunger, A. The Excitonic Exchange Splitting and Radiative Lifetime in PbSe Quantum Dots. *Nano Lett.* **2007**, *7*, 2129−2135.
(422) Tang, J.; Kemp, K. W.; Hoogland, S.; Jeong, K. S.; Liu, H.; Levina, L.; Furukawa, M.; Wang, X.; Debnath, R.; Cha, D.; et al. Colloidal-Quantum-Dot Photovoltaics Using Atomic-Ligand Passivation. *Nat. Mater.* **2011**, *10*, 765−771.
(423) Carey, G. H.; Chou, K. W.; Yan, B.; Kirmani, A. R.; Amassian, A.; Sargent, E. H. Materials Processing Strategies for Colloidal Quantum Dot Solar Cells: Advances, Present-Day Limitations, and Pathways to Improvement. *MRS Commun.* **2013**, *3*, 83−90.
(424) Petkov, V.; Moreels, I.; Hens, Z.; Ren, Y. PbSe Quantum Dots: Finite, Off-Stoichiometric, and Structurally Distorted. *Phys. Rev. B: Condens. Matter Mater. Phys.* **2010**, *81*, 241304.
(425) Ocier, C. R.; Whitham, K.; Hanrath, T.; Robinson, R. D. Chalcogenidometallate Clusters as Surface Ligands for PbSe Nanocrystal Field-Effect Transistors. *J. Phys. Chem. C* **2014**, *118*, 3377−3385.
(426) Fernee, M. J.; Watt, A.; Warner, J.; Cooper, S.; Heckenberg, N.; Rubinsztein-Dunlop, H. Inorganic Surface Passivation of PbS Nanocrystals Resulting in Strong Photoluminescent Emission. *Nanotechnology* **2003**, *14*, 991−997.
(427) Overgaag, K.; Vanmaekelbergh, D.; Liljeroth, P.; Mahieu, G.; Grandidier, B.; Delerue, C.; Allan, G. Electron-Phonon Coupling and Intervalley Splitting Determine the Linewidth of Single-Electron Transport through PbSe Nanocrystals. *J. Chem. Phys.* **2009**, *131*, 224510.
(428) Andreev, A. D.; Lipovskii, A. A. Anisotropy-Induced Optical Transitions in PbSe and PbS Spherical Quantum Dots. *Phys. Rev. B: Condens. Matter Mater. Phys.* **1999**, *59*, 15402−15404.
(429) Jdira, L.; Overgaag, K.; Stiufiuc, R.; Grandidier, B.; Delerue, C.; Speller, S.; Vanmaekelbergh, D. Linewidth of Resonances in Scanning Tunneling Spectroscopy. *Phys. Rev. B: Condens. Matter Mater. Phys.* **2008**, *77*, 205308.
(430) Norris, D. J.; Bawendi, M. G. Measurement and Assignment of the Size-Dependent Optical Spectrum in CdSe Quantum Dots. *Phys. Rev. B: Condens. Matter Mater. Phys.* **1996**, *53*, 16338−16346.
(431) Tews, M.; Pfannkuche, D. Stark Effect in Colloidal Indium Arsenide Nanocrystal Quantum Dots: Consequences for Wave-Function Mapping Experiments. *Phys. Rev. B: Condens. Matter Mater. Phys.* **2002**, *65*, 073307.
(432) He, L. X.; Bester, G.; Zunger, A. Prediction of an Excitonic Ground State in InAs/InSb Quantum Dots. *Phys. Rev. Lett.* **2005**, *94*, 016801.
(433) Marquez, J.; Geelhaar, L.; Jacobi, K. Atomically Resolved Structure of InAs Quantum Dots. *Appl. Phys. Lett.* **2001**, *78*, 2309−2311.
(434) Johal, T. K.; Rinaldi, R.; Passaseo, A.; Cingolani, R.; Vasanelli, A.; Ferreira, R.; Bastard, G. Imaging of the Electronic States of Self-Assembled $In_xGa_{1-x}As$ Quantum Dots by Scanning Tunneling Spectroscopy. *Phys. Rev. B: Condens. Matter Mater. Phys.* **2002**, *66*, 075336.
(435) Urbieta, A.; Grandidier, B.; Nys, J. P.; Deresmes, D.; Stievenard, D.; Lemaitre, A.; Patriarche, G.; Niquet, Y. M. Scanning Tunneling Spectroscopy of Cleaved InAs/GaAs Quantum Dots at Low Temperatures. *Phys. Rev. B: Condens. Matter Mater. Phys.* **2008**, *77*, 155313.
(436) Fain, B.; Girard, J. C.; Elvira, D.; David, C.; Beaudoin, G.; Beveratos, A.; Robert-Philip, I.; Sagnes, I.; Wang, Z. Z. Electronic Structure of Cleaved InAsP/InP(001) Quantum Dots Measured by Scanning Tunneling Spectroscopy. *Appl. Phys. Lett.* **2010**, *97*, 171903.
(437) Teichmann, K.; Wenderoth, M.; Loth, S.; Garleff, J. K.; Wijnheijmer, A. P.; Koenraad, P. M.; Ulbrich, R. G. Bistable Charge Configuration of Donor Systems near the GaAs(110) Surfaces. *Nano Lett.* **2011**, *11*, 3538−3542.

DOI: 10.1021/acs.chemrev.5b00678
Chem. Rev. 2016, 116, 11181−11219

(438) Akhavan, V. A.; Panthani, M. G.; Goodfellow, B. W.; Reid, D. K.; Korgel, B. A. Thickness-Limited Performance of $CuInSe_2$ Nanocrystal Photovoltaic Devices. *Opt. Express* **2010**, *18*, A411−A420.
(439) Dong, Y.; Feenstra, R. M.; Semtsiv, M. P.; Masselink, W. T. Band Offsets of InGaP/GaAs Heterojunctions by Scanning Tunneling Spectroscopy. *J. Appl. Phys.* **2008**, *103*, 073704.
(440) Holmes, J. D.; Ziegler, K. J.; Doty, R. C.; Pell, L. E.; Johnston, K. P.; Korgel, B. A. Highly Luminescent Silicon Nanocrystals with Discrete Optical Transitions. *J. Am. Chem. Soc.* **2001**, *123*, 3743−3748.
(441) Ding, Z. F.; Quinn, B. M.; Haram, S. K.; Pell, L. E.; Korgel, B. A.; Bard, A. J. Electrochemistry and Electrogenerated Chemiluminescence from Silicon Nanocrystal Quantum Dots. *Science* **2002**, *296*, 1293−1297.
(442) Zaknoon, B.; Bahir, G.; Saguy, C.; Edrei, R.; Hoffman, A.; Rao, R. A.; Muralidhar, R.; Chang, K. M. Study of Single Silicon Quantum Dots' Band Gap and Single-Electron Charging Energies by Room Temperature Scanning Tunneling Microscopy. *Nano Lett.* **2008**, *8*, 1689−1694.
(443) Rosso-Vasic, M.; Spruijt, E.; Popovic, Z.; Overgaag, K.; van Lagen, B.; Grandidier, B.; Vanmaekelbergh, D.; Dominguez-Gutierrez, D.; De Cola, L.; Zuilhof, H. Amine-Terminated Silicon Nanoparticles: Synthesis, Optical Properties and Their Use in Bioimaging. *J. Mater. Chem.* **2009**, *19*, 5926−5933.
(444) Marsen, B.; Lonfat, M.; Scheier, P.; Sattler, K. Energy Gap of Silicon Clusters Studied by Scanning Tunneling Spectroscopy. *Phys. Rev. B: Condens. Matter Mater. Phys.* **2000**, *62*, 6892−6895.
(445) Reboredo, F. A.; Zunger, A. L-to-X Crossover in the Conduction-Band Minimum of Ge Quantum Dots. *Phys. Rev. B: Condens. Matter Mater. Phys.* **2000**, *62*, R2275−R2278.
(446) Millo, O.; Balberg, I.; Azulay, D.; Purkait, T. K.; Swarnakar, A. K.; Rivard, E.; Veinot, J. G. C. Direct Evaluation of the Quantum Confinement Effect in Single Isolated Ge Nanocrystals. *J. Phys. Chem. Lett.* **2015**, *6*, 3396−3402.
(447) Luther, J. M.; Jain, P. K.; Ewers, T.; Alivisatos, A. P. Localized Surface Plasmon Resonances Arising from Free Carriers in Doped Quantum Dots. *Nat. Mater.* **2011**, *10*, 361−366.
(448) Bekenstein, Y.; Vinokurov, K.; Keren-Zur, S.; Hadar, I.; Schilt, Y.; Raviv, U.; Millo, O.; Banin, U. Thermal Doping by Vacancy Formation in Copper Sulfide Nanocrystal Arrays. *Nano Lett.* **2014**, *14*, 1349−1353.
(449) Wang, T.; Vaxenburg, R.; Liu, W. Y.; Rupich, S. M.; Lifshitz, E.; Efros, A. L.; Talapin, D. V.; Sibener, S. J. Size-Dependent Energy Levels of InSb Quantum Dots Measured by Scanning Tunneling Spectroscopy. *ACS Nano* **2015**, *9*, 725−732.
(450) Kalesaki, E.; Evers, W. H.; Allan, G.; Vanmaekelbergh, D.; Delerue, C. Electronic Structure of Atomically Coherent Square Semiconductor Superlattices with Dimensionality Below Two. *Phys. Rev. B: Condens. Matter Mater. Phys.* **2013**, *88*, 115431.

DOI: 10.1021/acs.chemrev.5b00678
Chem. Rev. 2016, 116, 11181−11219